universität wien

DISSERTATION

Titel der Dissertation

„Long-distance multipartite quantum communication"

verfasst von

Dipl.-Ing. Thomas Herbst

angestrebter akademischer Grad

Doktor der Naturwissenschaften (Dr. rer. nat.)

Wien, 2014

Ich habe mich bemüht, sämtliche Inhaber der Bildrechte ausfindig zu machen und ihre Zustimmung zur Verwendung der Bilder in dieser Arbeit eingeholt. Sollte dennoch eine Urheberrechtsverletzung bekannt werden, ersuche ich um Meldung bei mir.

Contents

List of Abbreviations

APD	Avalanche photodiode
AR	Anti-reflective
BBO	β-barium borate
BNC	Bayonet Neill-Concelman
BS	Beam splitter
BSM	Bell-state measurement
CHSH	Clauser-Horne-Shimony-Holt
cps	Counts per second
CSV	Comma-separated values
cw	Continuous wave
ENO	European Northern Observatory
EPR	Einstein-Podolsky-Rosen
ESA	European Space Agency
FBS	Fibre beam splitter
FC	Fibre coupler
FPC	Fibre polarization controller
FPGA	Field programmable gate array
FWHM	Full width at half maximum

GHZ	Greenberger-Horne-Zeilinger
GPS	Global positioning system
HOM	Hong-Ou-Mandel
HR	Highly reflective
HWP	Half-wave plate
IAC	Instituto de Astrofísica de Canarias
IF	Interference filter
ING	Isaac Newton Group of Telescopes
JKT	Jacobus Kapteyn Telescope
LP	Long pass
MM	Multi mode
NIM	Nuclear instrumentation module
OA	Optical Axis
OGS	Optical Ground Station
OP	Operation point
ORM	Observatorio del Roque de los Muchachos
OT	Observatorio del Teide
PBS	Polarizing beam splitter
PI	Physik Instrumente GmbH Co. KG
PPKTP	Periodically poled KTiOPO$_4$
PPS	Pulse per second
PPT	Positive partial transpose
QKD	Quantum key distribution

QRNG	Quantum random number generator
QWP	Quarter-wave plate
Rx	Receiver
SHG	Second-harmonic generation
SM	Single mode
SNR	Signal-to-noise ratio
SPDC	Spontaneous parametric down-conversion
TEM	Transverse electromagnetic
TTL	Transistor-transistor logic
TTU	Time-tag unit
Tx	Transmitter

Abstract

This work addresses two long-distance free-space experiments based on multi-photon polarization entanglement. The highlighted measurements were performed between the Canary Islands La Palma and Tenerife, featuring a 143 km horizontal free-space quantum channel.

Based on the superposition principle, quantum entanglement constitutes the key building block in quantum information sciences. Its nonclassical correlations lay the ground for exciting new protocols like quantum cryptography, quantum computation or quantum teleportation [1–5]. Our first experiment targeted on the teleportation of entanglement, also known as entanglement swapping [6], where the entanglement from two polarization entangled photon pairs 0-1 and 2-3 is swapped onto photons 1-2 and 0-3. This feature constitutes the fundamental resource for so-called quantum repeaters [7; 8]. In the future such devices could be used to subdivide large distances into shorter links and finally extend the entanglement over the whole range by entanglement swapping. In the second experiment we realized four-photon entanglement in the form of a GHZ-state [9; 10], named after the researchers Daniel Greenberger, Michael Horne and Anton Zeilinger.

At the base station on La Palma we employed two sources for polarization-entanglement, generating photon pairs of 808 nm wavelength by spontaneous parametric down-conversion of femtosecond pulsed laser light. In both experiments one of the four photons per pulse was transmitted over a 143 km free-space link to the receiver station on Tenerife, whereas the remaining three photons were measured locally on La Palma. Long term atmospheric turbulences in the near-ground quantum channel were compensated by means of a bi-directional closed-loop tracking of the transceiver telescopes. Despite an average link attenuation of ~ 30 dB over the 143 km free-space channel, we successfully showed entanglement swapping with a statistical significance of more than 6 standard deviations. Moreover we faithfully entangled four photons in a GHZ-state with one of the recipients being separated by 143 km.

Entanglement swapping and multi-photon entanglement such as GHZ-states lay the foundation for the distribution of entanglement over large distances and for entangling

multiple nodes with each other. Our findings prove the feasibility of these protocols in future satellite-based quantum-communication applications, furthering the vision of quantum networks on a global scale.

Zusammenfassung

Die folgende Doktorarbeit beschreibt zwei Freiraumexperimente über große Distanzen basierend auf Multiphotonenverschränkung im Polarisationsfreiheitsgrad. Die angeführten Messungen wurden unter Verwendung eines 143 km langen horizontalen Quantenkanals durch die Erdatmosphäre zwischen den Kanarischen Inseln La Palma und Teneriffa durchgeführt.

Basierend auf dem Superpositionsprinzip stellt die Quantenverschränkung den Schlüsselbaustein für das Gebiet der Quanteninformation dar. Ihre nichtklassischen Korrelationen sind die Grundvoraussetzung für spannende neue Protokolle wie etwa Quantenkryptographie, Quantenberechnungen oder Quantenteleportation [1–5]. Unser erstes Experiment befasste sich mit der Teleportation von Verschränkung, auch Verschränkungsaustausch genannt [6]. Dabei wird die Verschränkung von zwei Photonenpaaren 0-1 und 2-3 auf eine Verschränkung zwischen den Photonen 1-2 und 0-3 übertragen. Diese Eigenschaft stellt die fundamentale Ressource von sogenannten Quanten Repeater [7; 8] dar. Solche Geräte könnten in Zukunft verwendet werden um große Distanzen in kleinere Abschnitte zu unterteilen und schließlich die Verschränkung durch Verschränkungsaustausch über die gesamte Strecke auszudehnen. Im zweiten Experiment haben wir die Verschränkung von vier Photonen in Form eines GHZ-Zustandes [9; 10] gezeigt, benannt nach den Wissenschaftlern Daniel Greenberger, Michael Horne und Anton Zeilinger.

Zwei Quellen für Polarisationsverschränkung in der Basisstation auf La Palma haben anhand von parametrischer Fluoreszenz des Lichts eines Femtosekundenlasers Photonenpaare mit 808 nm Wellenlänge erzeugt. In beiden Experimenten wurde pro Laserpuls jeweils eines von insgesamt vier Photonen über 143 km Luftlinie zur Empfängerstation nach Teneriffa gesendet. Die restlichen drei Photonen wurden lokal auf La Palma registriert. Für die Kompensation von langsamen atmosphärischen Turbulenzen im bodennahen Quantenkanal wurden die Teleskope anhand eines bidirektionalen geschlossenen Regelkreises kontinuierlich nachgeführt. Trotz einer mittleren Abschwächung von ~ 30 dB über den 143 km Quantenkanal haben wir mit einer statistischen Sicherheit von über 6 Standardabweichungen den Austausch der Verschränkung nachgewiesen. Weiters

10

haben wir vier Photonen erfolgreich zu einem GHZ-Zustand verschränkt, wobei einer der vier Empfänger 143 km entfernt war.

Der Austausch von Verschränkung sowie die Verschränkung mehrerer Photonen, wie etwa in einem GHZ-Zustand der Fall, bilden die Grundlage für die Verteilung von Verschränkung über große Distanzen sowie für die Verschränkung mehrerer Datenknoten miteinander. Unsere Ergebnisse beweisen die Realisierbarkeit dieser Protokolle im Lichte zukünftiger Anwendungen im Bereich der satellitenbasierten Quantenkommunikation und rücken die Vision eines weltumspannenden Quantennetzwerks näher.

Preface

More than 100 years after the birth of quantum theory, its consequences have lead to numerous applications indispensable in our everyday life. However, one of the most fundamental features namely the concept of quantum entanglement hasn't been exploited until the last decades. Considering the various possibilities opened up by its counterintuitive properties, the field of quantum information sciences has been constantly growing in importance over the past years. The vision of a future quantum internet [11] calls for a world-spanning quantum network based on ground-to-satellite as well as inter-satellite quantum links in order to faithfully distribute entanglement around the globe. By showing the feasibility of quantum communication over a 143 km horizontal free-space link between the Canary Islands La Palma and Tenerife, we proved the practicability for such satellite-based systems. In this light the *Institute for Quantum Optics and Quantum Information* recently joined forces with the *Chinese Academy of Sciences* for the development and operation of a prototype quantum-communication satellite.

This thesis provides a detailed description of the theoretical and experimental research on long-distance multipartite quantum-communication in free-space under the supervision of Prof. Anton Zeilinger. The work was conducted at the *Vienna Center for Quantum Sciences and Technology* of the *University of Vienna* and the *Institute for Quantum Optics and Quantum Information* of the *Austrian Academy of Sciences*.

In the first chapter I will give a quick review of long-distance free-space quantum experiments performed after 2007. Another review of experiments that were carried out until 2007 can be found in my diploma thesis [12].

Chapter two provides a basic introduction to the fundamentals of quantum information, explaining the qubit and quantum entanglement. However, it is assumed that most of the fellow readers are familiar with the theoretical background.

The third chapter points out the experimental prerequisites for the implementation of the experiments. It explains the sources used for entanglement, the methods for polarization analysis, the Bell-state measurement and the characteristics of the atmospheric free-space link.

Chapter four gives an overview of the local infrastructure on the Canary Island La Palma and Tenerife, as well as a detailed description of the telescopes used and the experimental setups for our inter-island measurement campaigns.

The fifth chapter explains how data acquisition and analysis was realized in our experimental setups, with one measurement station being separated by 143 km from the remaining ones.

In chapters six I will present the measurement results of the long-distance free-space quantum experiments performed.

Finally I will conclude our findings in chapter seven and provide an outlook for future experiments and applications.

The appendix contains specification sheets of equipment, a preprint of our publication about the entanglement-swapping experiment and my final report for the European Space Agency regarding a high-speed adaptive-optics system.

1. Introduction

1.1. Overview of long-distance free-space experiments

In the past years several free-space quantum-communication experiments have been performed over various distances. Starting with fairly short free-space links in the order of hundreds of meters, extending the range up to 144 km in the inter-island experiments between the Canary Islands La Palma and Tenerife. An overview of these first trials from 2003 until 2007 is given in my diploma thesis [12]. Here I will give a short summary of long-distance free-space quantum-communication experiments performed since then.

High-fidelity transmission of entanglement over a high-loss free-space channel

In May 2009 Fedrizzi et al. [13] reported the high-fidelity transmission of entanglement over a 144 km high-loss free-space channel between the Canary Islands La Palma and Tenerife. The source for polarization entangled photon pairs was based on a periodically poled $KTiOPO_4$ (PPKTP) crystal in a bidirectionally pumped Sagnac-interferometer configuration. It produced $\sim 3.3 \times 10^6$ detected single photons and $\sim 10^6$ detected photon pairs per second. The two photons of each pair were transmitted to Tenerife by
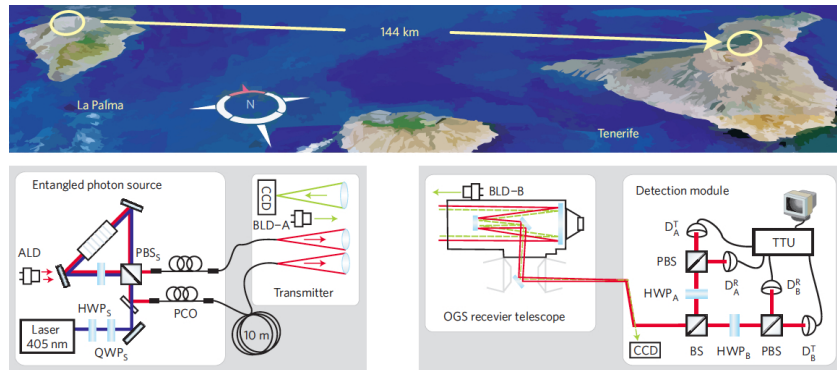

Figure 1.1.: The experimental scheme of the high-fidelity transmission of entanglement over a 144 km high-loss free-space channel by Fedrizzi et al. [13].

two telescopes mounted on a motorized platform. Each sending telescope consisted of a single-mode (SM) fibre coupler and $f/4$ best-form lens with a diameter of 7 cm. The receiver was a 1 m diameter reflector telescope of the European Space Agency (ESA). A bidirectional closed-loop tracking of the transmitter and the receiver telescopes was implemented to stabilize the free-space link and enhance the efficiency (figure 1.1).

In three consecutive nights a total of 10800 s of data was acquired with an average signal of 2500 single photons and 0.071 photon pairs per second. The net attenuation of the 144 km free-space link was 32 dB for single photons and 64 dB for photon pairs, which was exactly twice as large and therefore proved the independence of the two quantum channels. Finally the violation of a Clauser-Horne-Shimony-Holt (CHSH)-type Bell inequality with a measured parameter $S_{exp} = 2.612 \pm 0.114$ revealed that the transmitted photon pairs were still entangled after 144 km through turbulent atmosphere. This value violated the classical bound of $S_{cl} \leq 2$ by 5.4 standard deviations.

Feasibility of 300 km quantum key distribution with entangled states

Scheidl et al. [14] experimentally studied the feasibility of 300 km quantum key distribution (QKD) with entangled states and published their results in August 2009. They compared three different entanglement-based QKD setups (figure 1.2) over the 144 km free-space link between the Canary Islands La Palma and Tenerife.

In the first configuration the entangled-photon source was placed directly at Alice's location and only one photon was sent to Tenerife at a total two-photon attenuation of approximately 35 dB. With a local pair rate of 0.55 MHz and a total visibility of 86.2% they achieved a secure key rate of 24 bits/s.
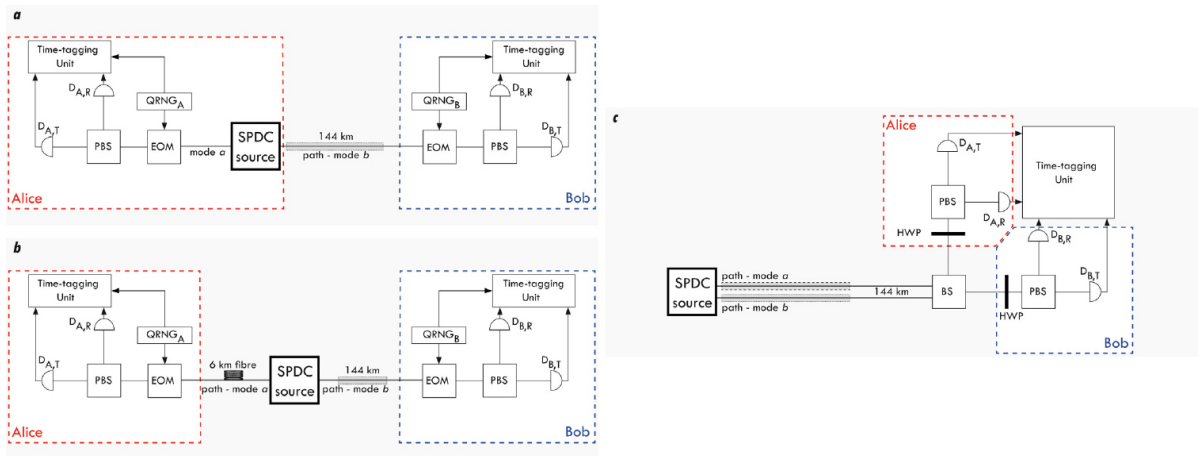

Figure 1.2.: The schemes of the three QKD scenarios in the experimental study of Scheidl et al. [14].

For the second experiment a 6 km fibre was introduced before Alice, which added additional loss resulting in a total two-photon attenuation of 58 dB. In this asymmetric scheme they measured a secure key rate of 0.6 bits/s at a local pair rate of 2.5 MHz and a total visibility of 86.2%.

In the third scenario both photons were transmitted to Tenerife through independent free-space channels, which can be seen as an effective realization of a symmetric "source in the middle" scheme. The results for this configuration were inferred from the experiment of Fedrizzi et al. [13], which yielded a secure key rate of 0.02 bits/s at a total two-photon attenuation of 71 dB.

The results showed that in symmetric schemes secure keys can be generated up to a channel attenuation of 70 dB or roughly 300 km link distance, while asymmetric setups fail in high loss scenarios.

Violation of local realism with freedom of choice

One year later in November 2010 Scheidl et al. [15] published a paper on the violation of local realism with freedom of choice. The experiment was performed over the 144 km free-space link between La Palma and Tenerife, closing the locality and the freedom-of-choice loophole simultaneously for the violation of a CHSH-type Bell inequality (figure 1.3). To close the locality loophole they space-like separated the measurement events on Alice's
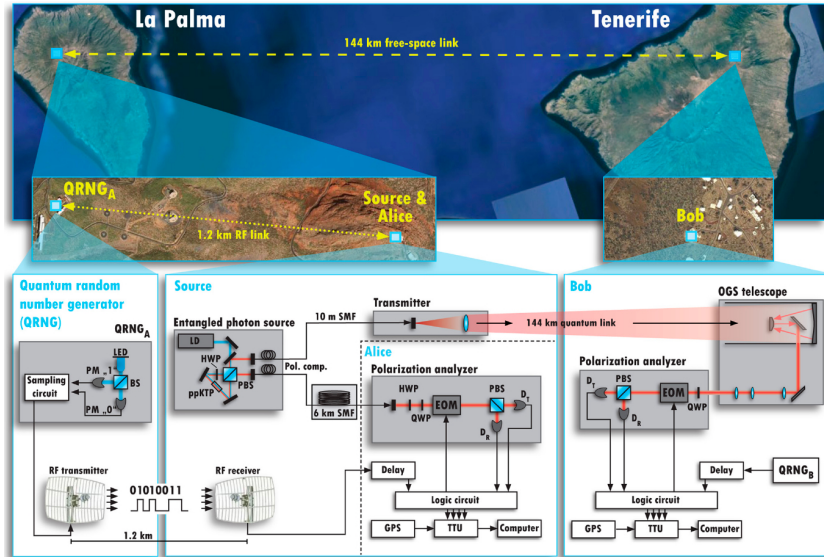

Figure 1.3.: The scheme of the experimental violation of local realism with freedom of choice by Scheidl et al. [15].

side from the measurement and setting choice on Bob's side and vice versa. Special relativity ensured that no signals about the measurement outcomes could influence the observed correlations. The freedom-of-choice loophole was closed using quantum random number generators (QRNGs) to randomly choose the settings of Alice and Bob. Additionally they had to space-like separate the choice events from the pair-emission events of the source.

In the experiment one photon was sent through a 6 km fibre coil to Alice directly next to the photon-pair source in La Palma, while the other photon was transmitted over the 144 km quantum channel to Bob in Tenerife. The QRNG on La Palma was placed around 1.2 km from the photon source, ensuring space-like separation of the setting choice and the photon emission. A classical radio link was used to send the QRNG outcomes to Alice. On Bob's side the random setting had to occur before any signal from the photon emission could arrive. In total they detected 19917 photon-pairs during four 600 s measurement runs and violated the CHSH-type Bell inequality by 16 standard deviations, with an experimental parameter $S_{exp} = 2.37 \pm 0.02$. These results showed the violation of local realism with both the locality and the freedom-of-choice loophole closed, only relying on the fair-sampling assumption.

Quantum teleportation and entanglement distribution over 100-kilometre free-space channels

In August 2012 Yin et al. [16] reported quantum teleportation of independent qubits over a single 97 km free-space channel (figure 1.4) and entanglement distribution over a symmetric two-link channel with a total separation of the entangled photon pairs of 102 km (figure 1.5).

The teleportation experiment was carried out next to Qinghai Lake in China, 3262 m above sea level. In the teleportation scheme Alice and Bob share an entangled photon pair distributed by a third party usually called Charlie. Alice and Charlie were located at Gangcha, north-west of the lake and Bob at Guanjing on the opposite side. Charlie produced the entangled photons with a pulsed source based on a type-II β-barium borate (BBO) crystal at an average 2-fold rate of 4.4×10^5 per second. Alice prepared the unknown state and the trigger photon in a collinear BBO crystal at a 2-fold rate of 6.5×10^5 per second, which resulted in a locally measured 4-fold coincidence rate of 2×10^3 per second. One photon of Charlie's entangled pair was overlapped with the unknown state on a beam splitter (BS) performing a so-called Bell-state measurement (BSM). The partner photon was transmitted through a 97 km free-space channel to

Bob. The sending telescope was an $f/7.5$ apochromatic refractor lens with a diameter of 127 mm and the receiver an off-axis reflecting telescope with a diameter of 400 mm. On Charlie's side link stabilization was achieved with a cascaded closed-loop control system consisting of a rotatable platform for coarse alignment and a fast steering mirror (150 Hz closed-loop bandwidth) for fine tracking. Bob used the telescope's motors for coarse alignment and a fast steering mirror (10 Hz closed-loop bandwidth) for fine tracking. The average link attenuation was ~ 44 dB which yielded 1171 coincidences during an effective time of 14400 s. They teleported the photons in the horizontal, vertical, plus, minus, right and left polarization states with all experimental fidelities well beyond the classical limit of 2/3 and gained an overall average fidelity of 80%.

In the second experiment Yin et al. demonstrated two-link entanglement distribution with a symmetric source-close-to-the-middle scheme. Charlie was moved to Haixin, an island in the middle of Qinghai Lake and Bob to Gonghe next to Guanjing. The distance between Charlie and Alice was 51.2 km, between Charlie and Bob 52.2 km and between Alice and Bob 101.8 km. Whereas Bob used the same receiver telescope, Alice used a Cassegrain reflector telescope with 600 mm diameter. With an average channel attenuation of 79.5 dB a total of 208 coincidences during an effective measurement time of 32000 s was recorded. The violation of a CHSH-type Bell inequality with an S parameter of $S_{exp} = 2.51 \pm 0.21$ showed entanglement between Alice's and Bob's photons with a significance of 2.4 standard deviations. In the experiment the locality loophole was closed due to space-like separation of Alice's and Bob's measurement events, as well as space-like separation of the measurement-setting choices.
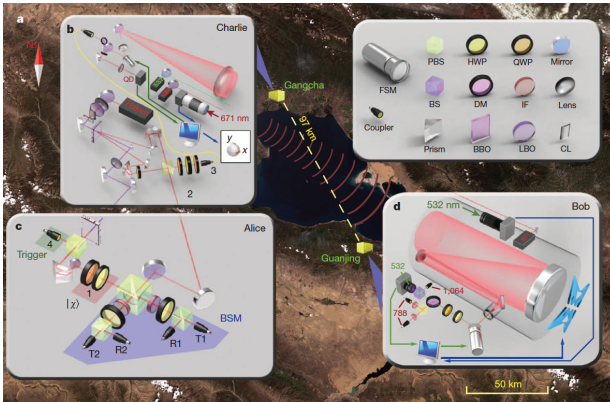

Figure 1.4.: The scheme of the 97 km quantum-teleportation experiment by Yin et al. [16].

Figure 1.5.: The scheme of the 102 km entanglement-distribution experiment by Yin et al. [16].

Quantum teleportation over 143 kilometres using active feed-forward

Only one month after Yin et al. had published their paper, Ma et al. [17] reported on quantum teleportation over a 143 km free-space link using active feed-forward in real-time. The experiment was performed between the Canary Islands La Palma and Tenerife (figure 1.6). In contrast to the previously presented inter-island experiments over 144 km, Alice and Charlie on La Palma were moved to the Jacobus Kapteyn Telescope (JKT) building of the Isaac Newton Group of Telescopes (ING), located ≈ 1 km closer to Bob on Tenerife. Alice generated polarization entangled photon pairs in a femtosecond-pulsed type-II BBO source and Charlie provided the heralded single photon to be teleported with a collinear type-II BBO crystal. One photon of the entangled pair was guided through a SM fibre to the sending telescope on the rooftop of the building and transmitted to Bob over 143 km of turbulent atmosphere. The entangled partner photon was overlapped on a fibre BS with Charlie's photon for the BSM.

In the first stage of the experiment only one out of four possible outcomes of the BSM was taken into account. The chosen outcome required no operation to be performed by Bob, as in this case Bob's photon was already in the state of the teleported input pho-
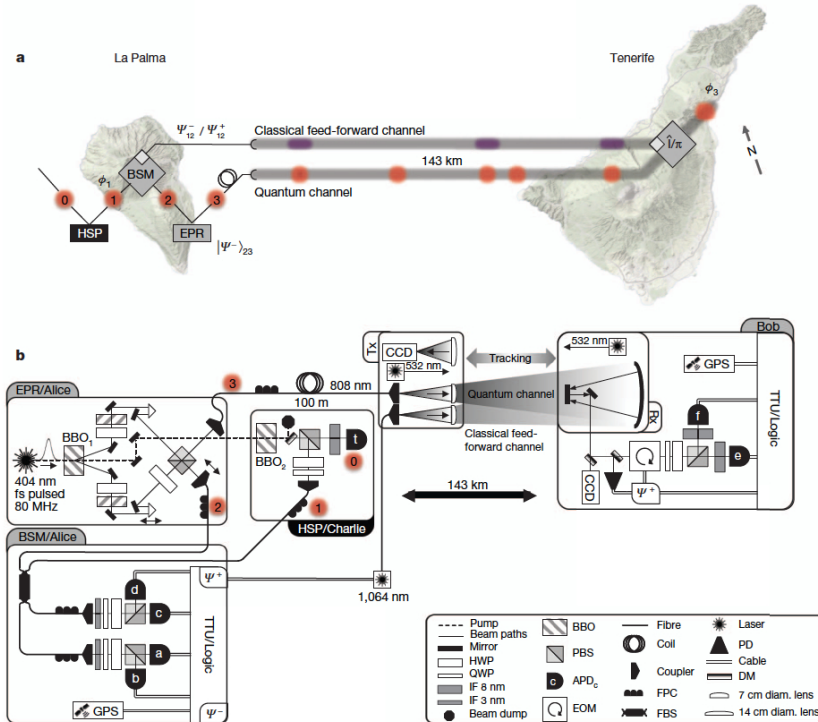

Figure 1.6.: The scheme of the quantum-teleportation experiment over a 143 km free-space link with real-time feed-forward [17].

ton. Successful quantum teleportation was demonstrated by the four input states with horizontal, vertical, plus and left polarization. All observed fidelities were well beyond the classical limit of 2/3 and the average state fidelity was $f = 0.863 \pm 0.038$. During these measurements the link attenuation varied from 28 dB to 39 dB. The teleportation procedure was characterized by quantum process tomography yielding a process fidelity of $f_{process} = 0.710 \pm 0.042$. This value is 5 standard deviations above the maximum classical process fidelity of 1/2.

In the second stage of the experiment real-time feed-forward of the BSM result over an additional 143 km classical channel was introduced. Conditional on the classical information Bob either had to perform a π phase shift between the horizontal and vertical component of his received photon, or do nothing at all. Quantum teleportation with active feed-forward was then showed for the plus and right polarization input states with state fidelities $f_{plus} = 0.760 \pm 0.050$ and $f_{right} = 0.800 \pm 0.037$. Again both fidelities were clearly above the classical fidelity bound, even though the average efficiency of the classical link was only 21.3%.

Quantum erasure with causally disconnected choice

In 2013 Ma et al. [18] published a long-distance quantum-erasure experiment with causally disconnected choice. The experiment was actually carried out already in 2008 with a setup that employed hybrid path-polarization entangled photon pairs, which were distributed over a 144 km free-space link between La Palma and Tenerife (figure 1.7).
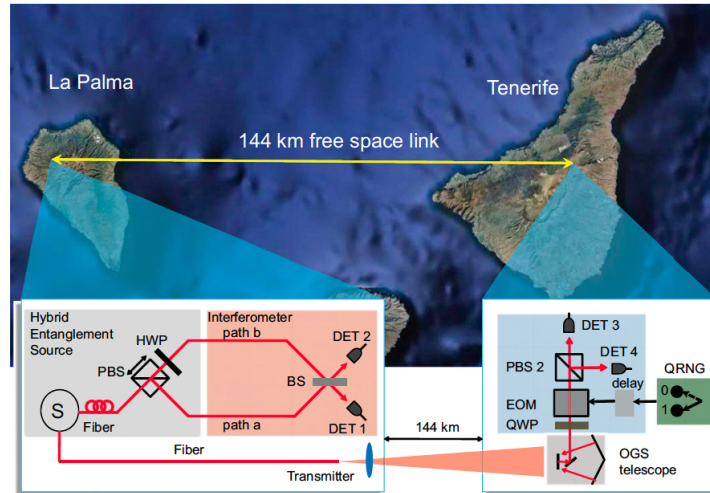

Figure 1.7.: The experimental scheme of the long-distance quantum-erasure experiment between the Canary Islands La Palma and Tenerife [18].

The path of a so-called system photon was entangled with the polarization of a so-called environment photon. Therefore the environment photon's polarization carries *welcher-weg* information of the system photon. Conditional on the chosen measurement basis for the environment photon the *welcher-weg* information was either acquired or erased, resulting in either the presence of no interference fringes or the observation of interference fringes of the system photon, respectively. More precisely a measurement in the horizontal/vertical polarization basis revealed *welcher-weg* information, whereas a measurement in the right/left-circular polarization basis erased the information. The choice of the measurement basis was performed by a QRNG, which was space-like separated from the source and the interference in order to rule out any luminal or sub-luminal communication between the events. A so-called *welcher-weg* parameter I in the case of a measurement in the horizontal/vertical basis and the visibility V of the interference fringes for the right/left-circular basis were obtained. For a link attenuation of 33 dB they measured $I \approx 0.93$ and $V \approx 0.76$, showing almost full *welcher-weg* information in the first case and high visibility in case the *welcher-weg* information was erased.

2. Quantum information fundamentals

2.1. The photonic qubit

In classical computing the basic unit of information is the bit, which can either attain the definite value "0" or "1". Its analogue in quantum information is the qubit, a two-level system with the computational basis states denoted by $|0\rangle$ and $|1\rangle$. For photons this two level system can be the polarization degree of freedom, e.g. the horizontal and vertical polarization states $|H\rangle$ and $|V\rangle$ corresponding to $|0\rangle$ and $|1\rangle$, respectively. Photonic qubits can easily be generated and manipulated, which makes them a convenient resource for quantum experiments.

2.1.1. The superposition principle

In contrast to classical systems, quantum systems can exist in a superposition state

$$|\Psi\rangle = \alpha \, |0\rangle + \beta \, |1\rangle \ \text{ with } \alpha, \beta \in \mathbb{C} \text{ and } |\alpha|^2 + |\beta|^2 = 1, \tag{2.1}$$

which is a linear combination of the basis states with complex coefficients. A neat way to visualize such superposition states is to represent them on a unit sphere, i.e. the Bloch sphere (figure 2.1). Equation 2.1 transforms to

$$|\Psi\rangle = \cos\left(\frac{\theta}{2}\right) |0\rangle + e^{i\varphi} \sin\left(\frac{\theta}{2}\right) |1\rangle, \tag{2.2}$$

with the zenit angle $0 \leq \theta \leq \pi$ and the azimuthal angle $0 \leq \varphi \leq 2\pi$.

The surface of the Bloch sphere represents pure states, whereas the interior of the sphere is filled with mixed states. The length of a given state vector is a measure for purity, therefore the most mixed state lies in the center. Furthermore, opposite states on the Bloch sphere are always orthogonal.

A photonic qubit with the basis states $|H\rangle$ and $|V\rangle$ can be represented on a Poincaré sphere (figure 2.2) by

$$|\Psi\rangle = \cos\left(\frac{\theta}{2}\right) |H\rangle + e^{i\varphi} \sin\left(\frac{\theta}{2}\right) |V\rangle, \tag{2.3}$$
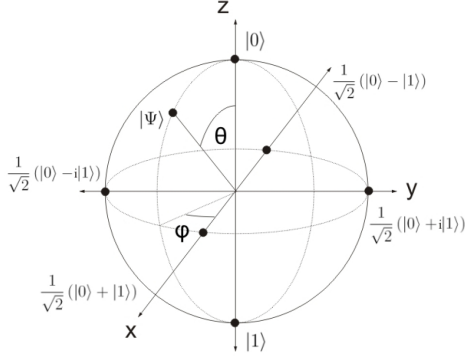
Figure 2.1.: The illustration of a general qubit on the Bloch sphere (equation 2.2).
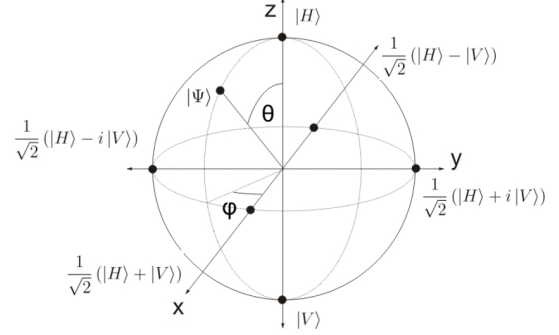
Figure 2.2.: The illustration of a photonic qubit on the Poincaré sphere (equation 2.3).

where the horizontal and vertical polarization states are the north and south pole of the sphere, respectively. The most important superpositions of these two states are the

$$
\begin{aligned}
\text{diagonal or plus state } |P\rangle =& \frac{1}{\sqrt{2}} \left(|H\rangle + |V\rangle \right), \\
\text{anti-diagonal or minus state } |M\rangle =& \frac{1}{\sqrt{2}} \left(|H\rangle - |V\rangle \right), \\
\text{right-handed circular state } |R\rangle =& \frac{1}{\sqrt{2}} \left(|H\rangle + i \, |V\rangle \right) \text{ and} \\
\text{left-handed circular state } |L\rangle =& \frac{1}{\sqrt{2}} \left(|H\rangle - i \, |V\rangle \right).
\end{aligned}
\tag{2.4}
$$

The three measurement bases H/V, P/M and R/L form a set of mutually unbiased bases, meaning that if a state is prepared in one of the bases, the measurement outcomes in another basis have equal probabilities of 1/2. For example, if one measures the state $|H\rangle$ in the R/L-basis, then 50% of the outcomes will be $|R\rangle$ and 50% will be $|L\rangle$.

2.1.2. The no-cloning theorem

Quite different from what we are used to in classical communication, an unknown single quantum state cannot be cloned nor amplified without losing its quantum feature. Triggered by a *Gedankenexperiment* of Nick Herbert [19] for a superluminal communication device, Wootters et al. [20] formulated the *no-cloning theorem* in their paper with the title *"A single quantum cannot be cloned"*. This means that it is impossible to get an exact copy of an arbitrary qubit without disturbing the quantum state of the original qubit. Mathematically this can be shown with a rather simple example. Let's assume there is a device available, which can copy an input qubit i onto a blank qubit b such

that the following relations are complied with

$$\begin{aligned} |0\rangle_i |0\rangle_b &\rightarrow |0\rangle_i |0\rangle_b \\ |1\rangle_i |0\rangle_b &\rightarrow |1\rangle_i |1\rangle_b . \end{aligned} \tag{2.5}$$

The linearity of quantum mechanics together with the superposition principle then result in

$$\begin{aligned} \frac{1}{\sqrt{2}} \left(|0\rangle_i + |1\rangle_i \right) |0\rangle_b &\rightarrow \frac{1}{\sqrt{2}} \left(|0\rangle_i |0\rangle_b + |1\rangle_i |1\rangle_b \right) \\ &\nrightarrow \frac{1}{\sqrt{2}} \left(|0\rangle_i + |1\rangle_i \right) \frac{1}{\sqrt{2}} \left(|0\rangle_b + |1\rangle_b \right) = \\ &= \frac{1}{2} \left(|0\rangle_i |0\rangle_b + |0\rangle_i |1\rangle_b + |1\rangle_i |0\rangle_b + |1\rangle_i |1\rangle_b \right) , \end{aligned} \tag{2.6}$$

where the output state is an entangled state (see section 2.2) rather than the desired copy of the input state. This proves that there is no such thing as deterministic perfect cloning of an unknown single quantum state, although there are several probabilistic and approximate cloning strategies [21–23]. A solution to faithfully transfer an unknown quantum state over arbitrary distances despite the no-cloning theorem is given by quantum teleportation (section 2.2.5).

2.2. Entanglement

Erwin Schrödinger coined the term *Verschränkung (Entanglement)* in 1935 in his work *"Die gegenwärtige Situation in der Quantenmechanik (The Present Situation in Quantum Mechanics)"* [24]. Entangled states exhibit much stronger correlations than classically possible and therefore are of great interest in quantum mechanics. A composite quantum system in a tensor product Hilbert space $\mathcal{H} = \bigotimes_{i=1}^{n} \mathcal{H}_n$ is entangled if it is not separable, i.e. if it cannot be written as a tensor product of its n subsystems. E.g. for a bipartite system the superposition state $|\Psi\rangle_{12} = \frac{1}{\sqrt{2}}(|H\rangle_1 |V\rangle_2 + e^{i\phi} |V\rangle_1 |H\rangle_2)$ with phase ϕ and subsystems 1 and 2 is entangled. Named after Einstein, Podolsky and Rosen (EPR) entangled pairs are often called EPR-pairs referring to EPR's paradox published in the paper *"Can quantum-mechanical description of physical reality be considered complete?"* [25].

2.2.1. The maximally entangled Bell states

The four maximally entangled Bell states

$$\left|\Psi^{\pm}\right\rangle_{12} = \frac{1}{\sqrt{2}}(\left|H\right\rangle_1 \left|V\right\rangle_2 \pm \left|V\right\rangle_1 \left|H\right\rangle_2)$$

$$\left|\Phi^{\pm}\right\rangle_{12} = \frac{1}{\sqrt{2}}(\left|H\right\rangle_1 \left|H\right\rangle_2 \pm \left|V\right\rangle_1 \left|V\right\rangle_2) \tag{2.7}$$

form a complete orthonormal basis in the four-dimensional Hilbert space. They are called maximally entangled as the reduced density matrices are multiples of the identity operator. Therefore a measurement on either single qubit will result in a random outcome, whereas a joint measurement on both qubits will yield perfect (anti-)correlations. These instantaneous correlations are presumed to hold for arbitrary distances, which is why they are also called non-local correlations. However, quantum non-locality is compatible with special relativity because one cannot use it for faster-than-light communication [26], as the measurement outcome of a single qubit is perfectly random. The $\left|\Psi^{-}\right\rangle$ state is the only antisymmetric state under exchange of particles and therefore also called singlet state, whereas the other three Bell states $\left|\Psi^{+}\right\rangle$ and $\left|\Phi^{\pm}\right\rangle$ are symmetric and called triplet states.

2.2.2. Conditions for entanglement

The separability criterion is the characteristic to reveal entanglement in a quantum system. If a given density matrix is separable, it means that the system is not entangled. In general there are only several sufficient conditions for non-separability or entanglement but no sufficient and necessary conditions are known. However, there are certain simple systems where also necessary conditions exist.

Violation of Bell's inequality

The violation of Bell's inequality [27] allows to exclude local realistic models and reveals non-local correlations in a bipartite system. Therefore, it is a sufficient condition to determine whether the system is entangled. However, satisfying the Bell inequality does not necessarily mean that the state is not entangled. In his famous inequality Bell puts the expectation values E of the joint measurements on both subsystems into relation and yields the inequality

$$|E(\vec{a}, \vec{b}) - E(\vec{a}, \vec{c})| \leq 1 + E(\vec{b}, \vec{c}) \tag{2.8}$$

for measurements along spin directions $\vec{a}$, $\vec{b}$ and $\vec{c}$. He shows that the singlet state maximally violates the equation if the measurement settings are chosen to fulfill $\vec{a} \cdot \vec{c} = 0$ and $\vec{a} \cdot \vec{b} = \vec{b} \cdot \vec{c} = \frac{1}{\sqrt{2}}$. In order to experimentally verify Bell's theoretical predictions, Clauser, Horne, Shimony and Holt (CHSH) [28] reformulated Bell's inequality in 1969 such that there are no perfect correlations and no perfect measurement devices required. Two years later in 1971 Bell published another version of his inequality [29] which then was also experimentally testable. Introducing four measurement settings $\vec{a}$, $\vec{b}$, $\vec{a'}$ and $\vec{b'}$, he derived a CHSH-type Bell inequality

$$S(\vec{a}, \vec{b}, \vec{b'}, \vec{c}) = |E(\vec{a}, \vec{b}) - E(\vec{a}, \vec{b'})| + |E(\vec{a'}, \vec{b'}) + E(\vec{a'}, \vec{b})| \leq 2. \qquad (2.9)$$

This new inequality reduces to its original form under the assumption $\vec{a'} = \vec{b'}$. For measurements along the angles $\alpha = 0$, $\beta = \frac{\pi}{4}$, $\alpha' = \frac{\pi}{2}$ and $\beta' = \frac{3\pi}{4}$ the inequality is again maximally violated with a so-called S-value of $S = 2\sqrt{2}$.

The original derivations are based on electrons, which are spin-$\frac{1}{2}$ particles. In order to maximally violate the equation in the case of photons, one has to halve the angles as photons are spin-1 particles. Therefore, polarization measurements along the directions $\alpha = 0$, $\beta = \frac{\pi}{8}$, $\alpha' = \frac{\pi}{4}$ and $\beta' = \frac{3\pi}{8}$ yield a maximal violation. Experimentally the expectation values E are retrieved by coincidence counts CC for the measurement angles and the corresponding orthogonal $\perp$ angles by the equation

$$E(\alpha, \beta) = \frac{CC(\alpha, \beta) - CC(\alpha, \beta^\perp) - CC(\alpha^\perp, \beta) + CC(\alpha^\perp, \beta^\perp)}{CC(\alpha, \beta) + CC(\alpha, \beta^\perp) + CC(\alpha^\perp, \beta) + CC(\alpha^\perp, \beta^\perp)}. \qquad (2.10)$$

Positive partial transpose

A more general test for entanglement is the positive partial transpose (PPT) criterion found by Peres [30] and Horodecki et al. [31] (also called Peres-Horodecki criterion). If a density matrix ρ is separable then its partial transpose

$$\rho^{T_2}_{m\mu;n\nu} \equiv \rho_{m\nu;n\mu} \qquad (2.11)$$

is always positive semidefinite $\rho^{T_2} \geq 0$ and therefore has no negative eigenvalues. Hence, if one of the eigenvalues is negative the partial transpose is not positive and the state is entangled, being a sufficient condition for entanglement. For the special cases of $2 \otimes 2$ (qubit-qubit) and $2 \otimes 3$ (qubit-qutrit) systems this is also a necessary condition, i.e. if a state is entangled its partial transpose is not positive semidefinite.

Entanglement witness

The disadvantage of the PPT criterion is that it assumes full knowledge of the density matrix. For the experimental detection of entanglement there are more useful operators, the so-called entanglement witnesses W [32–34]. They are Hermitian operators designed especially for distinguishing between separable and entangled states. W is called an entanglement witness if for all separable density matrices ρ_s the expectation value is positive $\text{Tr}[W\rho_s] \geq 0$, whereas for at least one entangled state ρ_e the relation $\text{Tr}[W\rho_e] < 0$ holds. Another big advantage of entanglement witnesses is that for every entangled state there exists a witness to detect it [31].

Still, there remains the task to construct a witness. In typical experimental setups where one has some *a priori* knowledge about the state to be generated, this can be achieved quite straightforward [35]. For an entangled state ρ_e there exists a negative eigenvalue $\lambda_- < 0$ of its partial transpose $\rho_e^{T_2}$ with the corresponding eigenvector $|\eta\rangle$. Applying the relation $\text{Tr}[AB^{T_2}] = \text{Tr}[A^{T_2}B]$ for general matrices A and B, one can show that $\text{Tr}[(|\eta\rangle\langle\eta|)^{T_2}\rho] = \text{Tr}[|\eta\rangle\langle\eta|\rho^{T_2}]$. Therefore

$$W = (|\eta\rangle\langle\eta|)^{T_2} \tag{2.12}$$

is an entanglement witness for ρ.

So for an entangled state $|\Psi\rangle = \alpha|HH\rangle + \beta|VV\rangle$ the entanglement witness is of the form

$$W = (|\Psi\rangle\langle\Psi|)^{T_2} = \begin{pmatrix} \alpha^2 & 0 & 0 & \alpha\beta \\ 0 & 0 & 0 & 0 \\ 0 & 0 & 0 & 0 \\ \alpha\beta & 0 & 0 & \beta^2 \end{pmatrix}^{T_2} =$$

$$= \left(\begin{bmatrix} \alpha^2 & 0 \\ 0 & 0 \end{bmatrix}^T \begin{bmatrix} 0 & \alpha\beta \\ 0 & 0 \end{bmatrix}^T \\ \begin{bmatrix} 0 & 0 \\ \alpha\beta & 0 \end{bmatrix}^T \begin{bmatrix} 0 & 0 \\ 0 & \beta^2 \end{bmatrix}^T \right) = \begin{pmatrix} \alpha^2 & 0 & 0 & 0 \\ 0 & 0 & \alpha\beta & 0 \\ 0 & \alpha\beta & 0 & 0 \\ 0 & 0 & 0 & \beta^2 \end{pmatrix} =$$

$$= \frac{1}{4}[\mathbb{1}\otimes\mathbb{1} + \sigma_z\otimes\sigma_z + (\alpha^2 - \beta^2)(\sigma_z\otimes\mathbb{1} + \mathbb{1}\otimes\sigma_z) + 2\alpha\beta(\sigma_x\otimes\sigma_x + \sigma_y\otimes\sigma_y)] \tag{2.13}$$

with the identity matrix $\mathbb{1}$ and the Pauli matrices

$$\mathbb{1} = \begin{pmatrix} 1 & 0 \\ 0 & 1 \end{pmatrix}, \sigma_x = \begin{pmatrix} 0 & 1 \\ 1 & 0 \end{pmatrix}, \sigma_y = \begin{pmatrix} 0 & -i \\ i & 0 \end{pmatrix} \text{ and } \sigma_z = \begin{pmatrix} 1 & 0 \\ 0 & -1 \end{pmatrix}. \tag{2.14}$$

This means that there are only three different measurement settings required to determine the witness. In the special case of $\alpha = \beta = \frac{1}{\sqrt{2}}$ equation 2.13 reduces to

$$W = \frac{1}{4}[\mathbb{1} \otimes \mathbb{1} + \sigma_x \otimes \sigma_x + \sigma_y \otimes \sigma_y + \sigma_z \otimes \sigma_z] =$$

$$= \frac{1}{2} \begin{pmatrix} 1 & 0 & 0 & 0 \\ 0 & 0 & 1 & 0 \\ 0 & 1 & 0 & 0 \\ 0 & 0 & 0 & 1 \end{pmatrix} = \frac{1}{2}\mathbb{1} \otimes \mathbb{1} - \frac{1}{2} \begin{pmatrix} 0 & 0 & 0 & 0 \\ 0 & 1 & -1 & 0 \\ 0 & -1 & 1 & 0 \\ 0 & 0 & 0 & 0 \end{pmatrix} =$$

$$= \frac{1}{2}\mathbb{1} \otimes \mathbb{1} - \left|\Psi^-\right\rangle\left\langle\Psi^-\right| = \frac{1}{2}\mathbb{1} \otimes \mathbb{1} - F_{\Psi^-}. \tag{2.15}$$

Therefore the entanglement witness is connected with the state fidelity F via the relation $\langle W \rangle = \frac{1}{2} - \langle F \rangle$. Hence the state fidelity and the entanglement witness can be measured with only three coincidence probabilities, namely $\sigma_x \otimes \sigma_x$, $\sigma_y \otimes \sigma_y$ and $\sigma_z \otimes \sigma_z$. This corresponds to coincidence measurements in the P/M, R/L and H/V-basis on both particles, respectively. With the $|\Psi^-\rangle$-state fidelity $\langle F_{\Psi^-} \rangle = \frac{1}{4}[\mathbb{1} \otimes \mathbb{1} - \langle \sigma_x \otimes \sigma_x \rangle - \langle \sigma_y \otimes \sigma_y \rangle - \langle \sigma_z \otimes \sigma_z \rangle]$ and the visibilities in the three bases being $V_{P/M} = -\langle \sigma_x \otimes \sigma_x \rangle$, $V_{R/L} = -\langle \sigma_y \otimes \sigma_y \rangle$ and $V_{H/V} = -\langle \sigma_z \otimes \sigma_z \rangle$ [36] the entanglement witness is given by

$$\langle W \rangle = \frac{1}{2} - \frac{1}{4}(1 + V_{HV} + V_{PM} + V_{RL}). \tag{2.16}$$

The visibility is defined as the ratio $V = (CC_{max} - CC_{min})/(CC_{max} + CC_{min})$ with the sum of the desired coincidence counts CC_{max} and the sum of the undesired coincidence counts CC_{min}.

2.2.3. Interferometric Bell-state measurement

Interference of two photons on a non-polarizing 50/50 beam splitter (BS) enables one to efficiently project onto one of the four Bell-states (equation 2.7) with equal probability of 1/4. If one overlaps two particles on a BS (figure 2.3) it depends on the symmetry of the wave function how they will interfere [37–40]. For fermions the Pauli principle

states that the particles must not end up in the same quantum state. Therefore, if two indistinguishable fermions interfere on a BS they will always take separate output modes. Indistinguishable bosons, however, will bunch at the BS and take the same output mode, although it is fully random which output mode they will take. Photon bunching was shown by Hong, Ou and Mandel (HOM) [41] where they revealed a minimum in the coincidence counts of the photons, the so-called HOM-dip. The afore mentioned statements are only correct if the internal degrees of freedom of the particles are ignored. Different interference phenomena arise from different symmetries of the total wave functions. For photons one also has to take into account the polarization degree of freedom in order to describe the interference effects correctly. As already mentioned, the four Bell-states (equation 2.7) can be divided in the antisymmetric singlet state $|\Psi^-\rangle$ and the symmetric triplet states $|\Psi^+\rangle$ and $|\Phi^\pm\rangle$. In order to obtain a total state with a symmetric wave function the polarization degree of freedom and the spatial degree of freedom have to be combined. The singlet state is antisymmetric in polarization, therefore the spatial part has to be antisymmetric as well and both photons will exit the BS in different output modes. On the other hand photons in the triplet states with symmetric polarization degree of freedom will bunch randomly into a single output mode. Polarization analysis in the H/V-basis can then discriminate the $|\Psi^+\rangle$-state from the $|\Phi^\pm\rangle$-states. Unfortunately, photons in the $|\Phi^\pm\rangle$-states will end up in the same detectors and cannot be distinguished with linear optics only [42–44]. The procedure of two-photon interference on a BS in combination with polarization analysis in each output mode (figure 2.4) is called Bell-state measurement (BSM).
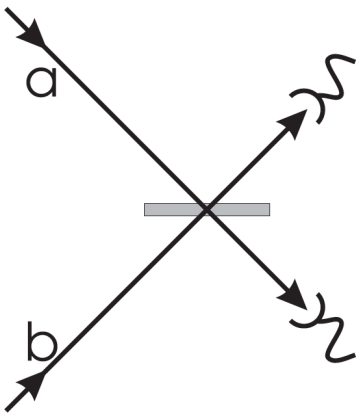

Figure 2.3.: Two-particle interference on a beam splitter (BS) [40]. The particles arrive at the BS in modes a and b.
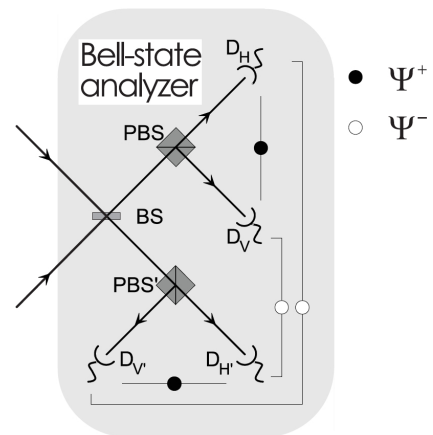

Figure 2.4.: Scheme of a Bell-state analyzer [40].

2.2.4. GHZ-states

The maximally entangled three-photon *Greenberger-Horne-Zeilinger* (GHZ) state [9; 10] is of the form

$$\left|\Psi^{GHZ}\right\rangle = \frac{1}{\sqrt{2}}(\left|H\right\rangle_1 \left|H\right\rangle_2 \left|H\right\rangle_3 + \left|V\right\rangle_1 \left|V\right\rangle_2 \left|V\right\rangle_3), \tag{2.17}$$

which is a superposition state of all photons being either horizontally H or vertically V polarized. Although, the measurement outcome of a single photon is perfectly random. The main advantage of a GHZ-state is that it can directly contradict local realism with in principle a single joint measurement on all three photons (the remaining statistics arise from experimental imperfections [45; 46]). Although Bell's inequality was derived assuming perfect correlations, its violation requires special measurement settings yielding only statistical predictions.

If we consider measuring the photons in the P/M-basis, also called x measurement, or in the R/L-basis, also called y measurement, the GHZ-state can be expressed in terms of these bases by using equation 2.4. In case of a measurement in the form of yyx the state transforms to

$$\begin{aligned}\left|\Psi^{GHZ}_{yyx}\right\rangle = \frac{1}{2}(\ &\left|R\right\rangle_1 \left|L\right\rangle_2 \left|P\right\rangle_3 + \left|L\right\rangle_1 \left|R\right\rangle_2 \left|P\right\rangle_3 \\ &+ \left|R\right\rangle_1 \left|R\right\rangle_2 \left|M\right\rangle_3 + \left|L\right\rangle_1 \left|L\right\rangle_2 \left|M\right\rangle_3).\end{aligned} \tag{2.18}$$

Again, the measurement on any single photon has perfectly random outcome, as well as the measurement on any two photons. Although, if we know the outcome of any two photons we can infer the result of the measurement on the third photon. For experiments in the form yxy and xyy we get analogous expressions by cyclic permutation in equation 2.18. One can see that whenever a measurement in the P/M-basis projects the photon in the state P, the remaining photons have opposite circular polarization. Whereas, when projected in the state M they have the same circular polarization.

Now we assume that photon i carries elements of reality X_i and Y_i to determine the outcomes for x and y measurements, respectively. The results P and M of X_i correspond to the values $+1$ and -1, similarly R and L of Y_i correspond to $+1$ and -1, respectively. Faithful reproduction of the quantum correlations (equation 2.18 and cyclic permutations) therefore yields the relations $Y_1Y_2X_3 = Y_1X_2Y_3 = X_1Y_2Y_3 = -1$. For a fourth xxx measurement local realism then predicts the possible results $M_1M_2M_3$, $M_1P_2P_3$, $P_1M_2P_3$ and $P_1P_2M_3$. This can be seen by the fact that $Y_iY_i = +1$ and therefore $X_1X_2X_3 = (X_1Y_2Y_3)(Y_1X_2Y_3)(Y_1Y_2X_3) = -1$. Quantum mechanics, however, predicts

the state to be of the form

$$\left|\Psi_{xxx}^{GHZ}\right\rangle = \frac{1}{2}(\left|P\right\rangle_1\left|P\right\rangle_2\left|P\right\rangle_3 + \left|P\right\rangle_1\left|M\right\rangle_2\left|M\right\rangle_3$$
$$+ \left|M\right\rangle_1\left|P\right\rangle_2\left|M\right\rangle_3 + \left|M\right\rangle_1\left|M\right\rangle_2\left|P\right\rangle_3), \tag{2.19}$$

which is the exact opposite of the local realistic predictions. Theoretically a single joint measurement can therefore contradict local realism.

Experimentally, the above relations cannot be perfectly tested, which is why Mermin [47] derived a Bell-type inequality for three-particle GHZ-states

$$|\langle xyy\rangle + \langle yxy\rangle + \langle yyx\rangle - \langle xxx\rangle| \leq 2. \tag{2.20}$$

Note that numerous Bell-type inequalities for N-particle GHZ-states have been published [47–50], all showing an exponential growth with N in violating these inequalities.

2.2.5. Four-photon protocols

Quantum teleportation

In order to transfer an unknown quantum state over arbitrary distances Bennett et al. [2] introduced the quantum-teleportation protocol. This way the no-cloning theorem, arising with any amplification, can be circumvented. The protocol exploits the entanglement of an auxiliary pair of photons 2 and 3

$$\left|\Psi^-\right\rangle_{23} = \frac{1}{\sqrt{2}}(\left|H\right\rangle_2\left|V\right\rangle_3 - \left|V\right\rangle_2\left|H\right\rangle_3) \tag{2.21}$$

in order to teleport the state of the input qubit 1

$$\left|\Psi\right\rangle_1 = \alpha\left|H\right\rangle_1 + \beta\left|V\right\rangle_1 \text{ with } |\alpha|^2 + |\beta|^2 = 1 \tag{2.22}$$

onto qubit 3. Alice therefore performs a BSM on qubits 1 and 2, forwarding the outcome to Bob via a classical channel. Depending on the result of the BSM Bob conducts the corresponding unitary operation on qubit 3, obtaining the teleported state of the input qubit 1 (figure 2.5). The no-cloning theorem is still obeyed, as the BSM destroys the state of the input photon, not giving any information about its individual state.

Mathematically the concept of the quantum-teleportation protocol can be seen by reformulating the total three-photon state in the basis of the Bell-states between qubits
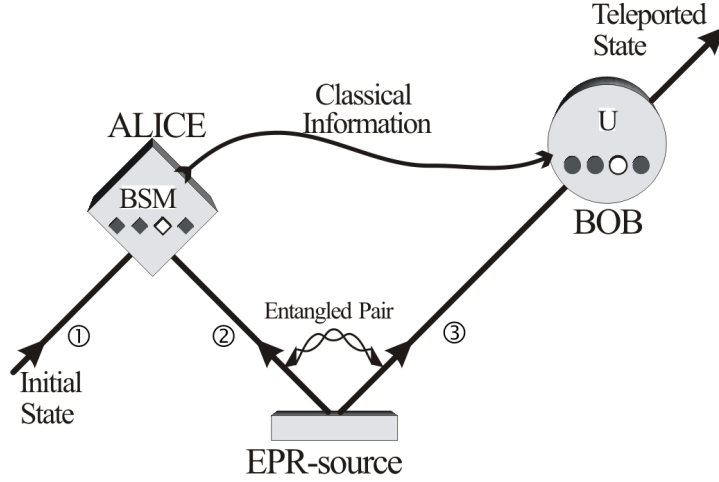
Figure 2.5.: The quantum-teleportation protocol [51]. Alice projects the input qubit 1 and qubit 2 of the entangled pair onto one of the four Bell-states and classically communicates the result to Bob. He performs the corresponding unitary transformation on qubit 3 and therefore yields an exact replica of the input qubit.

1 and 2

$$\left|\Psi\right\rangle_{123} = \left|\Psi\right\rangle_1 \otimes \left|\Psi^-\right\rangle_{23} = \frac{1}{2}[\left|\Psi^-\right\rangle_{12}(-\alpha\left|H\right\rangle_3 - \beta\left|V\right\rangle_3)$$
$$+\left|\Psi^+\right\rangle_{12}(-\alpha\left|H\right\rangle_3 + \beta\left|V\right\rangle_3)$$
$$+\left|\Phi^-\right\rangle_{12}(+\alpha\left|V\right\rangle_3 + \beta\left|H\right\rangle_3)$$
$$+\left|\Phi^+\right\rangle_{12}(+\alpha\left|V\right\rangle_3 - \beta\left|H\right\rangle_3)]. \qquad (2.23)$$

From equation 2.23 Bob's unitary operations on qubit 3 can be deduced depending on Alice's BSM outcomes

$$\left|\Psi^-\right\rangle_{12} \rightarrow \text{no operation required}$$
$$\left|\Psi^+\right\rangle_{12} \rightarrow \text{polarization dependent phase shift by } \pi$$
$$\left|\Phi^-\right\rangle_{12} \rightarrow \text{polarization rotation by } \pi/2$$
$$\left|\Phi^+\right\rangle_{12} \rightarrow \text{polarization dependent phase shift by } \pi \text{ and rotation by } \pi/2. \qquad (2.24)$$

Therefore Bob already has an exact replica of the input qubit in 1/4 of the cases, namely when Alice projects qubits 1 and 2 onto the singlet state $\left|\Psi^-\right\rangle_{12}$.

In an experimental implementation [51] a trigger photon T generated in a pair production process together with photon 1 is used for heralding the presence of the input photon. This gives a total four-photon state of

$$\left|\Psi\right\rangle_{T123} = \left|T\right\rangle \otimes \left|\Psi\right\rangle_{123}. \qquad (2.25)$$

Entanglement swapping

Entanglement swapping was introduced in 1993 by Żukowski et al. [6] representing an extension of the quantum-teleportation protocol to two entangled pairs. Generally speaking entanglement swapping is teleportation of entanglement as now the input qubit 1 is entangled to qubit 0 (figure 2.6). Projecting photons 1 and 2 onto the Bell-state basis by a BSM ultimately entangles photons 0 and 3 even though they were independently generated and share no common past. This feature constitutes the fundamental resource of a quantum repeater [7], which is of great importance in future quantum-communication networks. It allows to distribute entanglement over large distances interconnecting remote quantum computers.

In the following the protocol will be explained with two entangled pairs in the singlet states

$$\left|\Psi^-\right\rangle_{01} = \frac{1}{\sqrt{2}}(\left|H\right\rangle_0\left|V\right\rangle_1 - \left|V\right\rangle_0\left|H\right\rangle_1) \text{ and}$$

$$\left|\Psi^-\right\rangle_{23} = \frac{1}{\sqrt{2}}(\left|H\right\rangle_2\left|V\right\rangle_3 - \left|V\right\rangle_2\left|H\right\rangle_3). \tag{2.26}$$

Analogous to the quantum-teleportation protocol the total state can be represented in the basis of the four Bell-states

$$\left|\Psi\right\rangle_{0123} = \frac{1}{2}[\left|\Psi^+\right\rangle_{12}\otimes\left|\Psi^+\right\rangle_{03} - \left|\Psi^-\right\rangle_{12}\otimes\left|\Psi^-\right\rangle_{03}$$
$$- \left|\Phi^+\right\rangle_{12}\otimes\left|\Phi^+\right\rangle_{03} + \left|\Phi^-\right\rangle_{12}\otimes\left|\Phi^-\right\rangle_{03}]. \tag{2.27}$$
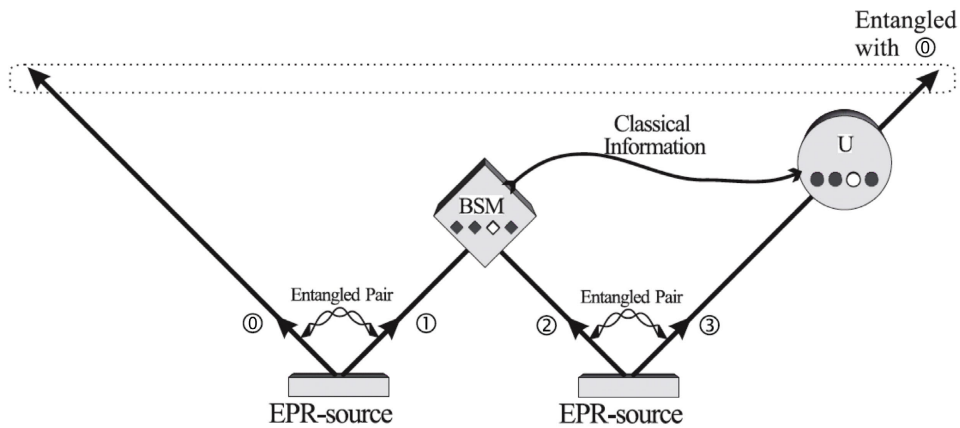

Figure 2.6.: The entanglement-swapping protocol [52]. A Bell-state measurement on qubits 1 and 2, each of an independent entangled pair, swaps the entanglement from qubits 0-1 and 2-3 onto qubits 1-2 and 0-3.

A quick look immediately reveals that a projection onto any Bell-state of qubits 1 and 2 entangles qubits 0 and 3 in the exact same state. In order to obtain a specific entangled state between qubits 0 and 3 e.g. the singlet state $|\Psi^-\rangle_{03}$ for all BSM outcomes, Alice classically communicates the result of her BSM to Bob who then applies the respective unitary operation on his qubit 3.

Four-photon GHZ-states

Replacing the non-polarizing 50/50 BS in the entanglement-swapping protocol with a polarizing beam splitter (PBS) [53; 54] allows for observing a four-photon GHZ-state of the form

$$\left|\Psi^{GHZ}\right\rangle = \frac{1}{\sqrt{2}}(|H\rangle\,|H\rangle\,|H\rangle\,|H\rangle + |V\rangle\,|V\rangle\,|V\rangle\,|V\rangle). \tag{2.28}$$

If both entangled pairs are prepared in the Bell-state $|\Phi^+\rangle = \frac{1}{\sqrt{2}}(|H\rangle\,|H\rangle + |V\rangle\,|V\rangle)$ this can be seen in figure 2.7 as a PBS transmits horizontal polarization and reflects vertical polarization. Eventually all photons are detected one in each of the output modes 0, 1, 2 and 3. In this case interference of photons 1 and 2 on the PBS within the coherence time erases which-path information and all four photons are in the superposition state of equation 2.28.
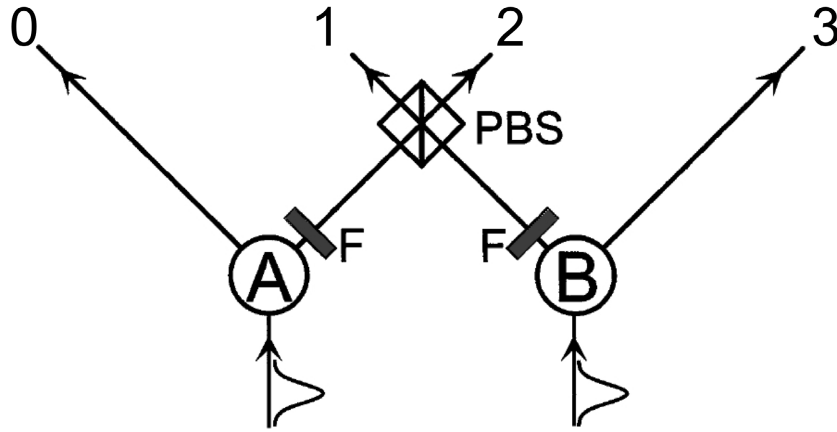

Figure 2.7.: The scheme of a four-photon GHZ experiment [53]. Two entangled pairs are generated in the Bell-state $|\Phi^+\rangle = \frac{1}{\sqrt{2}}(|H\rangle\,|H\rangle + |V\rangle\,|V\rangle)$. Oberlapping photons 1 and 2 on a polarizing beam splitter (transmitting horizontal polarization and reflecting vertical polarization) within the coherence time erases any information about the source of the photons. This eventually leads to a coincidence detection of all output modes 0, 1, 2 and 3, yielding the four-photon GHZ-state $\left|\Psi^{GHZ}\right\rangle = \frac{1}{\sqrt{2}}(|H\rangle\,|H\rangle\,|H\rangle\,|H\rangle + |V\rangle\,|V\rangle\,|V\rangle\,|V\rangle)$.

3. Experimental prerequisites

This chapter gives an overview of the basic prerequisites for our long-distance free-space experiments which are explained in detail in chapter 4.

3.1. Generation of entangled photons

We review the first observation of entanglement between two separated particles was achieved for polarization correlations of $\gamma^+\gamma^-$ emissions in positron annihilation [55; 56]. Later experiments with polarization-entangled photons from calcium cascade emissions [57–59] had the advantage of photons in the visible spectrum. The drawback, however, was that the photons were not deterministically emitted in opposite directions due to the random momentum of the atom.

The major breakthrough for generation of entangled photon pairs in terms of count rates and experimental feasibility was achieved with spontaneous parametric down-conversion (SPDC) due to second-order susceptibility $\chi^{(2)}$ in nonlinear crystals such as β-barium borate (BBO) [60; 61]. In a nonlinear medium a pump field E induces a polarization P of the form

$$P_i = \chi^{(1)}_{i,j}E_j + \chi^{(2)}_{i,j,k}E_{j,k} + \chi^{(3)}_{i,j,k,l}E_{j,k,l} + ...,\tag{3.1}$$

with the mth-order susceptibility $\chi^{(m)}$ [62]. The linear term $\chi^{(1)}$ is in the order of ~ 1 describing diffraction effects, the first nonlinear coefficient $\chi^{(2)}$ causes SPDC and is in the order of $\sim 10^{-12}$ m/V and $\chi^{(3)} \sim 10^{-24}$ m^2/V^2 is responsible for four-wave mixing effects. Due to $\chi^{(2)}$ a photon of the pump field can spontaneously be converted in a pair of photons which are called *signal* and *idler*. This process obeys energy and momentum conservation

$$\omega_p = \omega_s + \omega_i$$
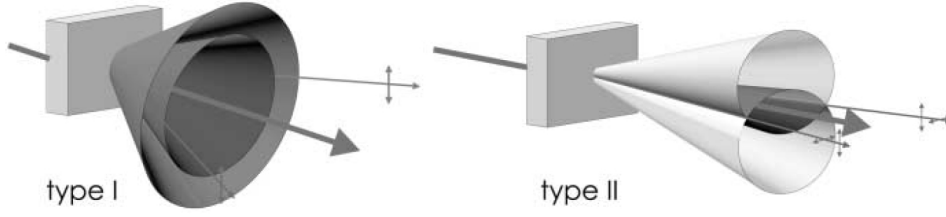$$\vec{k}_p = \vec{k}_s + \vec{k}_i\tag{3.2}$$

Figure 3.1.: The difference between type-I and type-II spontaneous parametric down-conversion [40].

which allows to observe entanglement in the position-momentum [63; 64] and time-energy [65; 66] degrees of freedom. Additionally there are two types of SPDC of which type-II can be used to generate polarization entanglement. In type-I SPDC a, for example, extraordinary polarized photon of the pump beam is converted into ordinary polarized signal and idler photons. Due to momentum conservation, which is also called phase-matching, the down-converted photons emit the crystal in cones of different colours centered around the pump beam. In the case of type-II SPDC an extraordinary polarized pump photon is converted into a pair of photons with orthogonal polarizations. Momentum conservation causes the signal and idler photons to exit the crystal on two cones, such that signal and idler lie on opposite sides of the pump beam (figure 3.1). In the intersection lines of the two cones one randomly observes either an ordinary or extraordinary polarized photon but always orthogonal polarizations with respect to each other. At this stage the photons still carry timing information due to different group velocities of the orthogonal polarizations in the nonlinear medium. Therefore they are rather described by the mixed state $\rho = \frac{1}{2}(|H_1\rangle |V_2\rangle \langle H_1| \langle V_2| + |V_1\rangle |H_2\rangle \langle V_1| \langle H_2|)$. For continuous wave (cw)-pumped schemes this distinguishability can be removed with a pair of crystals half the thickness of the down-conversion crystal one in each intersection line. Half-wave plates (HWP or $\lambda/2$) in front of the compensation crystals set to 45° flip the polarization in order to reverse the so-called walk-off effects induced by the down-conversion crystal. The longitudinal walk-off is a relative time delay between the ordinary and extraordinary photons due to different velocities in the crystal and can be compensated completely. The transverse walk-off causes different lateral displacement for both polarizations and an additional broadening for the ordinary beam due to different propagation directions in the medium. The relative lateral displacement can be compensated for, the spatial broadening of one beam, however, still remains after passing the compensation crystals. Erasing the distinguishability of the two photons by means

of compensation crystals translates the mixed state to the polarization-entangled state

$$|\Psi\rangle = \frac{1}{\sqrt{2}}(|H_e\rangle_1 |V_o\rangle_2 + e^{i\varphi} |V_o\rangle_1 |H_e\rangle_2), \quad (3.3)$$

with the relative phase φ between the ordinary and extraordinary photon. Tilting one of the compensation crystals changes φ and one can adjust the phase to a value of 0 or π in order to obtain the Bell-states $|\Psi^+\rangle$ or $|\Psi^-\rangle$, respectively.

In the case of pumping the nonlinear crystal with ultrashort pulses there arises an additional distinguishability between the signal and idler photon due to different spectra. The shorter the pulses the larger the bandwidth of the pump due to the time-energy uncertainty. An increased pump bandwidth translates into a broader spectrum of the down-converted photons. In a birefringent medium the phase-matching function is asymmetric in its frequency arguments causing the spectrum of the ordinary polarized photon to be broader than the one of the extraordinary polarized photon [67]. Kim et al. [68; 69] developed a scheme to decouple the spectral distinguishability from the polarization degree of freedom and therefore enhance the entanglement quality (figures 3.2 and 3.3). When flipping the polarization of a photon in one arm and interfering both on a polarizing beam splitter (PBS) all extraordinary polarized photons end up in one detector and all ordinary polarized photons in the other detector regardless of their polarization. Thus, photons with different spectra are separated and the spectral distinguishability is erased. The flip of polarization in one arm of the spectral-compensation scheme changes
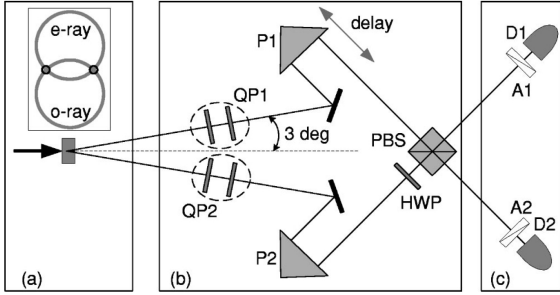
Figure 3.2.: The spectral compensation scheme of Kim et al. [69]. In one arm the polarization of the photon is flipped before overlapping both photons on a polarizing beam splitter (PBS). This scheme ensures that the extraordinary polarized photons only exit in one output arm of the PBS and all ordinary polarized photons in the other output arm.

Figure 3.3.: The two possible paths of the photon pairs. Either both photons are reflected at the polarizing beam splitter (left) or both photons are transmitted. Regardless of the polarization the extraordinary and ordinary polarized photons always exit at different output arms [70].

37

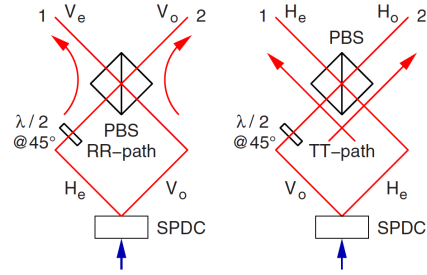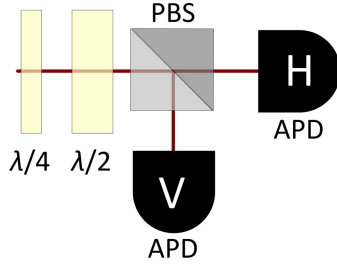|	H/V	P/M	R/L
QWP	0°	45°	45°
HWP	0°	22.5°	0°

Figure 3.4.: The scheme for a polarization measurement. A quarter-wave plate $\lambda/4$ and half-wave plate $\lambda/2$ rotate the polarization into the computational H/V-basis and a polarizing beam splitter separates the orthogonal components.

Table 3.1.: The settings of the quarter-wave plate (QWP) and half-wave plate (HWP) for a polarization measurement in one of the three mutually unbiased bases.

the original Bell-states $|\Psi^+\rangle$ or $|\Psi^-\rangle$ to $|\Phi^+\rangle$ or $|\Phi^-\rangle$, respectively. This can be revoked by another polarization flip in one output arm of the PBS.

3.2. Polarization measurement

An arbitrary polarization measurement of a photon can be achieved with a quarter-wave plate (QWP or $\lambda/4$) and a HWP followed by a PBS. The wave plates allow for rotation of any point on the Poincaré sphere into the computational H/V-basis and the PBS separates the orthogonal components (figure 3.4). For measurements in the three mutually unbiased bases the QWP and HWP settings are given in table 3.1. Single-photon counters in each output of the PBS detect the incident photons. Typical silicon avalanche photodiodes (APDs) have a detection efficiency of roughly 40% and are operated in Geiger mode. In this mode a photodiode is reverse biased above the breakdown voltage, such that a single photon can trigger a self-sustaining avalanche multiplication process. The resulting current gets transduced into a logic pulse [12].

3.3. Bell-state measurement

In section 2.2.3 the concept of a Bell-state measurement (BSM) has already been introduced. Here I want to mention the constraints for an experimental implementation. In order to observe interference of two independent photons on a beam splitter (BS) one has to render them indistinguishable by overlapping them within their coherence time τ_c. One approach to increase τ_c is narrow spectral filtering of the down-converted photons.

Standard interference filters in the visible spectrum exhibit a bandwidth of down to 1 nm which leads to $\tau_c = \frac{l_c}{c} = \frac{\lambda^2}{c \cdot \Delta\lambda} \approx 1$ ps. So far there are no APDs commercially available with a sufficient timing resolution. One can filter even stronger, e.g., with a Fabry-Pérot etalon in order to increase the coherence time to a level where state-of-the-art detectors can meet the temporal requirements. The drawback, however, is a substantial loss in count rates.

A different approach is to use ultrashort pulses as a pump for the SPDC together with standard interference filters. With off-the-shelf laser systems a pulse duration of 140 fs at a repetition rate of 80 MHz is available. Thus, filters for coherence times in the order of pico seconds erase practically every which-path information of the interfering photons, while still achieving fairly high count rates. The resulting coincidence window can be expanded just below the repetition period of the pump pulses, which is well within the temporal constraints of conventional APDs.

3.4. Free-space quantum channel

Free-space communication channels near ground strongly depend on the influence of the turbulent atmosphere and weather conditions. One therefore aims to install optical ground stations for satellite communication at elevated sites with thinner atmosphere and low cloud coverage throughout the whole year. The remaining atmospherical effects cause an increased channel loss due to absorption, scattering and refractive index fluctuations [71; 72].

3.4.1. Vacuum beam propagation

Even in the optimal case of vacuum beam propagation between satellites, the diffraction limit puts a lower bound on the beam diameter at the receiver. In order to predict the beam propagation of an electromagnetic wave in vacuum [73], one has to solve the wave equation for the electric field $\vec{E}$

$$\vec{\nabla}^2 \vec{E} = \frac{1}{c^2} \frac{\partial^2 \vec{E}}{\partial t^2}. \tag{3.4}$$

Next to plane waves and spherical waves the set of transverse electromagnetic (TEM) waves are solutions of the wave equation with boundary conditions. The TEM modes are a combination of a Gaussian profile with a Laguerre polynomial for cylindrical symmetry and with a Hermite polynomial for rectangular symmetry. In both cases the lowest order

mode TEM_{00} corresponds to a Gaussian beam profile. The irradiance distribution of the Gaussian beam is described by

$$I(r, z) = I_0 \frac{2P}{\pi w^2(z)} e^{\frac{-2r^2}{w^2(z)}}, \tag{3.5}$$

with the total power P in the beam, the distance r from the optical axis, the propagation distance z and the beam radius $w(z)$ for which the intensity drops to $1/e^2$ of the peak intensity. This mode describes the propagation of the electromagnetic wave in a specific direction, which is why it forms a good approximation for the propagation of a laser beam in vacuum. At the beam waist $w_0 = w(z = 0)$ the wave front is planar. The wave-front curvature

$$R(z) = z \left[1 + \left(\frac{\pi w_0^2}{\lambda z} \right)^2 \right] \tag{3.6}$$

for a wave with wavelength λ increases to a maximum at the *Rayleigh* range

$$z_R = \frac{\pi w_0^2}{\lambda} \tag{3.7}$$

and decreases again towards a planar wave front in the limit $z \to \infty$. The Rayleigh range z_R is also the distance over which the beam radius spreads by $\sqrt{2}$, i.e. $w(z_R) = \sqrt{2}w_0$. It divides between the near-field or *Fresnel* region and the mid-range divergence. For the far-field or *Fraunhofer* region a distance much greater than z_R, typically $z > 10 \times z_R$ is applicable. The collimated waist region of a Gaussian beam can be extended over a distance twice the Rayleigh range by starting with an aperture of diameter D and slightly focusing to a waist with radius w_0. Together with the πw criterion, i.e. 99% of the total power is transmitted through an aperture with diameter $D = \pi w = \pi \sqrt{2} w_0$, the collimated range can be expressed in terms of the transmitting aperture size to

$$2z_R \approx \frac{D^2}{\pi \lambda}. \tag{3.8}$$

The width of a laser beam after a distance z depends on the wavelength λ and the beam waist w_0 in the form

$$w(z) = w_0 \sqrt{1 + \left(\frac{\lambda z}{\pi w_0^2} \right)^2} \tag{3.9}$$

and for a given distance L the optimum starting beam radius is

$$w_0^{opt} = \sqrt{\frac{\lambda L}{\pi}}. \tag{3.10}$$

3.4.2. Atmospheric influence

In the presence of the earth's atmosphere light gets attenuated and disturbed. Already in the 17$^{\text{th}}$ century the Dutch scientist Christiaan Huygens mentioned in his notes [74] *"...the trembling Motion of the Vapours our Atmosphere is full of near the Earth; which is likewise the Cause of the Stars twinkling...".*

Attenuation

The attenuation of light in the atmosphere is caused by absorption a and scattering γ. It is described by the simple form

$$I(\lambda, z) = I_0(\lambda)e^{-\alpha(\lambda)z} = I_0(\lambda)e^{-[a(\lambda)+\gamma(\lambda)]z} \qquad (3.11)$$

called *Beer's* law [75–77], which is derived from the fact that the fractional amount of flux scattered from the beam is

$$\frac{dI}{I} = -\alpha dz. \qquad (3.12)$$

Beer's law is only applicable under conditions that do not allow multiple scattering, either due to low scattering or a narrow field-of-view of the observer.

Absorption of electromagnetic radiation is caused by excitation of the atmospheric molecules' quantum configuration, such as the electronic, vibrational and rotational states. Ozone O_3 essentially absorbs everything below $\lambda < 200$ nm. The visible spectrum is more or less transparent except for some absorption lines from Oxygen O_2 and water vapour H_2O for $\lambda > 650$ nm. Infrared radiation is absorbed by water vapour and carbon dioxide CO_2 (see figure 3.5).

Scattering results from photon collision with atmospheric molecules and aerosols. The collision with air molecules and haze that are small compared to the wavelength λ is described by *Rayleigh* scattering. Its scattering coefficient is proportional to λ^{-4} and therefore negligible for $\lambda > 3$ μm in air. The collision with aerosols comparable in size of the wavelength λ is called *Mie* scattering. With increasing wavelength the scattering coefficient decreases rapidly towards the Rayleigh scattering case.

In order to predict the atmospheric transmittance depending on the wavelength, software packages such as LOWTRAN, MODTRAN, HITRAN, FASCODE and PCLNWIN are available [76].
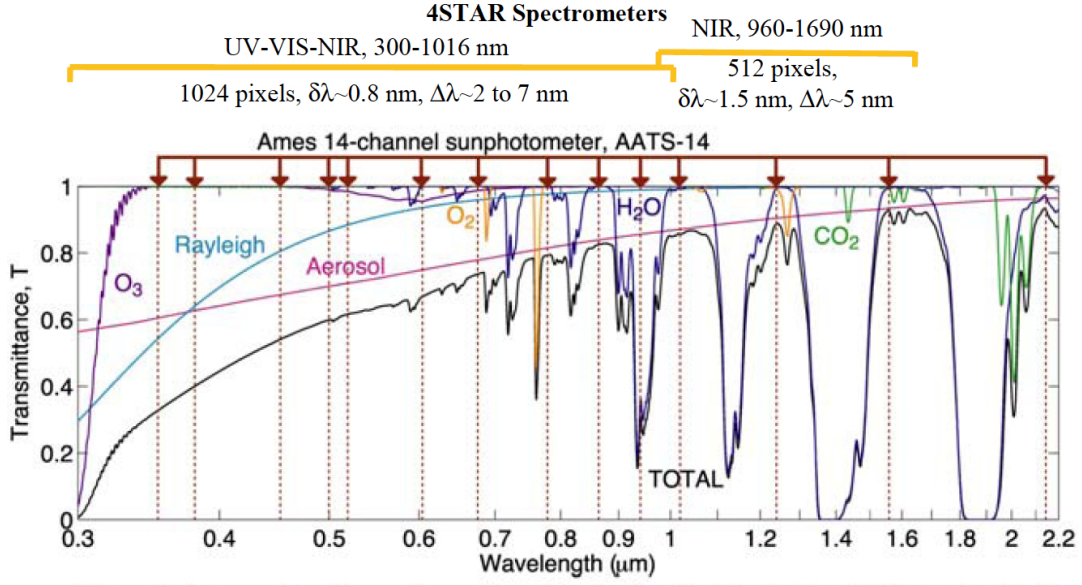
Figure 3.5.: The spectral transmittance T at sea level calculated using MODTRAN-4.3 with a Mid-latitude Summer atmosphere, a rural spring-summer tropospheric aerosol model (Vis = 23 km), and the sun at the zenith. Assumed O_3 = 332 DU, NO_2 = 0.22 DU. $\delta\lambda$ = spacing of pixel centers; $\Delta\lambda$ = slit/diffraction limited full width at half maximum [78].

Atmospheric beam propagation

In 1941 Andrey N. Kolmogorov [79; 80] introduced a simplified statistical model for the description of turbulence, which is commonly used for the prediction of wave propagation through random media [81]. If the laminar flow with a continuous velocity field turns into a turbulent flow, then the air masses break up into sub flows called turbulent eddies which become smaller and smaller until the supplied kinetic energy is dissipated. Therefore a multitude of eddies emerge ranging in size from the outer scale of turbulence $L_0 \approx 100$ m to the inner scale of turbulence $l_0 \approx 1$ mm. The point of transition from laminar to turbulent flow can be estimated by the dimensionless *Reynolds* number $Re = v_l l / \eta$ with the velocity fluctuation v_l within a domain of size l and the kinematic viscosity η. At the critical Reynolds number $Re \gtrsim 4000$ local unstable regions occur mainly caused by convection or a wind gradient over a relatively short distance called wind shear.

Kolmogorov's turbulence model is valid in the *inertial subrange* between l_0 and L_0 under the fair assumption of statistical homogeneity and isotropy of the turbulence. In this case the structure function $D_f(\vec{r}_1, \vec{r}_2) = \langle [f(\vec{r}_1) - f(\vec{r}_2)]^2 \rangle$ to characterize the strength of fluctuations is proportional to $|\vec{r}_1 - \vec{r}_2|^{\frac{2}{3}}$ with the distance $|\vec{r}_1 - \vec{r}_2|$ between

the observation points $\vec{r}_1$ and $\vec{r}_2$. This relation is also known as Kolmogorov's two-thirds law.

The propagation of an optical wave through a medium depends on its refractive index. For air the refractive index n can be approximated by

$$n(\vec{r}_1 - \vec{r}_2) = n_0 + n_1(\vec{r}_1 - \vec{r}_2)$$
$$\simeq 1 + 7.76 \times 10^{-5}(1 + 7.52 \times 10^{-3}\lambda^{-2})\frac{P(\vec{r}_1 - \vec{r}_2)}{T(\vec{r}_1 - \vec{r}_2)}, \qquad (3.13)$$

with pressure P in mbar, wavelength λ in μm and temperature T in kelvin. Therefore the refractive index is expressed by the sum of its mean value n_0 and a random fluctuation $n_1(\vec{r}_1 - \vec{r}_2)$. Together with Kolmogorov's model this leads to the refractive index structure function

$$D_n(\vec{r}_1, \vec{r}_2) = \langle [n(\vec{r}_1) - n(\vec{r}_2)]^2 \rangle = \begin{cases} C_n^2|\vec{r}_1 - \vec{r}_2|^{\frac{2}{3}} & \text{for } l_0 \ll |\vec{r}_1 - \vec{r}_2| \ll L_0 \\ C_n^2 l_0^{-\frac{4}{3}}|\vec{r}_1 - \vec{r}_2|^2 & \text{for } |\vec{r}_1 - \vec{r}_2| \ll l_0, \end{cases} \qquad (3.14)$$

with the refractive index structure constant C_n^2 or structure parameter. As pressure fluctuations are negligible, C_n^2 is mainly affected by temperature fluctuations. It typically ranges from 10^{-17} m$^{-\frac{2}{3}}$ for weak turbulence up to 10^{-13} m$^{-\frac{2}{3}}$ in the highly turbulent regime. The density plot in figure 3.6 shows a 35-days prediction of C_n^2 for an altitude up to 20 km above ground on La Palma [82].
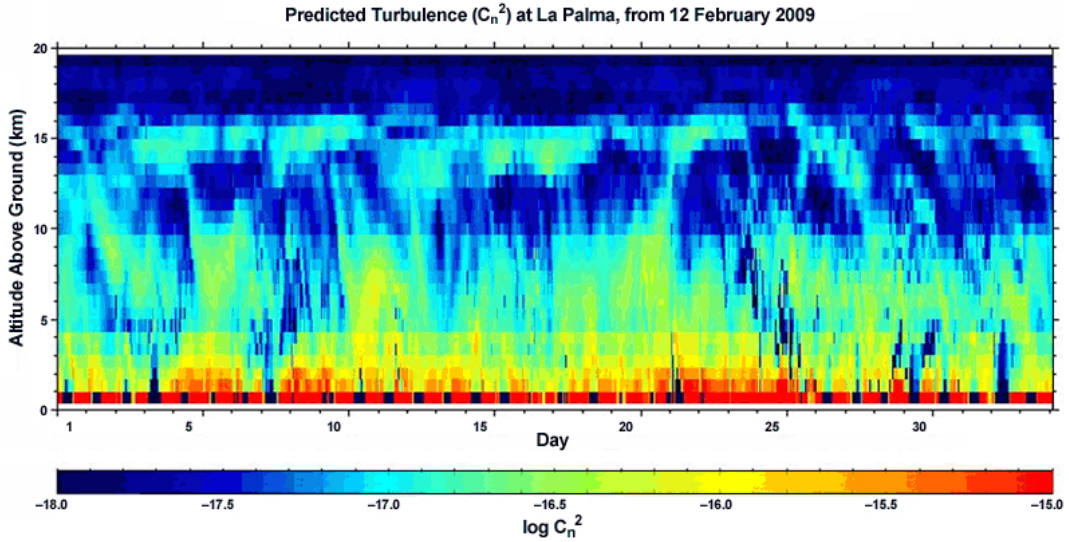

Figure 3.6.: A prediction of the structure parameter C_n^2 for 35 days on La Palma. The density plot illustrates the dependence on altitude above ground and shows almost no turbulence at altitudes above 17 km. The colour bar for C_n^2 ranges from 10^{-18} m$^{-\frac{2}{3}}$ (black) to 10^{-15} m$^{-\frac{2}{3}}$ (red) [82].

The effective radius w_{eff} of a Gaussian beam at the receiver after passage through turbulent medium generally depends on short-term and long-term beam spread. First of which is caused by turbulent eddies small compared to the beam diameter, resulting in beam broadening. The second effect is a beam wander caused by eddies larger than the beam diameter. A picture of the beam profile at the receiver taken with very short exposure would therefore show a beam broadened to a radius w_{st} being deflected from the optical axis by r_{bw} (figure 3.7) [76; 77]. For a long exposure time one therefore observes a broadened beam with a mean-square radius

$$\langle w_{eff}^2 \rangle = \langle w_{st}^2 \rangle + \langle r_{bw}^2 \rangle. \tag{3.15}$$

For weak turbulence the deflection of a beam with initial diameter D due to long-term beam wander can be expressed by the mean-square radius [83]

$$\langle r_{bw}^2(z) \rangle \simeq 1.92 C_n^2 z^3 D^{-\frac{1}{3}} \tag{3.16}$$

using the *Markov approximation*. In reference [84] the effective mean-square radius $\langle w_{eff}^2 \rangle$ for weak as well as strong turbulence is given by

$$\langle w_{eff}^2(z) \rangle \simeq \left(\frac{\lambda z}{\pi D}\right)^2 \left(1 + \left(\frac{D}{\rho_{sp}(z)}\right)^2\right) + \frac{D^2}{4}\left(1 - \frac{z}{F}\right)^2, \tag{3.17}$$

with the initial radius of curvature $-F$ and the transverse coherence radius ρ_{sp} for a
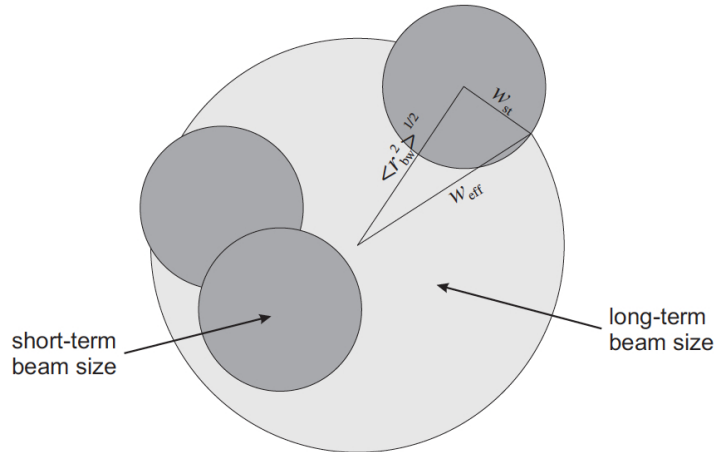

Figure 3.7.: Illustration of the effective beam radius w_{eff} in a turbulent medium caused by short-term beam broadening w_{st} and long-term beam wander r_{bw} [77].

spherical wave defined as

$$\rho_{sp}(z) = \left[1.46 k^2 z \int_0^1 (1-\xi)^{\frac{5}{3}} C_n^2(\xi z) d\xi \right]^{-\frac{3}{5}}$$
$$= \left[0.55 k^2 z C_n^2 \right]^{-\frac{3}{5}} \text{ for } C_n^2 = \text{constant.} \quad (3.18)$$

In the case of a collimated beam $F \to \infty$ the second term of equation 3.17 reduces to half the initial diameter D squared, whereas in case of focusing $z = F$ the term vanishes. This makes sense for $z \to 0$. From equations 3.15 - 3.17 the short-term beam spread $\langle w_{st}^2 \rangle$ for $\rho_{sp} \ll D < L_0$ and $z \lesssim k\rho_{sp}^2$ can be calculated to

$$\langle w_{st}^2(z) \rangle \simeq \left(\frac{\lambda z}{\pi D} \right)^2 \left(1 + \left(\frac{D}{\rho_{sp}(z)} \right)^2 \right) \left[1 - 0.62 \left(\frac{\rho_{sp}(z)}{D} \right)^{\frac{1}{3}} \right]^{\frac{6}{5}} + \frac{D^2}{4} \left(1 - \frac{z}{F} \right)^2 . \quad (3.19)$$

For strong turbulence the beam beam will not only be deflected but also break up into multiple beams and cause several randomly-distributed spots in a short-exposure image. The long-exposure picture, however, will show approximately the same effective radius w_{eff}. In the case of $kD^2 \ll z$ and $\rho_{sp} \ll D$ the mean-square radius of the beam wander is given by [85]

$$\langle r_{bw}^2(z) \rangle \simeq C_n^{\frac{8}{5}} k^{-\frac{1}{15}} z^{\frac{7}{15}} . \quad (3.20)$$

This means that for increasing path length or turbulence strength $\langle r_{bw}^2 \rangle$ saturates, which is in agreement with measured data of Table V in Ref. [83].

Turbulence parameters

There are several parameters to characterize the strength of the atmospheric turbulence. Here I want to give an overview and some useful estimations of the most common parameters. Nevertheless, one has to keep in mind that all these relations are estimations based on approximations of the turbulent atmosphere. Therefore the outcomes have to be treated with caution.

A simple estimate for the index of refraction structure constant C_n^2 for an altitude $h < 20$ km above ground is given by [75]

$$C_n^2(h) = \frac{1.5 \times 10^{-13}}{h} . \quad (3.21)$$

Alternatively the *Hufnagel-Valley* 5/7 model is a widely used expression for $C_n^2(h)$ which is named after the workers and results in a *Fried* parameter (see next parameter)

of $r_0 = 5$ cm and an isoplanatic angle of 7 μrad for a wavelength of 500 nm

$$C_n^2(h) = 8.2 \times 10^{-26} \left(\frac{h}{1000}\right)^{10} W^2 e^{-\frac{h}{1000}} + 2.7 \times 10^{-16} e^{-\frac{h}{1500}} + 1.7 \times 10^{-14} e^{-\frac{h}{100}}. \quad (3.22)$$

In this model the wind correlating factor is chosen to be $W = 21$ [75].

Fried has developed another useful parameter for the characterization of the atmosphere, the so-called Fried parameter r_0 [86]. It gives the diameter of a sending aperture which produces a diffraction-limited spot of the same diameter as that observed under atmospheric turbulence. It is connected to the structure parameter C_n^2 in the form

$$r_0 = \left[0.423k^2 sec(\beta) \int_0^L C_n^2(z)dz\right]^{-\frac{3}{5}}$$
$$= \left[0.423k^2 sec(\beta) C_n^2 L\right]^{-\frac{3}{5}} \text{ for } C_n^2 = \text{constant}, \quad (3.23)$$

with the wave number $k = 2\pi/\lambda$, the zenith angle β of the descending light waves and the distance L. For a horizontal link and constant C_n^2 Fried gives the relation

$$r_0 = 3.02 \left[k^2 L C_n^2\right]^{-\frac{3}{5}}. \quad (3.24)$$

A simple practical method for the estimation of r_0 is given by the measurement of the mean-square image motion σ^2 in a telescope with aperture diameter D via [75]

$$r_0 = 0.346 \left[\frac{\lambda^2}{\sigma^2 D^{\frac{1}{3}}}\right]^{\frac{3}{5}}. \quad (3.25)$$

The mean-square image motion at a receiver is caused by large turbulence cells inducing angle-of-arrival fluctuations α of the incoming wavefront. For a plane wave in nearly homogeneous turbulence the mean-square angle-of-arrival variance is given by [84]

$$\langle \alpha^2 \rangle \simeq \begin{Bmatrix} 2.19 \\ 2.92 \end{Bmatrix} \frac{\int_0^L C_n^2(z)dz}{D^{\frac{1}{3}}}, \quad \begin{matrix} l_0 \ll D \ll \rho_{pl} \\ \rho_{pl} \ll D \ll L_0, \end{matrix} \quad (3.26)$$

with the transversal coherence radius of a plane wave $\rho_{pl} \simeq r_0/2.103$.

The given parameters can help to estimate the influence of the random medium on a beam propagating through turbulent atmosphere. Nevertheless, due to many assumptions and approximations in the derivations of the parameters, they are mainly useful for phenomenological rather than precise predictions.

3.4.3. Compensation

The compensation of atmospherically induced wavefront disturbances is not only of great importance for astronomers but also for high-bandwidth optical communication protocols. Numerous techniques have been developed in order to counteract the impact of our earth's atmosphere.

Tracking

Long-term beam wander caused by turbulence cells in the order of the outer scale L_0 can extend across intervals as long as 30 s or even more. Variations at this very low temporal frequency can be compensated for by means of tracking systems with a closed-loop bandwidth of only 1 Hz or even less. This can be achieved by a simple lens focusing the signal of a beacon laser onto a tracking CCD together with a feedback loop controlling motorized actuators in order to keep the focal point at the same spot (see section 4.2 Transmitter).

Adaptive optics

Under strong turbulence conditions the wavefront distortions induced by small turbulence cells in the order of the inner scale l_0 can reach a temporal frequency of up to 1 kHz. Compensation of such wavefront errors can be achieved by adaptive-optics systems consisting of a wavefront sensing device and a deformable mirror to level out the wavefront deviations. A lot of adaptive-optics system use a Shack-Hartmann sensor in order to retrieve wavefront information. Such a sensor consists of a microlens array and a CCD for detecting the focal point position of each subaperture. From this information a discrete model of the overall shape of the wavefront can be computed which is used to command the actuators of the deformable mirror. The disadvantage of a Shack-Hartmann sensor is the relatively slow frame rate of typically 30 frames per second and the need for a bright light source in order to ensure enough exposure in each subaperture.

In the final report of my internship at the European Space Agency (ESA) I present a different approach to gain information about the wavefront in order to build a high-speed adaptive-optics system (see appendix A.3). This system is based on the fast measurement of a single metric, namely the intensity of light coupled into SM fibre and a stochastic parallel gradient descent algorithm in order to optimize the coupling into fibre. Field tests over 30 m at ESA showed a good performance of the system even under strong wind. Later tests over the 143 km horizontal free-space link at the Canary Island

47

revealed the limitations of the system under the influence of very strong turbulences. Although the adaptive-optics system slightly improved the link efficiency, a gain of only ~ 1 dB of the received power in Tenerife didn't justify the increased complexity of the overall experiment. Together with the ultra-low-noise single-photon detectors at the receiver in Tenerife, there was no urgent need for an adaptive-optics system anyhow. Therefore we decided to use our established bidirectional closed-loop tracking for link stabilization only.

4. Inter-island experiments

The following entanglement-swapping and GHZ experiments have been performed via a 143 km horizontal free-space link between the Canary Islands La Palma and Tenerife (figure 4.1). The *Observatorio del Roque de los Muchachos* (ORM) on La Palma and the *Observatorio del Teide* (OT) on Tenerife are hosted by the *Instituto de Astrofísica de Canarias* (IAC), also known as the *European Northern Observatory* (ENO). Located in the Atlantic Ocean roughly 360 km west of the Maroccan coast, the inter-island link has already been proven to represent a reliable testbed for several feasibility studies on the path towards a future space-based quantum-communication network (section 1.1).

Figure 4.1.: The 143 km horizontal free-space link between the Jacobus Kapteyn Telescope (JKT) on La Palma and the Optical Ground Station (OGS) on Tenerife (source: Google Earth, Data SIO, NOAA, U.S. Navy, NGA, GEBCO, Image Landsat).

4.1. Locations

La Palma

The Jacobus Kapteyn Telescope (JKT) building (28°45'40.2"N 17°52'41.0"W) [87] of the Isaac Newton Group of Telescopes (ING) on La Palma accommodated the main experimental setup consisting of two photon-pair sources, the BSM- and GHZ-module, Alice's polarization analysis and the transmitter telescope. At an altitude of ~ 2400 m the JKT provided a stable surrounding for the sensitive measurement apparatus. It shielded the equipment from the harsh environmental conditions outside the building and the advantage of permanent air conditioning ensured the required temperature stability for the experiments. In 2003 JKT was taken out of service as a common-user facility, which additionally minimized the disturbance in terms of vibrations and stray light during our measurement runs. The JKT is located close to the edge of the caldera and is therefore one of the few telescopes at ORM in direct line of sight with OT (figure 4.2).

Tenerife

On Tenerife we used the Optical Ground Station (OGS) (28°18'3.4"N 16°30'42.6"W) [88; 89] of the European Space Agency (ESA) as the receiver and base station for Bob's polarization analysis. The OGS is part of OT located at an altitude of ~ 2400 m in Izaña, about 13 km east by north of Mount Teide. It was built for optical laser communication

Figure 4.2.: Aerial view of the Jacobus Kapteyn Telescope (JKT) building (28°45'40.2"N 17°52'41.0"W) [87] on La Palma (source: Google Earth, GRAFCAN).

Figure 4.3.: Aerial view of the Optical Ground Station (OGS) (28°18'3.4"N 16°30'42.6"W) [88; 89] on Tenerife (source: Google Earth, GRAFCAN).
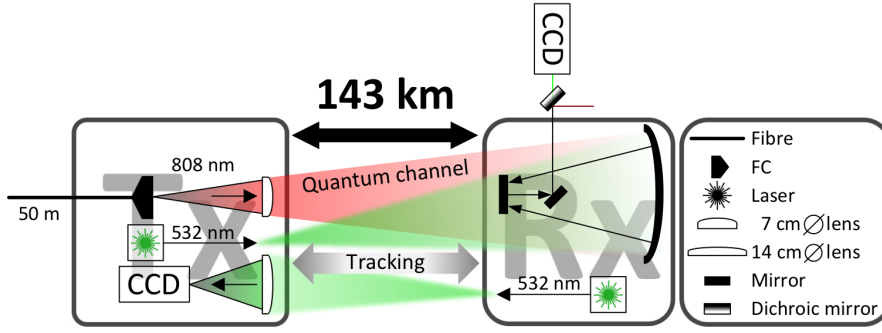
Figure 4.4.: The scheme of the closed loop tracking system between the transmitter Tx at the JKT on La Palma and the receiver Rx of the OGS on Tenerife. Two green beacon lasers at 532 nm wavelength created mutual guiding stars for the tracking system of the transceivers.

with satellites and therefore constitutes the ground based space infrastructure in our feasibility studies. The telescope is also used for surveillance and tracking of space debris. In contrast to astronomical telescopes the ability for satellite tracking allows for pointing at objects with an elevation even slightly below the horizon, which was required in order to establish the horizontal link between JKT and OGS (figure 4.3).

4.2. Transceivers

The 143 km quantum channel between the transmitter (Tx) at the JKT on La Palma and the receiver (Rx) of the OGS on Tenerife was stabilized with a bidirectional closed-loop tracking system. Green beacon lasers at 532 nm wavelength created mutual guiding stars, which were focused on tracking CCDs (figure 4.4). The tracking software gathered the position of the focal point on the CCD and controlled the actuators of the transceiver in order to keep the guiding star at its reference position. The closed loop feedback control was operated at roughly 1 Hz bandwidth and compensated for long term atmospheric drifts caused by the outer scale of turbulence L_0.

Transmitter

The sending telescope was assembled on a 60×30 cm^2 breadboard, which was mounted on a pivot bearing (figure 4.5). The whole platform was aligned by two high resolution *Stepper-Mike* actuators from *Physik Instrumente*[1] (PI). For the quantum channel a $f/4$

---

[1]Physik Instrumente (PI) GmbH Co. KG, Auf der Römerstrasse 1, 76228 Karlsruhe/Palmbach, Germany; www.physikinstrumente.com

achromatic best-form lens from *Lens-Optics*[2] with a focal length of $f = 280$ mm collimated the light out of SM fibre. Another PI stepper motor was used for alignment of the focal plane. All motors were driven by a PI *C-630 Apollo* controller. The SM fibre was mounted in a fibre adapter and centered on the sending lens. Blackout shielding around the sending lens minimized stray light into the tracking CCD during link alignment. A low-cost lens with a diameter of 140 mm and $f = 400$ mm focused the incident beacon light from Tenerife onto the tracking CCD from a disassembled *Logitech QuickCam Pro 9000*. The closed loop tracking algorithm was implemented with a self designed *LabView*[3] program. The 532 nm beacon laser pointing towards the OGS on Tenerife was mounted on the stationary lower stage of the transmitter, as the diameter of the beacon light after 143 km is by far big enough to constantly illuminate the whole receiver independent of any atmospheric fluctuations. During operation the transmitter was placed in a box on the rooftop of JKT (figure 4.6) and connected to the experimental setup via a 50 m SM fibre.

---

[2]LENS-Optics GmbH, Bürgermeister-Neumeyr-Straße 7, 85391 Allershausen, Germany; www.lens-optics.de

[3]National Instruments GmbH (Austria), Plainbachstr. 12, 5101 Salzburg-Bergheim, Austria; austria.ni.com

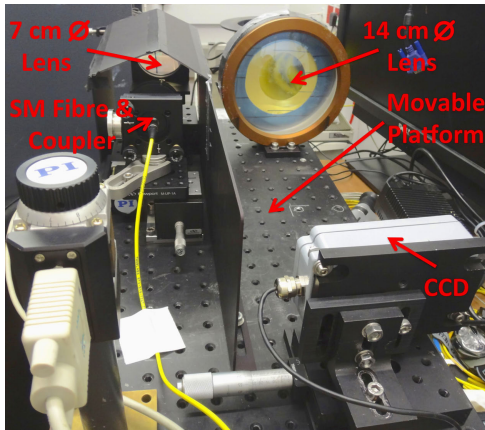**Figure 4.5.:** The movable transmitter platform with the ø = 7 cm sending lens collimated the light out of single-mode (SM) fibre. A ø = 14 cm lens focused the green guiding star from Tenerife onto the tracking CCD.
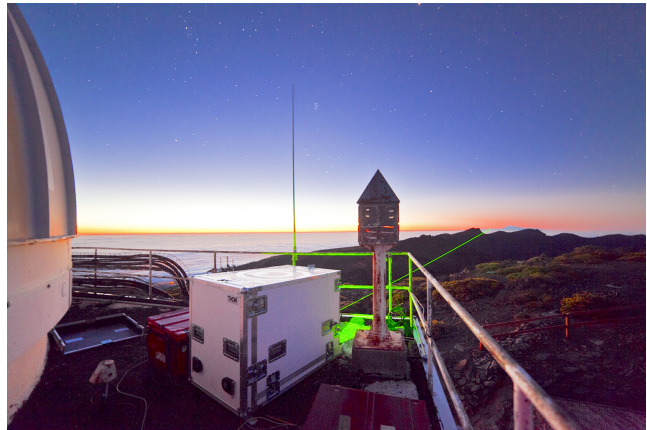

Figure 4.6.: Picture of the transmitter on the rooftop of JKT pointing towards OGS on Tenerife with a 532 nm beacon laser. Photo taken by Daniel Padrón, © IQOQI Vienna.

Receiver

The receiver on Tenerife is a 1 m diameter *Ritchey-Chrétien* reflecting telescope with hyperbolic primary and secondary mirrors mounted in an equatorial mount configuration. It can be operated in the wide field or small field *Cassegrain* modes with effective focal lengths of 4.5 m or 13.3 m, respectively. For stationary measurement devices, such as the Bob module in the inter-island experiments, it can be operated in the *Coudé* mode with 39 m effective focal length. Therefore additional mirrors reflect the light along the telescope's rotational axes to a fixed Coudé focus on an optical bench beneath the dome (figure 4.8). A dichroic mirror after the Coudé field stop reflected the received 808 nm quantum signal into Bob's polarization analyzer and transmitted the 532 nm beacon light from La Palma. The green tracking beam was focused onto the Coudé camera in order to establish the closed-loop pointing. A stationary 532 nm beacon laser was mounted next to the receiver creating the guiding star for the transmitter at JKT on La Palma (figure 4.4).

Figure 4.7.: Picture of the OGS pointing towards JKT on La Palma with a 532 nm beacon laser. Photo taken by Daniel Padrón, © IQOQI Vienna.
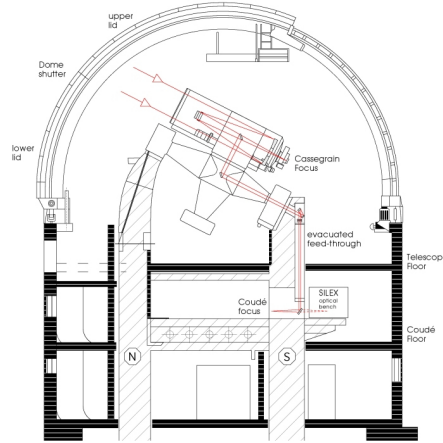
Figure 4.8.: The scheme of the ∅ = 1 m *Ritchey-Chrétien* receiver at the optical ground station on Tenerife. It can be operated in the *Cassegrain* and *Coudé* mode.

4.3. Experimental setups

The setups of the long-distance free-space entanglement swapping and GHZ-state experiments were implemented on a 150×125 cm^2 optical table in the first floor of the JKT building. Temperature stability was ensured by JKT's air-condition and an additional air-condition in the lab.

Second-harmonic generation

A *Chameleon Ultra II* [90] pulsed laser from *Coherent*[4] generated ultrashort pump pulses with a pulse duration of 140 fs and a gaussian beam width at the exit port of 1.2 ± 0.2 mm. At 808 nm wavelength we obtained an average optical power of ~ 3.5 W, which corresponds to a peak power of ~ 300 kW (specifications see figure A.1 in the appendix). An $f = 50$ mm lens focused the pump beam into a $10 \times 10 \times 0.7$ mm^3 type-I BBO crystal with the optical axis (OA) cut to an angle $\theta = 29.3°$ in respect to the beam propagation. In the nonlinear crystal the horizontally polarized 808 nm light was upconverted to a vertically polarized 404 nm beam by second-harmonic generation (SHG). Subsequent collimation of the 404 nm light was achieved by an $f = 75$ mm lens (figure 4.9). The SHG process had an efficiency of $\sim 60\%$ which made it necessary to perform a thorough spectral clean up in order to get rid of any remaining 808 nm photons. Therefore the upconverted beam was reflected by four dichroic mirrors highly reflective (HR) at 404 nm and anti-reflective (AR) at 808 nm wavelength (figure 4.10).

---

[4]Coherent (Deutschland) GmbH, Dieselstrasse 5b, 64807 Dieburg, Germany; www.coherent.com
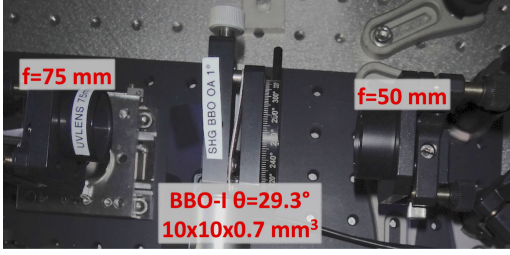
Figure 4.9.: Second-harmonic generation in a type-I BBO crystal. The 808 nm pump beam was focused into the crystal with an $f = 50$ mm lens and the upconverted 404 nm light was collimated with an $f = 75$ mm lens.
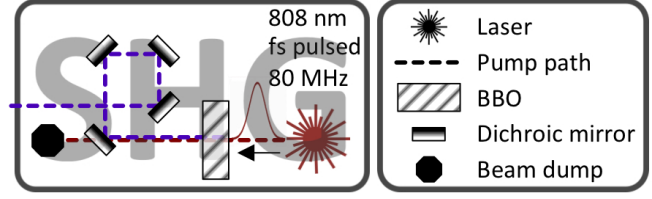

Figure 4.10.: Scheme of the second-harmonic generation and spectral clean up of the pump beam. The 808 nm femtosecond pulses of the pump laser are upconverted to 404 nm in a type-I BBO crystal. The remaining 808 nm light is separated from the 404 nm beam by an arrangement of four dichroic mirrors highly reflective at 404 nm and highly transmissive at 808 nm.

SPDC sources

After cleaning up the 404 nm pump beam it was guided to the first of two identical sources for polarization entangled photon pairs. An $f = 150$ mm lens focused the vertically polarized beam into a $10 \times 10 \times 2$ mm^3 type-II BBO crystal cut at $\theta = 41.5°$ (all BBOs were AR coated for 808 nm and 404 nm). The blue 404 nm pump beam was recollimated by another $f = 150$ mm lens and guided to the second source, where the pump was again focused into a BBO and finally blocked by a beam dump.

SPDC in the BBO generated correlated photon pairs at 808 nm wavelength on the intersection lines of the ordinary and extraordinary polarized output cones. The angle $\theta = 41.5°$ of the crystal's OA in respect to the propagation direction of the pump resulted in a 6° opening angle of the intersection lines. Two prisms HR coated for 808 nm reflected the photons in opposite directions through HWPs set to 45° in order to flip the polarization of each photon. In each arm a subsequent BBO crystal half the thickness of the down-conversion crystal compensated for the transverse and longitudinal walk-off and $f = 250$ mm lenses collimated the down-conversion beams. A delay line in each arm was realized with several mirrors, with two mirrors mounted on a motorized translation stage in order to ensure simultaneous arrival of the two photons at the subsequent PBS. In one of the two delay lines a HWP at 45° flipped the polarization before interference at the PBS. The PBS was mounted on a tip/tilt and rotation stage on top of a 2-axis translation stage movable in the plane of the optical table. Therefore the PBS could be properly aligned for spatial overlap of the transmitted and reflected beams. In each output port of the PBS a combination of a QWP, HWP and QWP was introduced before

coupling the down-converted photons into SM fibre. Both QWPs were fixed to 45° and the HWP was adjustable in order to simplify polarization compensation of the SM fibre in combination with the fibre polarization controller (FPC). Each fibre coupler (FC) consisted of a *New Focus*[5] *5726-H-B*, $f = 15.4$ mm aspheric lens and *New Focus*[5] *9091-M* SM fiber positioner, mounted on a 3-axis translation stage. The experimental scheme and setup are illustrated in figures 4.11 and 4.12, respectively. According to Kim's spectral-compensation scheme, one of the two FCs coupled the narrow bandwidth extraordinary polarized photons and the other one the broader ordinary polarized photons. The narrow-band photons of both SPDC sources had increased coherence times and were used for subsequent interference setups. In order to match the photons' optical path lengths we used SM fibres of different lengths for coarse balancing. For fine adjustment a motorized actuator for the z-translation stage of one FC was used. All linear-translation actuators were *Newport*[5] *LTA-HL* motors with a minimum incremental motion of 50 nm controlled by *Newport*[5] *SMC100CC* drivers.

The remaining photons with broader spectrum were sent to Alice in the JKT on La Palma and Bob in the OGS on Tenerife. Alice's photon was delayed by 100 m SM

---

[5]Newport Spectra-Physics GmbH, Guerickeweg 7, 64291 Darmstadt, Germany; www.newport.com
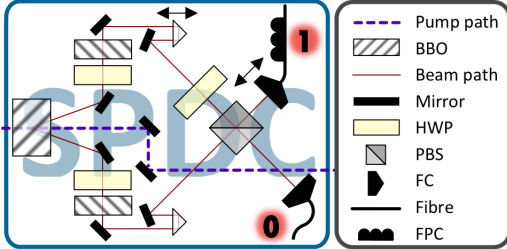
Figure 4.11.: Scheme of a spontaneous parametric down-convertion (SPDC) source with the spectral-compensation scheme of Kim et al. [68; 69].
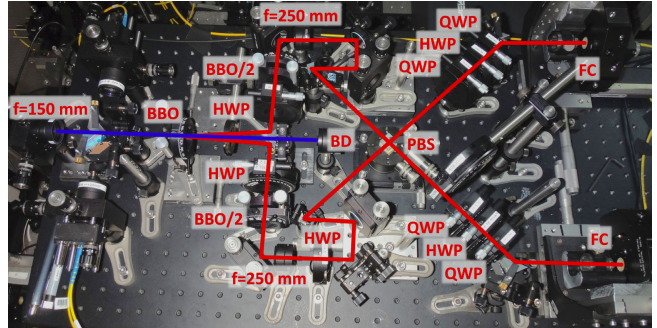
Figure 4.12.: Experimental setup of the second source for polarization entangled photon pairs. The 404 nm pump beam was focused ($f = 150$ mm) into a $10 \times 10 \times 2$ mm^3 type-II β-barium borate (BBO) crystal and stopped by a beam dump (BD). The down-converted 808 nm photons were guided through the setup containing half-wave plates (HWP), compensation BBOs (BBO/2), collimation lenses ($f = 250$ mm), a polarizing beam splitter (PBS) and quarter-wave plates (QWP). Fibre couplers (FC) were used to couple the entangled photons into single-mode fibres.

fibre before polarization analysis. Therefore Bob's photon already passed the 50 m SM fibre to the transmitter, being well ahead of any classical information about Alice's measurement outcome. Due to this space-like separation, there exists a moving reference frame in which Alice and Bob measure their photons simultaneously [15]. With respect to the reference frame of the source, this moving reference frame travels at a speed $v_{ref} = c^2 \cdot (t_B - t_A)/(x_B - x_A) = c^2 \cdot 477.3$ ns$/143127$ m $\approx 0.99975 \cdot c$, where c is the speed of light in vacuum, $t_B - t_A$ is the mean delay for a coincidence detection of Alice and Bob and $x_B - x_A$ is the distance between Alice and Bob. This reference speed yields a relativistic gamma factor $\gamma = (1 - v_{ref}^2/c^2)^{-1/2} \approx 44.55$ and therefore a Lorentz contracted separation between Alice and Bob of $\gamma^{-1} \cdot 143127$ m ≈ 3.2 km.

Alice

Alice's polarization analyzer comprised an SM FC with an interference filter (IF) and subsequent QWP, HWP and PBS, which allowed for projection on any desired polarization basis before detection by an APD in each of the PBS's orthogonal output ports. The detection events were logically combined with the BSM outcomes and recorded with a time tag from a time-tag unit (TTU) with a temporal resolution of 156 ps. The TTU's time reference was provided by a 10 MHz clock disciplined with the 1 pulse per second (PPS) signals of several global positioning system (GPS) satellites (figure 4.13).

In the experimental setup (figure 4.14) Alice was put in a light-tight box together
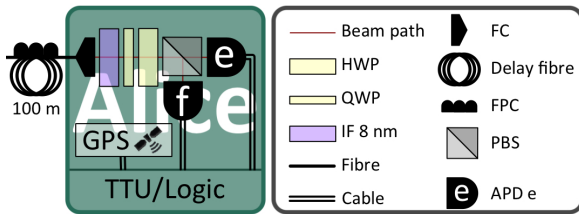
Figure 4.13.: Scheme of Alice's polarization analyzer. Her photon was delayed by a 100 m fibre and measured by detector e or f. The 1 pulse per second signal of the global positioning system (GPS) provided the time reference for the time-tag unit (TTU).
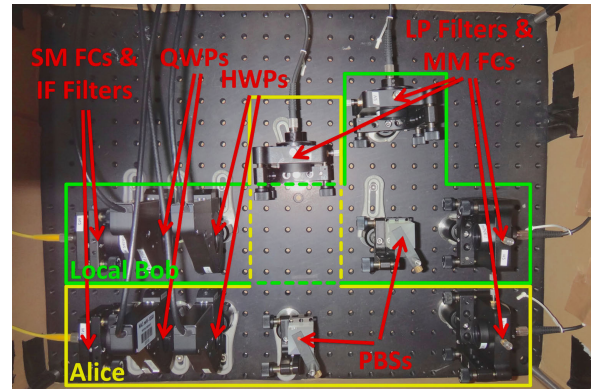
Figure 4.14.: Experimental setup of Alice and local Bob containing Single mode (SM) fibre couplers (FCs), interference filters (IFs), quarter-wave plates (QWPs), half-wave plates (HWPs), polarizing beam splitters (PBSs), long pass (LP) filters and multi mode (MM) FCs.

with an identical setup for local Bob, which was implemented for alignment purposes. Alice's photon was coupled out of SM fibre and collimated with a fixed-focus collimator. The photon passed an IF with a full width at half maximum (FWHM) of 8 nm at 808 nm wavelength and a QWP and HWP. All wave plates were mounted in *Thorlabs*[6] *PRM1/MZ8* motorized rotation stages and driven by *Thorlabs*[6] *TDC001* controllers. A PBS on a tip/tilt mount projected onto horizontal or vertical polarization by transmitting or reflecting the photon, respectively. In each output port of a PBS was a FC with a long pass (LP) filter blocking the wavelengths < 780 nm in order to reduce stray light into the multi-mode (MM) fibre to the APD. Again fixed-focus collimators were used for coupling into MM fibres. The single-photon counting module array *SPCM-AQ4C* [91] from *PerkinElmer*[7] was used for photon detection by Alice and local Bob (specifications see figure A.2 in the appendix).

Bob

After the transmission of Bob's photon via the 143 km free-space link (section 4.2) it was guided through the Coudé path to Bob's setup. A dichroic mirror right behind the Coudé focus transmitted the 532 nm beacon light to the tracking CCD and reflected the 808 nm quantum signal to the polarization analyzer. The measurement apparatus contained a QWP, HWP, PBS and free-space APDs in each output port of the PBS with IFs mounted on top for stray-light reduction (figure 4.15). The detector clicks were time-tagged with a TTU and stored for later analysis. Bob's TTU, logic and GPS-disciplined clock were identical to Alice's.

The experimental implementation of the Bob module is illustrated in figure 4.16. Before entering the module, the received quantum signal was collimated by an $f = 400$ mm lens. With the 39 m effective focal length of the 1 m diameter telescope in Coudé mode, this resulted in a collimated beam diameter of ~ 1 cm. Two auxiliary mirrors were introduced in order to freely steer the beam into a light-tight measurement box. The QWP and HWP inside the box were again mounted in motorized rotation stages from *Thorlabs*[6] and the PBS was mounted on a tip/tilt stage. Two $f = 50$ mm lenses, one in each output arm of the PBS, focused the beam on ultra-low dark-count APDs with ~ 20 dark-counts per second and an active area of ø= 500 μm [92]. IFs were directly attached to the detectors and had an FWHM of 8 nm at 808 nm wavelength.

---

[6]Thorlabs GmbH, Hans-Boeckler-Str. 6, Dachau/Munich 85221, Germany; www.thorlabs.de

[7]PerkinElmer Vertriebs GmbH, Feldstrasse 34, 2345 Brunn am Gebirge, Austria; www.perkinelmer.com

Figure 4.15.: Scheme of Bob's polarization measurement. A dichroic mirror transmitted the 532 nm tracking beam to the CCD and reflected the 808 nm quantum signal into the polarization analyzer. A time-tag unit (TTU) provided time stamps for each click in detectors g or h, synchronized to Alice by the 1 pulse per second signal of the global positioning system (GPS).

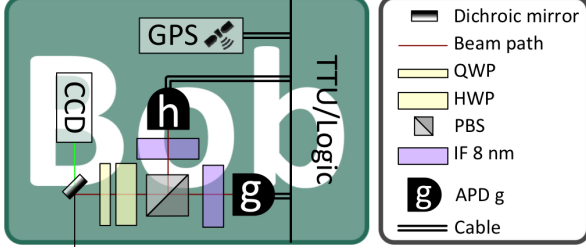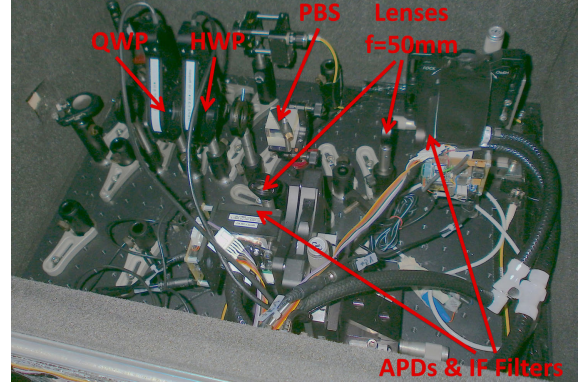**Figure 4.16.:** Experimental setup of the Bob module inside a light-tight box. The photons passed a quarter-wave plate (QWP), half-wave plate (HWP) and polarizing beam splitter (PBS) before focusing onto avalanche photodiodes (APDs) by $f = 50$ mm lenses. Interference filters (IFs) were directly attached to the APDs for stray-light reduction.

4.3.1. Entanglement-swapping experiment

The afore mentioned parts of the setup were in common use by both experiments. For our entanglement-swapping experiment the narrow-band photons of the two SPDC sources were subjected to a BSM in order to project these independent photons randomly onto one of the four Bell-states and therefore entangle Alice's and Bob's photon.

The experimental scheme and the total setup of the inter-island experiment is illustrated in figure 4.17.

Scheme

The SPDC sources generated the entangled photons 0-1 and 2-3 in the $|\Psi^-\rangle$ Bell-states. Photons 0 and 3 were sent to Alice and Bob, respectively. Alice's photon was delayed by a 100 m fibre such that Bob's photon passed already the 50 m fibre to the transmitter and was on its way to Bob, well ahead of any information about Alice's measurement outcome. Photons 1 and 2 were subjected to a BSM projecting them onto a maximally entangled Bell-state, which ultimately entangled photons 0 and 3 of Alice and Bob, respectively. Preparation of the initially entangled pairs 0-1 and 2-3 in the $|\Psi^-\rangle$ state lead to a symmetrical relation of the entanglement-swapping procedure. Whatever Bell-state photons 1 and 2 were projected on by the BSM, photons 0 and 3 were in the exact
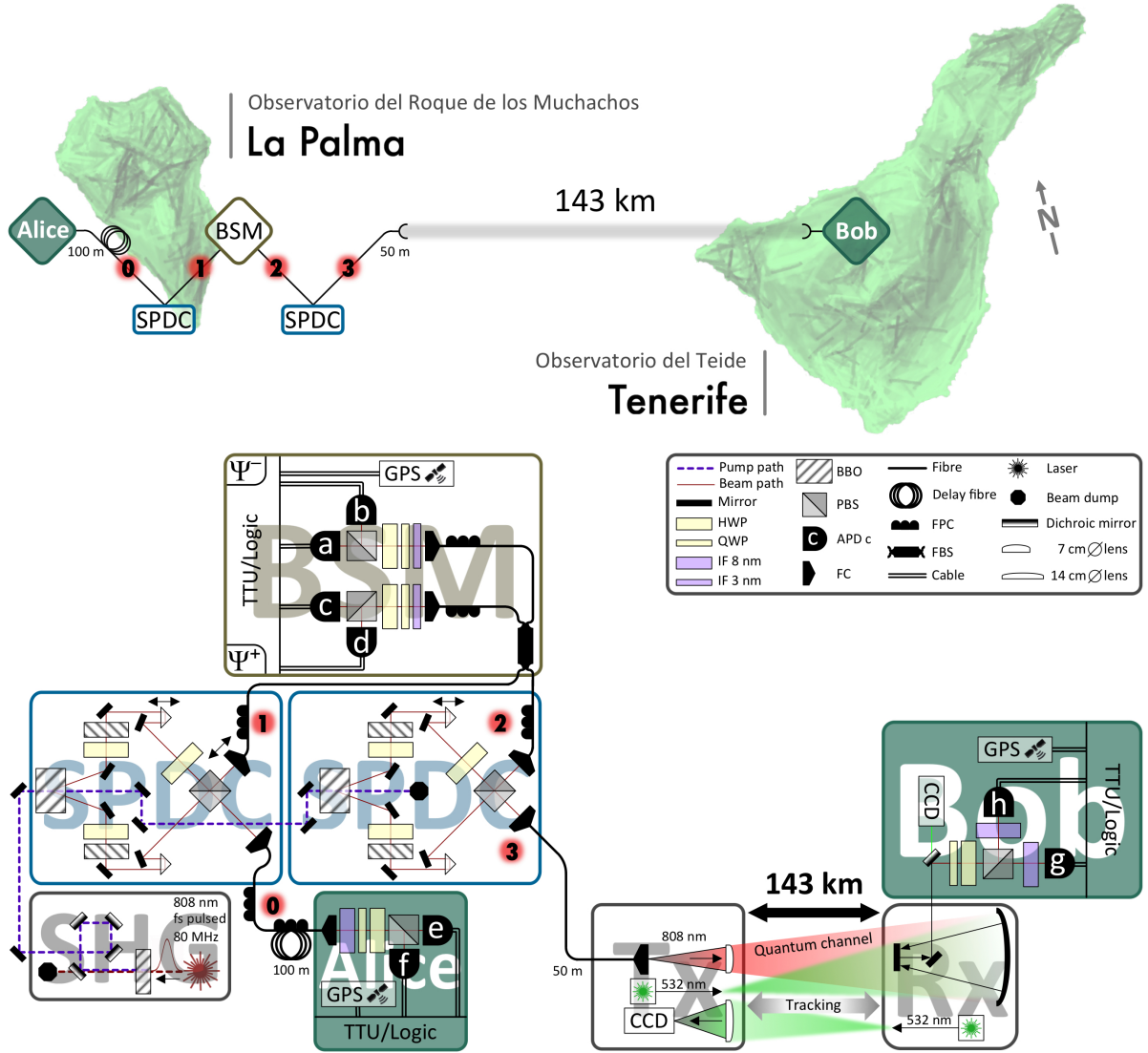
Figure 4.17.: Scheme (top) and experimental setup (bottom) of the 143 km free-space entanglement-swapping experiment between the Jacobus Kapteyn Telescope on La Palma and the Optical Ground Station on Tenerife. Two spontaneous parametric down-conversion (SPDC) sources generated the entangled photon pairs 0-1 and 2-3. Photons 0 and 3 were sent to Alice and Bob, respectively. A Bell-state measurement (BSM) on photons 1 and 2 projected them onto a maximally entangled Bell-state, ultimately entangling photons 0 and 3. Photons 0, 1, 2 and 3 are represented by red numbered circles.

Abbreviations: Second-harmonic generation (SHG), transmitter (Tx), receiver (Rx), global position system (GPS), time-tag unit (TTU), charge-coupled device (CCD), half-wave plate (HWP), quarter-wave plate (QWP), interference filter (IF), β-barium borate (BBO), polarizing beam splitter (PBS), avalanche photodiode (APD), fibre coupler (FC), fibre polarization controller (FPC), fibre beam splitter (FBS).

same Bell-state. With the BSM setup used, we were able to distinguish two out of the four Bell-states, namely the $|\Psi^-\rangle_{12}$ and $|\Psi^+\rangle_{12}$ states. Consequently we were able to verify the entanglement-swapping protocol for half of the swapping events by identifying photons 0 and 3 in the states $|\Psi^-\rangle_{03}$ and $|\Psi^+\rangle_{03}$, respectively.

Setup

In the BSM module the photons interfered on a fibre beam splitter (FBS) with subsequent polarization analysis in each output port of the FBS. FPCs in all input and output ports were used for compensation of any stress induced polarization rotation in the SM fibres. The polarization analyzers were similar to Alice's setup, with the only difference that the FWHM of the IF was 3 nm at 808 nm wavelength due to the narrow-band photons used for the BSM (figure 4.18). Again, photon detection was achieved by a single-photon counting module array *SPCM-AQ4C* from *PerkinElmer*[7]. A logic unit combined the detection signals of the BSM with the outcomes of Alice, providing four possible combinations of the BSM detectors a, b, c, d and Alice's detectors e and f:

$$[(\text{a \& d}) \text{ OR } (\text{b \& c})] \text{ \& e} \rightarrow \left|\Psi^-\right\rangle_{12} |T\rangle_0$$
$$[(\text{a \& d}) \text{ OR } (\text{b \& c})] \text{ \& f} \rightarrow \left|\Psi^-\right\rangle_{12} |R\rangle_0$$
$$[(\text{a \& b}) \text{ OR } (\text{c \& d})] \text{ \& e} \rightarrow \left|\Psi^+\right\rangle_{12} |T\rangle_0$$
$$[(\text{a \& b}) \text{ OR } (\text{c \& d})] \text{ \& f} \rightarrow \left|\Psi^+\right\rangle_{12} |R\rangle_0 \, , \tag{4.1}$$
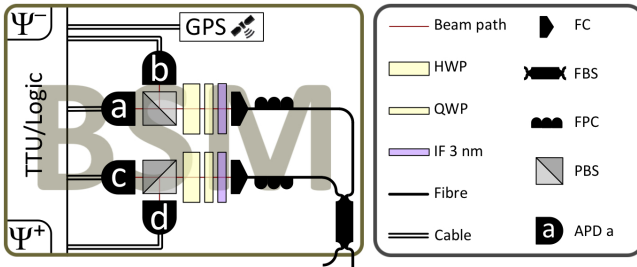
Figure 4.18.: Scheme of the BSM module. Two photons interfered on a 50/50 fibre beam splitter (FBS) with subsequent polarization analysis in each output port. Clicks in detectors a, b, c, and d were logically combined with Alice's detection events and tagged with a time-stamp by the time-tag unit (TTU). Synchronization with Bob's measurement was achieved by the 1 pulse per second signal of the global positioning system (GPS).
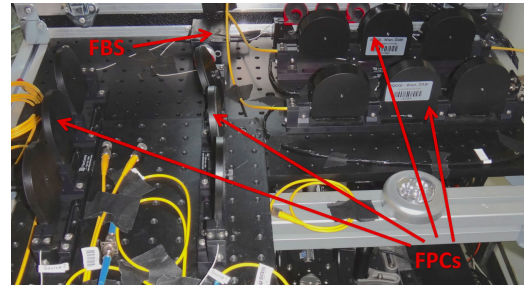
Figure 4.19.: Experimental setup of the tunable fibre beam splitter (FBS) and the fibre polarization controllers (FPCs) in each port. The FBS was adjusted to exactly 50/50 splitting ratio and the FPCs were used for compensation of stress-induced polarization rotation in the single-mode fibres.

with $|T\rangle_0$ and $|R\rangle_0$ denoting the transmission and reflection of photon 0 at the PBS of Alice's polarization analyzer, respectively. The occurrence of any such coincidence detection triggered a logical signal which was fed into a TTU, providing a time-stamp for each event. All data was stored on a hard drive for subsequent comparison with Bob's measurement results. Synchronization with Bob's detection events was ensured by the GPS disciplined 10 MHz signal for the TTU.

Figure 4.19 shows the experimental setup of the FBS and the FPCs. An FPC uses stress-induced birefringence in the SM fibre for polarization alteration. It consists of three adjustable spools around which the SM fibre is wrapped once, twice and once, thus acting similarly to a QWP, HWP and QWP, respectively. We used the models *FPC-2* for 900 μm diameter SM fibres and *FPC-3* for 3 mm diameter SM fibres, both from *FiberControl*[8]. The FBS was a variable ratio coupler *F-CPL-830-N-FP* from *Newport*[5] with the ability to tune the splitting ratio. Therefore we were able to adjust the splitting ratio to exactly 50/50, even though the operating wavelength was specified with 830 nm.

4.3.2. Four-photon GHZ-state experiment

In the four-photon GHZ-state experiment between La Palma and Tenerife the FBS of the entanglement-swapping setup on La Palma was replaced by a free-space PBS. Furthermore, the polarization analyzers of the BSM module now represented the two additional parties usually called Charlie and Dave. The rest of the experimental setup was left unchanged.

Scheme

Similar to the entanglement-swapping experiment two SPDC sources generated entangled photon pairs 0-1 and 2-3 in the $|\Psi^-\rangle$ Bell-states and photons 0 and 3 were distributed to Alice and Bob, respectively. However, in the GHZ-experiment photons 1 and 2 overlapped on a PBS with Charlie and Dave at the output ports. Whenever all participants, i.e. Alice, Bob, Charlie and Dave detected a single photon from the same pump pulse, a four-photon GHZ-state of the form

$$\left|\Psi^{GHZ}\right\rangle_{0123} = \frac{1}{\sqrt{2}}(|H\rangle_0 |V\rangle_1 |V\rangle_2 |H\rangle_3 + |V\rangle_0 |H\rangle_1 |H\rangle_2 |V\rangle_3) \tag{4.2}$$

has been observed. Figure 4.20 shows the experimental scheme and the detailed setup of the 143 km GHZ-experiment.

---

[8]FiberControl, P.O. Box 198, Holmdel, NJ 07733, U.S.A; www.fibercontrol.com
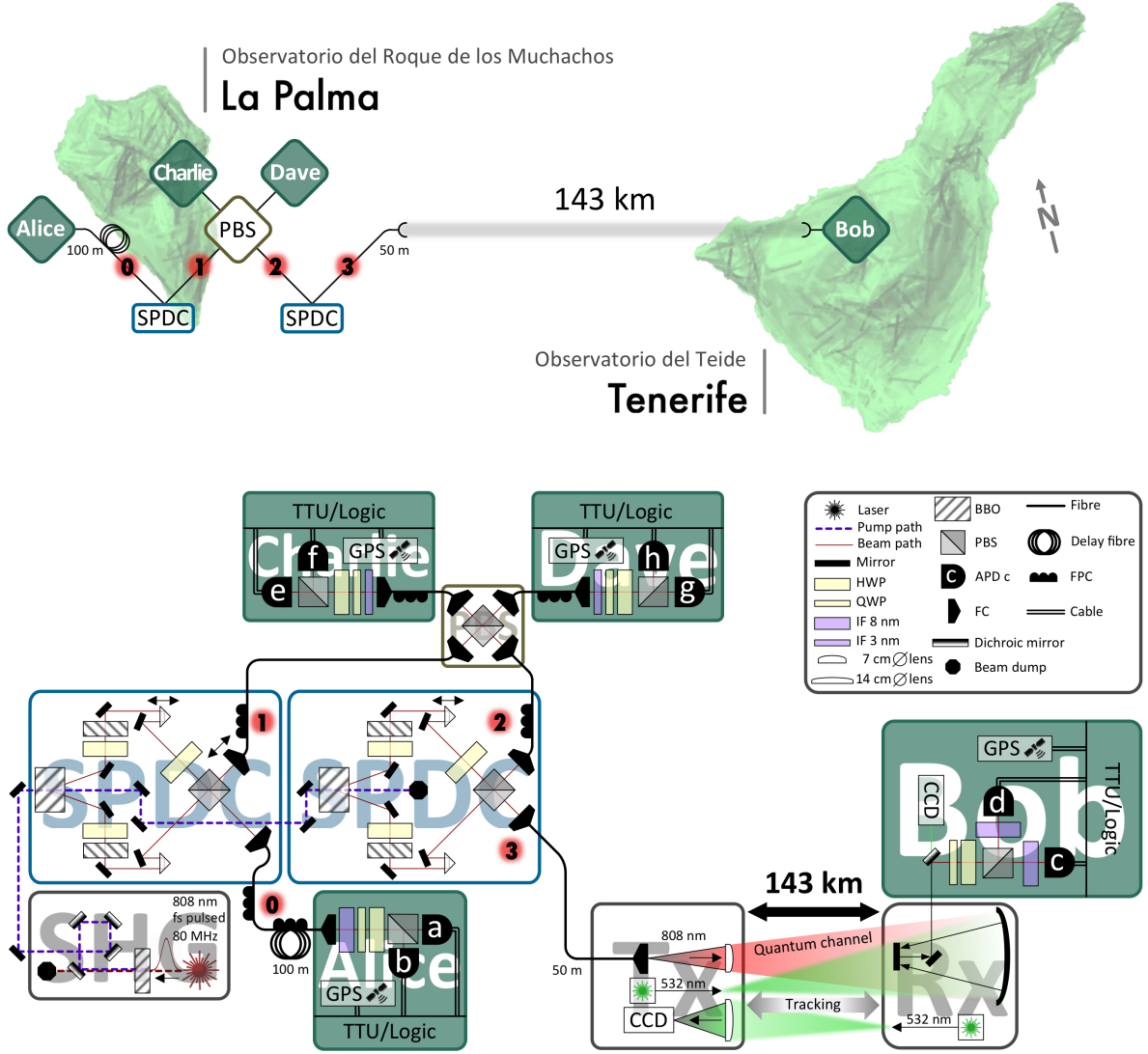
Figure 4.20.: Scheme (top) and experimental setup (bottom) of the 143 km free-space four-photon GHZ-state experiment between the Jacobus Kapteyn Telescope on La Palma and the Optical Ground Station on Tenerife. Two spontaneous parametric down-conversion (SPDC) sources generated the entangled photon pairs 0-1 and 2-3 in the $|\Psi^-\rangle$ Bell-states. Photons 0 and 3 were sent to Alice and Bob, respectively. Photons 1 and 2 interfered on a polarizing beam splitter (PBS), which lead to the GHZ-state $\left|\Psi^{GHZ}\right\rangle_{0123} = \frac{1}{\sqrt{2}}(|H\rangle_0 |V\rangle_1 |V\rangle_2 |H\rangle_3 + |V\rangle_0 |H\rangle_1 |H\rangle_2 |V\rangle_3)$ in the case that Alice, Bob, Charlie and Dave received a single photon each. Photons 0, 1, 2 and 3 are represented by red numbered circles.
Abbreviations: Second-harmonic generation (SHG), transmitter (Tx), receiver (Rx), global position system (GPS), time-tag unit (TTU), charge-coupled device (CCD), half-wave plate (HWP), quarter-wave plate (QWP), interference filter (IF), β-barium borate (BBO), avalanche photodiode (APD), fibre coupler (FC), fibre polarization controller (FPC).

Setup

Photons 1 and 2 were coupled out of fibre and interfered on the free-space PBS. At each output port of the PBS the photons were recoupled into SM fibre and guided to Charlie's and Dave's polarization analyzers (figure 4.21). FPCs for all SM fibres were used for polarization alignment. Experimentally, the polarization analyzers were the exact same as in the BSM-module, now being labelled Charlie and Dave. The clicks of Alice's APDs a and b, Charlie's APDs e and f and Dave's APDs g and h were combined in a logic unit providing the three relevant cases for measurement in the H/V-basis:

$$a \ \& \ f \ \& \ h \to |HVV\rangle_{012}$$
$$b \ \& \ e \ \& \ g \to |VHH\rangle_{012}$$
$$(a \ \& \ e \ \& \ g) \ \text{OR} \ (a \ \& \ e \ \& \ h) \ \text{OR} \ (a \ \& \ f \ \& \ g)$$
$$\text{OR} \ (b \ \& \ e \ \& \ h) \ \text{OR} \ (b \ \& \ f \ \& \ g) \ \text{OR} \ (b \ \& \ f \ \& \ h) \to \ \text{remaining six permutations}$$

$$(4.3)$$
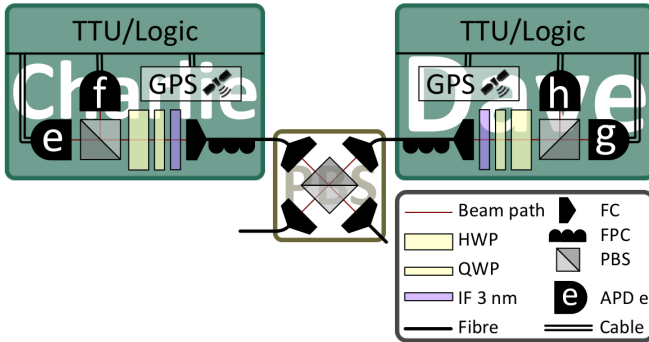
Figure 4.21.: Scheme of the free-space polarizing beam splitter (PBS) setup with Charlie and Dave. Two photons overlap on the PBS with subsequent polarization analysis in each output port. The signals of Charlie's detectors e, f and Dave's detectors g, h were logically combined with Alice's outcomes and time-tagged with a time-tag unit (TTU). A GPS disciplined 10 MHz clock guaranteed synchronization with Bob's detection events.
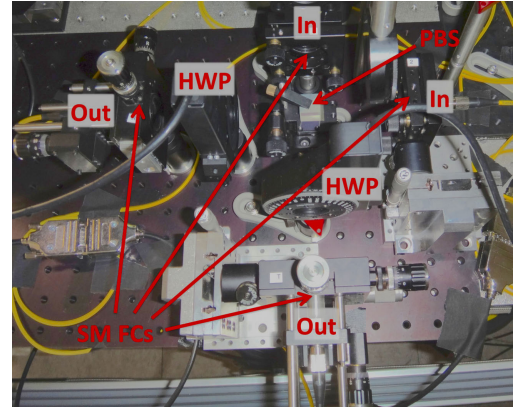
Figure 4.22.: Experimental implementation of the free-space polarizing beam splitter (PBS). The photons were coupled out of single-mode (SM) fibres by fibre couplers (FCs). Half-wave plates (HWP) were used for polarization alignment of the SM fibres. After the PBS the photons were recoupled into SM fibres by fixed-focus FCs.

64

and two relevant cases for measurement in the P/M and R/L-basis:

$$(\text{a \& e \& g) OR (a \& f \& h) OR (b \& e \& h) OR (b \& f \& g)}$$
$$\rightarrow |PPP\rangle_{012} + |PMM\rangle_{012} + |MPM\rangle_{012} + |MMP\rangle_{012}$$
$$\rightarrow |RRR\rangle_{012} + |RLL\rangle_{012} + |LRL\rangle_{012} + |LLR\rangle_{012}$$
$$(\text{b \& e \& g) OR (b \& f \& h) OR (a \& e \& h) OR (a \& f \& g)}$$
$$\rightarrow |MPP\rangle_{012} + |MMM\rangle_{012} + |PPM\rangle_{012} + |PMP\rangle_{012}$$
$$\rightarrow |LRR\rangle_{012} + |LLL\rangle_{012} + |RRL\rangle_{012} + |RLR\rangle_{012}. \qquad (4.4)$$

All coincidences of such kind were time-tagged with a TTU, clocked by a GPS disciplined 10 MHz signal. The measurement data was stored on a hard drive for later comparison with Bob's outcomes, in order to verify the GHZ-states.

The experimental implementation of the free-space PBS is illustrated in figure 4.22. Photons 1 and 2 were coupled out of SM fibres by FCs followed by a HWP in each port of the PBS. The HWPs were needed for alignment purposes of the SM fibres only and were mounted in motorized rotation stages. A tip/tilt stage was used for adjustment of the PBS. After the PBS the photons were recoupled into SM fibres by fixed-focus collimators and guided to Charlie and Dave.

5. Data acquisition and analysis

Several self-made *LabView*[3] programs running on a Windows PC were used for recording and time tagging of all detection events of the APDs at the JKT and the OGS. In order to find coincidences between the remote measurement stations, Alice's and Bob's measurement data was stored on hard drives for later analysis by performing cross-correlation operations.

5.1. Data acquisition

A single-photon detection in an APD triggered a transistor-transistor logic (TTL) pulse, with the logic levels "0" and "1" corresponding to 0V and $\sim 3.3 - 5$V, respectively. The electronic signals of the detectors were fed into a self-designed logic via *Bayonet Neill-Concelman* (BNC) connector cables.

5.1.1. Logic

Each logic fitted in a 19" nuclear instrumentation module (NIM) crate, had 12 input channels, 4 output channels and was based on a field programmable gate array (FPGA) (figure 5.1). A USB connection to the PC allowed for adjustment of parameters such as logical combinations and relative delays between the individual channels or the measurement time. Additionally, the observed count rates were transferred to the PC via the USB link. A *LabView*[3] program was used as interface between the observer and the device (figure 5.2). In the *Singles* column the counts of each detector within the measurement time is shown. Each column of the *Singles-Logic-Pattern* defines the logical AND combination of the orange highlighted channels. The resulting coincidences are illustrated in the *Coincidences* column, where each row corresponds to a column of the *Singles-Logic-Pattern*. Columns $\Sigma 1$-$\Sigma 4$ give the sum over the orange highlighted coincidences in the respective text field below.

The program also allowed for rerouting of the measurement data to the 4 output

Figure 5.1.: The self-designed logic and the detector arrays at La Palma. BNC cables fed the detector signals into the logic from which the logically-combined data was rerouted to a time-tag unit (TTU) via its 4 output channels. All devices fitted in a 19" nuclear instrumentation module (NIM) crate.

channels of the logic for further processing. Such, the logically-combined signals for the entanglement-swapping experiment (equation 4.1) and GHZ experiment (equations 4.3 and 4.4) were forwarded to the outputs of the logic and fed into the TTU, respectively.

5.1.2. Multi-pair reduction

Strong pumping of the BBO crystals resulted in very high pair-generation rates, which also increased the probability of the emission of more than one pair per pump pulse. These multi-pair emissions reduced the quality of entanglement and therefore resulted in extended measurement times or even rendered an experiment impossible.

In order to reduce the effect of multi-pair emissions we discarded all coincidence events where more than 4 detectors clicked. This was implemented via the *LabView*[3] program of the logic by selecting all detectors of the *Singles-Logic-Pattern* and adjusting the so-called *Pattern Polarity* parameters in the software. In figure 5.2 the first 8 columns of the *Singles-Logic-Pattern* resulted in a coincidence count whenever the highlighted detectors clicked within the coincidence window, without taking into account the other detectors. Columns 9 till 16, however, where programmed to reproduce the same combinations once more, but this time considering multi-pair events by discarding coincidence events with more than 4 simultaneous clicks. The ratios $\Sigma1/\Sigma2$ and $\Sigma3/\Sigma4$ gave the signal-to-noise ratios (SNRs) with and without multi-pair reduction, respectively. Of course this scheme couldn't detect multi-pair emissions which still resulted in 4-fold coincidences and therefore it only gave a slight improvement of the entanglement quality.
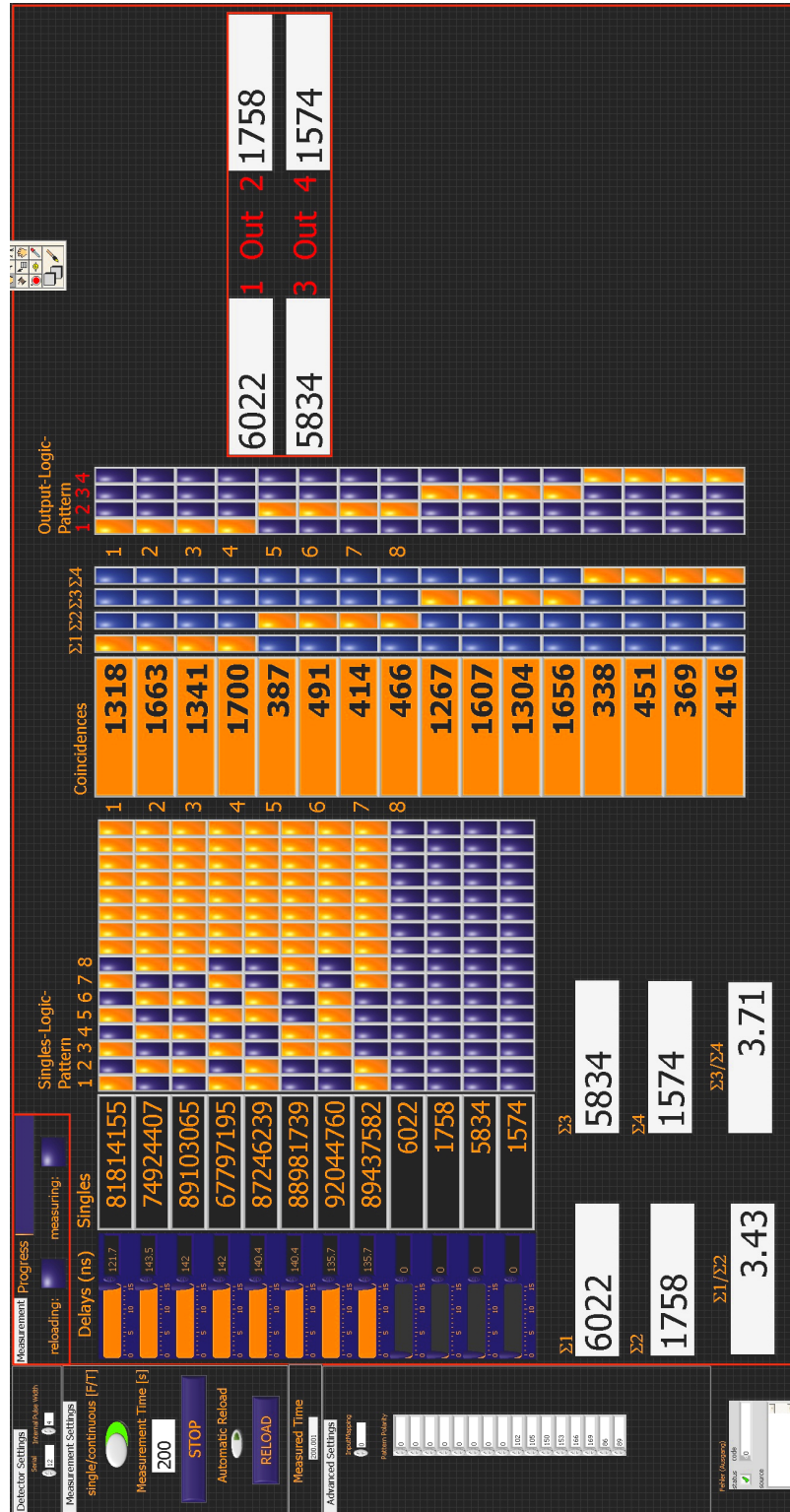
Figure 5.2.: The *LabView*[3] program for the logic. It was used to transfer parameters and measurement data between the device and the PC.

5.1.3. Time tagging

The logically combined signals were routed from the logic outputs to the TTU inputs via BNC cables. Each TTU featured a 10 MHz clock input, input channel 1 for the 1 PPS GPS signal for time reference and input channels 2-6 for the measurement data (figure 5.3). The TTU labelled every registered pulse with a 64-Bit tag consisting of channel information and a time tag with 156 ps temporal resolution. A *Trimble*[9] *Thunderbolt* GPS disciplined clock was used to provide a stable 10 MHz clock and the 1 PPS signal for the TTU. In order to transfer the data from the TTU to the PC we connected the device via a 68-Pin connector to a *National Instruments*[3] *PCI-DIO-32HS* [93] card for high-speed digital data transfer. All devices were designed to fit in a 19" NIM crate.

A self designed *LabView*[3] program controlled data acquisition on both islands and transferred the measurement files from Tenerife to La Palma via the internet. Finally a C[++] program (details and source code see reference [94]) was used to perform a cross correlation between the two files and find the coincidence peaks.

---

[9]Trimble Germany GmbH, Am Prime Parc 11, 65479 Raunheim, Germany; www.trimble.com
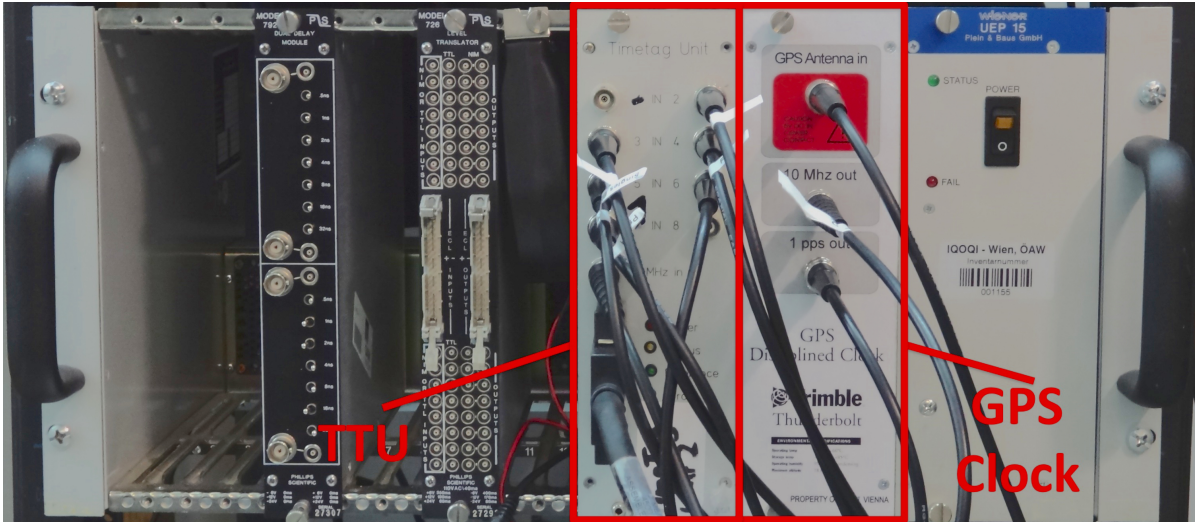
Figure 5.3.: The self-designed time-tag unit (TTU) and the *Trimble*[9] *Thunderbolt* GPS disciplined clock. A GPS antenna was connected to the device, which provided the 10 MHz clock and 1 pulse per second (PPS) signal for the TTU. The 1 PPS signal was connected to channel 1 of the TTU and channels 2-6 were used for data recording. All devices fitted in a 19" nuclear instrumentation module (NIM) crate.

Entanglement assisted clock synchronization

Even though the 1 PPS GPS signal was generated by an atomic clock at a GPS satellite, we observed a long-term residual time drift in the order of $\approx \pm 15$ ns. This effect was mainly caused by atmospheric inhomogeneities in the ionosphere [95] which influenced the speed and ultimately the arrival time of the GPS signal. For satellites with low elevation this effect becomes stronger, as the signal has a longer passage through the atmosphere (figure 5.4).

The relative drift between the clocks at La Palma and Tenerife would broaden the coincidence peak, leading to an increased coincidence window and therefore an increased noise contribution. Furthermore, if the coincidence window would become larger than the repetition period of the pump laser, i.e. 12.5 ns, one would also detect coincidences between uncorrelated photons from neighbouring pump pulses. We circumvented the problem by performing a so-called entanglement assisted clock synchronization. First we divided the total measurement time into successive measurement runs of only 30 s duration in order to minimize the influence of the relative time drift. Second we additionally time tagged the signal of a single APD of the BSM or Dave in the case of the entanglement-swapping or GHZ experiment, respectively. The much higher 2-fold count rate allowed for a 2-fold coincidence search between detection events at La Palma and Tenerife in each 30 s file. This relative timing information was used to temporally shift each measurement file with respect to each other and finally compensate for the long-term clock drift. Applying this method enabled us to limit the coincidence window down to only 5 ns.
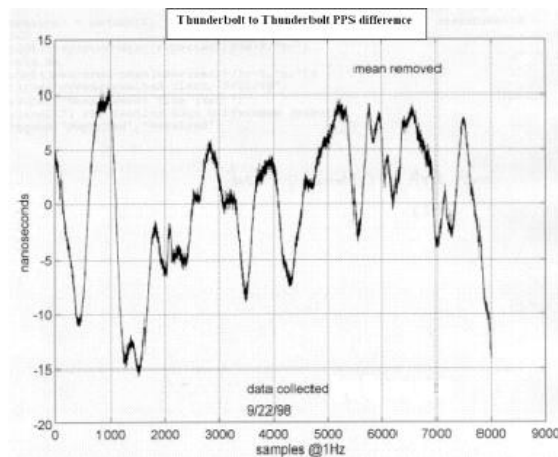
Figure 5.4.: The long-term relative clock drift of $\approx \pm 15$ ns between two *Trimble*[9] *Thunderbolt* GPS disciplined clocks during 8000 s [94].

5.2. Analysis

The C++ program for the calculation of the cross correlation between the data from La Palma and Tenerife generated a comma-separated values (CSV) file from the binary time-tag files. The first column of the CSV file represented the fine offset (after introducing a coarse offset of 477.425 μs for the time of flight from La Palma to Tenerife) between the input files over a range of ± 1000 bins with a bin size of 1 ns. The next 5 columns contained the coincidences of input channel 1 of the first input file with the 5 input channels of the second input file, respectively. This was repeated with input channels 2 to 5 of the first input file until all 25 combinations have been compiled. The last column gave the sum over all combinations. Each row corresponded to the relative offset given in the first column.

Finally all CSV files were combined, synchronized and analyzed by a self designed *LabView*[3] program in order to retrieve the 4-fold correlations between the measurement data of La Palma and Tenerife.
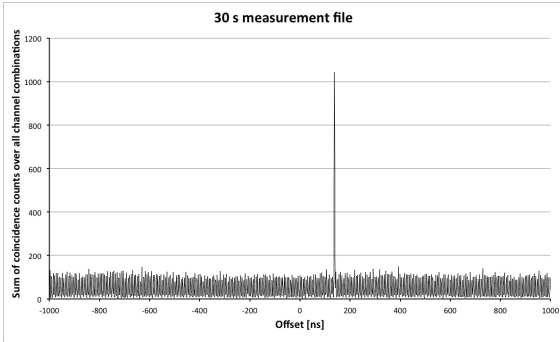
Figure 5.5.: A typical 30 s measurement file illustrating the sum over all coincidence combinations. The main contribution comes from the 2-fold coincidences for the entanglement assisted clock synchronization. A clear peak was observed at the coarse offset of 477.425 μs minus the fine offset of 137 ns between the measurement data of La Palma and Tenerife.
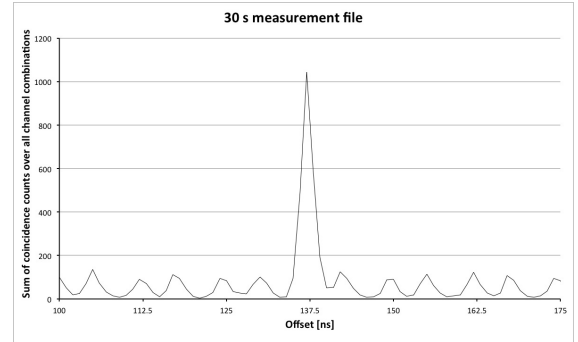
Figure 5.6.: The same 30 s measurement file as in figure 5.5 zoomed in on the coincidence peak. One can identify the 12.5 ns repetition period of the pump laser.

6. Results

The data was recorded during the nights from 3 May until 11 May 2013, chosen around new moon at 10 May, 01:28:38 (UTC+2) for reduced stray light. Before the actual long-distance experiments, we specified the performance of the sources and the total setup on La Palma. Therefore we introduced a local Bob module, identical to Alice's measurement apparatus. We locally measured the HOM-dip visibilities at the BSM for several average pump powers, depending on the path difference Δl between photons 1 and 2. Such we were able to identify the optimal tradeoff between count rate and entanglement quality for the experiments over 143 km. The results are illustrated in figure 6.1. The average
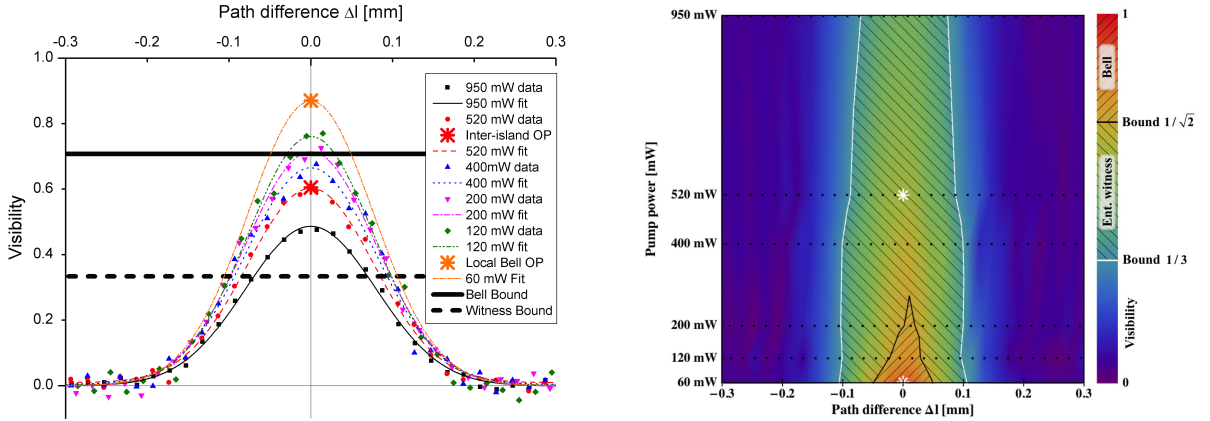
Figure 6.1.: Left: The Hong-Ou-Mandel dip visibilities between photons 1 and 2 at the Bell-state measurement depending on the path difference Δl in mm. The measurement data was taken at several average pump powers in mW, set such that both sources experienced an identical pump power. A Gaussian fit was applied to approximate the measurement data. The operation point (OP) for the local Bell test and the inter-island experiments is illustrated by an orange and red asterisk, respectively. The bound of $1/\sqrt{2}$ for the violation of a Clauser-Horne-Shimony-Holt (CHSH)-type Bell inequality and of $1/3$ to confirm entanglement via an entanglement witness is illustrated by a solid and dashed black line, respectively.
Right: Density plot of the data on the left, giving an overview of the areas where entanglement can be confirmed by a witness or even the violation of a CHSH-type Bell inequality. The black dots represent the measurement data from the left graphs and the visibility is encoded in rainbow colours. The OPs are marked by white asterisks.

pump power is given in mW and was adjusted by the attenuation of the pump laser. The left plot of figure 6.1 shows the data points and Gaussian fits for 60, 120, 200, 400, 520 and 950 mW average pump power at each source. The FWHM of ≈ 0.2 mm of the illustrated graphs is in line with the coherence length governed by the spectral filtering with the IFs used ($\Delta\lambda = 3$ nm FWHM at $\lambda_0 = 808$ nm). One can see that the visibility at zero delay $\Delta l = 0$ mm drops below the bound of $1/\sqrt{2}$ for the violation of local realistic theories at about 200 mW, but even at full pump power, i.e. 950 mW, a visibility of 0.49 still above the bound of 1/3 to confirm entanglement via an entanglement witness was achieved. With a local 4-fold coincidence rate of only 1 count per second (cps) at lowest pump power (60 mW) and 370 cps 4-folds at full power (950 mW) we chose an operation point (OP) at 520 mW corresponding to 100 cps 4-folds for the inter-island experiments. On one hand the visibility at this OP was 0.6 and therefore well above the entanglement-witness bound, ensuring enough headroom in case of additional errors over the 143 km free-space link. On the other hand the 4-fold count rate at this OP allowed for reasonable measurement times over the long-distance link. The density plot on the right of figure 6.1 gives an overview of the areas where entanglement between photons 0 and 3 can be confirmed via an entanglement witness or even by the violation of a CHSH-type Bell inequality.

Due to the low 4-fold rate of less than 1 cps at 60 mW pump power and the expected ~ 30 dB channel loss over the free-space link, it would not have been possible to collect enough data within the given observation time in order to violate a CHSH-type Bell inequality over the long distance quantum channel with enough statistical significance. Therefore we chose this OP for a Bell test with all measurement parties on La Palma, using the local Bob module. In 8000 s we locally detected 5647 singlet and 5618 triplet 4-fold events for photons 0 and 3, achieving an S-value (equation 2.9) of 2.487 ± 0.287 and 2.469 ± 0.287, respectively. We locally violated a CHSH-type Bell inequality on La Palma by more than 1.6 σ. Assuming a perfectly stable setup, we would have had to measure ~ 10 times longer, i.e. ~ 22 h in order to reach a statistical significance of more than 3 σ. This result clarifies the reason why we had to confirm the entanglement over the 143 km free-space link via an entanglement witness, offering a much lower visibility bound as well as an OP with a 100 times higher 4-fold rate.

6.1. Entanglement-swapping experiment results

In the long-distance entanglement-swapping experiment we cumulated 542 measurements á 30 s, giving a total of 271 min of measurement data in 3 out of 4 consecutive nights from 3 May until 7 May 2013. In the night from 4 to 5 May we have no useful data due to bad weather conditions. The top, center and bottom graphs in figure 6.2 illustrate the temporal evolution of the entanglement-swapping visibilities in the three mutually unbiased bases and the respective errors assuming Poissonian photon statistics. The abscissa represents the cumulated measurement time in min. A closer look at the first couple of minutes of the singlet-state visibility in the P/M-basis shows that there are no values given. This is because of the fact that no "undesired" 4-fold count has occurred until then, making it useless to give a statistical statement at that point in time. The first 17 and 19 minutes of data for the visibilities in the H/V and P/M-bases were taken in our first measurement night, which appeared to exhibit very good atmospheric conditions. This resulted in a high count rate which consequently lead to a rapid decrease of the statistical deviation within the first minutes of cumulated data. One can see, that the error bars in the top and center graphs of figure 6.2 decrease more rapidly than in the bottom graphs illustrating the visibilities in the R/L-basis. The measurement data for the R/L-basis was recorded under moderate atmospheric conditions with lower count rates during the whole measurement time. Therefore the fluctuations of the visibilities in the bottom graphs start to smooth out much later, after ~ 90 min. This can be explained by the low average 4-fold count rate of ~ 1 count per measurement file in the R/L-basis. As long as the relative change in "desired" or "undesired" counts from file to file is in the order of the total "desired" or "undesired" counts, their ratio and therefore the visibility fluctuates much stronger. Due to the reduced count rate it also took more than double the measurement time to yield a comparable amount of swapping events in the R/L-basis.

In total we detected 506 singlet states $|\Psi^-\rangle_{03}$ and 492 triplet states $|\Psi^+\rangle_{03}$ between photons 0 and 3. The measurements in the H/V-basis yielded 300 swapping events in 57 min, in the P/M-basis 335 swapping events in 63.5 min and in the R/L-basis 363 swapping events in 150.5 min. Table 6.1 and figure 6.3 give the visibilities in the three mutually unbiased bases $V_{H/V}$, $V_{P/M}$ and $V_{R/L}$, the mean visibility $\overline{V} = 1/3 \cdot (V_{H/V} + V_{P/M} + V_{R/L})$, the entanglement-witness value $W = 1/2 - 1/4 \cdot (1 + V_{H/V} + V_{P/M} + V_{R/L})$ and the locally measured S-value. We showed that the entanglement was swapped onto photons 0 and 3 over a distance of 143 km even though these photons shared no common

Figure 6.2.: The evolution of the entanglement-swapping visibilities in the three mutually unbiased bases and the respective errors (assuming Poissonian photon statistics) in minutes of cumulated measurement time.

Top: The result in the H/V-basis. The first 17 min were recorded in the night from 3 to 4 May 2013 and the remaining data in the night from 5 to 6 May 2013.

Center: The result in the P/M-basis. The first 19 min were recorded in the night from 3 to 4 May 2013 and the remaining data in the night from 5 to 6 May 2013.

Bottom: The result in the R/L-basis. The first 75.5 min were recorded in the night from 5 to 6 May 2013 and the remaining data in the night from 6 to 7 May 2013.

Swapped state	$\lvert\Psi^-\rangle_{03}$	$\lvert\Psi^+\rangle_{03}$
$V_{H/V}$	0.618 ± 0.067	0.610 ± 0.062
$V_{P/M}$	0.607 ± 0.060	0.556 ± 0.065
$V_{R/L}$	0.624 ± 0.056	0.542 ± 0.065
$\overline{V} = 1/3\,(V_{H/V} + V_{P/M} + V_{R/L})$	0.616 ± 0.035	0.569 ± 0.037
$W = 1/2 - 1/4\,(1 + 3\overline{V})$	-0.212 ± 0.027	-0.177 ± 0.028
Local S-value	2.487 ± 0.287	2.469 ± 0.287

Table 6.1.: The table of results of the entanglement-swapping experiment over 143 km. It gives the visibilities $V_{H/V}$, $V_{P/M}$ and $V_{R/L}$ in the three mutually unbiased bases, the mean visibility $\overline{V}$, the entanglement witness W and the locally measured S-value. The errors were calculated assuming Poissonian statistics.

Figure 6.3.: Graphical illustration of the values given in table 6.1 including the relative classical bounds (black solid lines) and range (grey bars).

past. The measured entanglement witness was 7.99 and 6.37 standard deviations beyond the classical bound of 0 for the $\lvert\Psi^-\rangle_{03}$ and $\lvert\Psi^+\rangle_{03}$ state, respectively. In our experiment Alice and Bob were space-like separated, such that in a reference frame moving at a speed of $\approx 0.99975 \cdot c$ relative to the source, one would observe a simultaneous photon detection of Alice and Bob and a Lorentz-contracted distance of ≈ 3.2 km between the two.

6.2. Four-photon GHZ-state experiment results

The 4-photon GHZ-state experiment was carried out in two consecutive nights from 9 May until 11 May 2013. We measured the visibilities for the 3 cases where all measurement stations (Alice, Bob, Charlie and Dave) were set to the same measurement basis. In total we ran 332 measurements á 30 s, accumulating a total of 403 four-fold coincidences in 166 min. Measurement runs with all four measurement stations set to the H/V-basis yielded 245 four-folds in 39.5 min. In the P/M-basis we gained 71 four-folds in 64.5 min and 87 four-folds in 62 min in the R/L-basis. Figure 6.4 illustrates the temporal evolution of the visibilities in the H/V, P/M and R/L-basis, as well as the respective errors assuming Poissonian photon statistics. The abscissa represents the
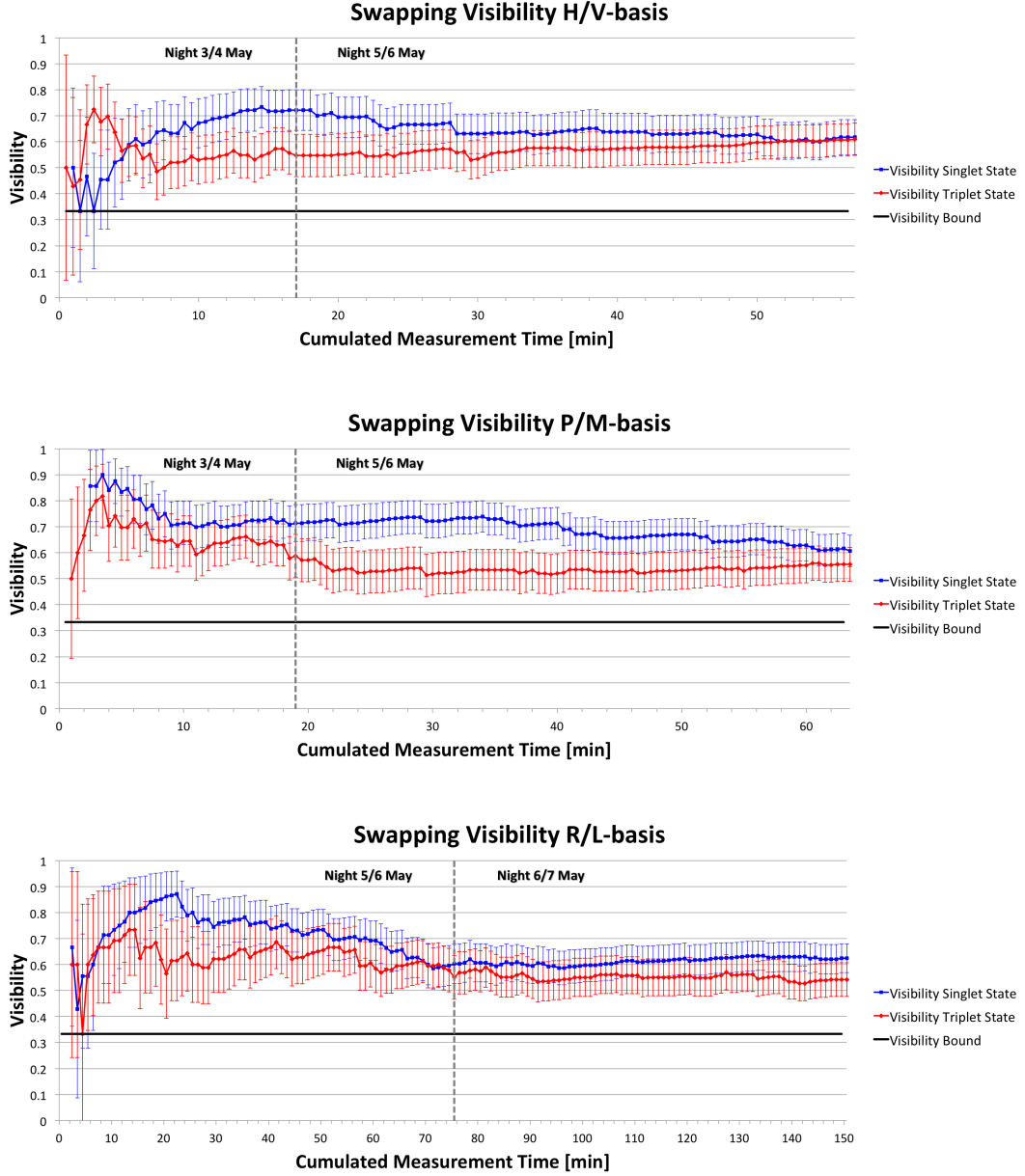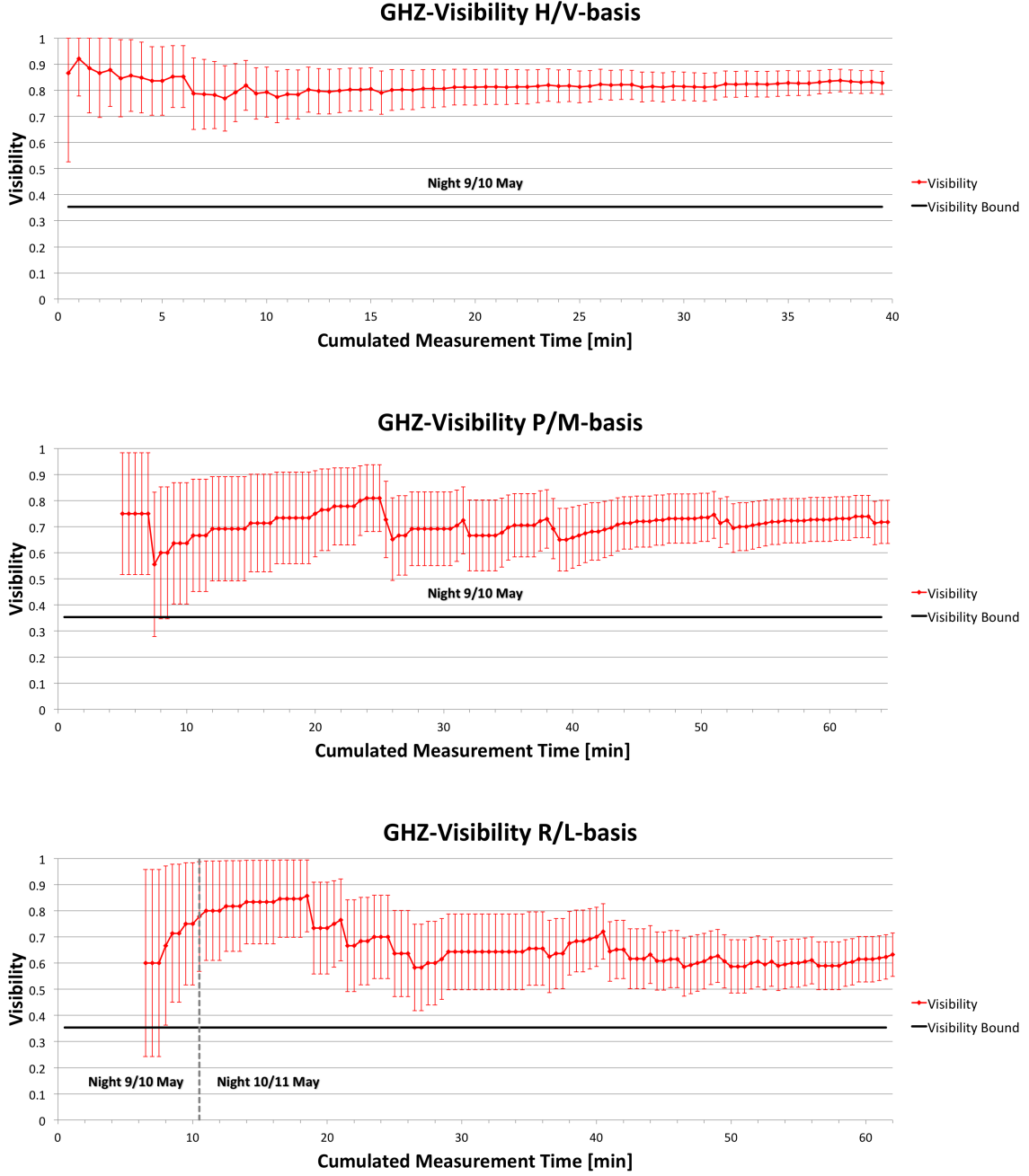
Figure 6.4.: The evolution of the GHZ-state visibilities in the three mutually unbiased bases and the respective errors (assuming Poissonian photon statistics) in minutes of cumulated measurement time. **Top:** The result in the H/V-basis. The data was recorded in the night from 9 to 10 May 2013. **Center:** The result in the P/M-basis. The data was also recorded in the night from 9 to 10 May 2013. **Bottom:** The result in the R/L-basis. The first 10.5 min were recorded in the night from 9 to 10 May 2013 and the remaining data in the night from 10 to 11 May 2013.

cumulated measurement time in min. All visibilities were above the classical bound [49; 50] of $\frac{1}{2\sqrt{2}} \approx 0.354$ for a 4-photon GHZ-state during the whole measurement session.

A close look at figure 6.4 reveals that the standard deviation of the visibility in the H/V-basis (top graph) decreased much faster than in the other bases. This and the reduced fluctuations of the visibility after only ~ 10 min was due to higher count rates compared to the other measurements. On one hand we had better weather conditions at the beginning of the night from 9 to 10 May. On the other hand the contribution of errors caused by multi-pair emissions is lower in the computational basis, therefore we increased the pump power compared to the P/M and R/L-basis by $\sim 50\%$ in order to further reduce the measurement time in the H/V-basis. In contrast, the measurements in the P/M and R/L-basis showed very low mean 4-fold rates of less than 1 count per measurement file. Therefore it lasted several minutes until the first useful statistical statements about the visibilities could be made, as there were no "undesired" counts recorded till then. Also the center and bottom graphs of figure 6.4 show strong fluctuations of the visibilities due to the low count rates and the respective standard deviations decreased only slowly but steady towards a violation of the bound for local realistic theories by more than 3 standard deviations. Table 6.2 and figure 6.5 give the final results for the visibilities in the three mutually unbiased bases $V_{H/V}$, $V_{P/M}$ and $V_{R/L}$ and the mean visibility $\overline{V}$. We successfully showed 4-photon entanglement with

GHZ-state	$\vert\Psi^{\mathbf{GHZ}}\rangle_{\mathbf{0123}}$
$\mathbf{V_{H/V}}$	0.829 ± 0.044
$\mathbf{V_{P/M}}$	0.718 ± 0.083
$\mathbf{V_{R/L}}$	0.632 ± 0.083
$\mathbf{\overline{V} = 1/3\ (V_{H/V} + V_{P/M} + V_{R/L})}$	0.726 ± 0.042

Table 6.2.: The table of results of the 4-photon GHZ-state experiment over 143 km. It gives the visibilities $V_{H/V}$, $V_{P/M}$ and $V_{R/L}$ in the three mutually unbiased bases and the mean visibility $\overline{V}$. The errors were calculated assuming Poissonian statistics.

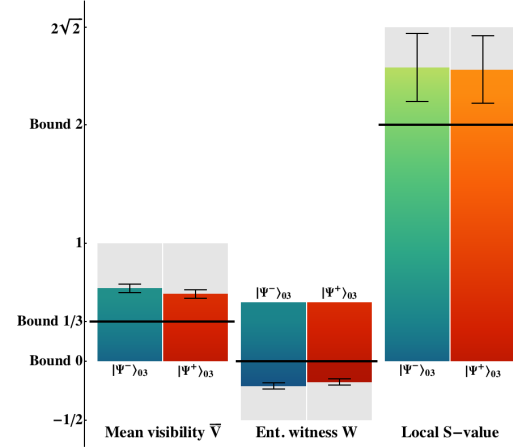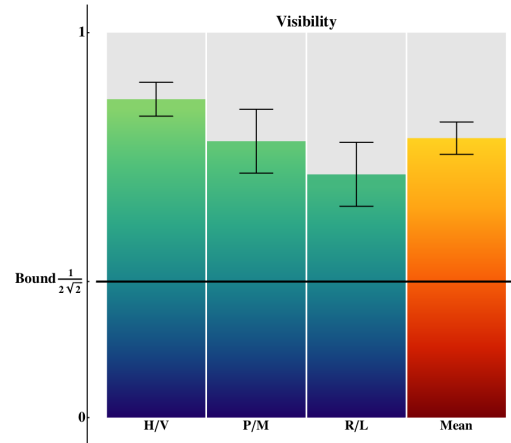**Figure 6.5.:** Graphical illustration of the values given in table 6.2 including the classical bound (black solid line) and range (grey bars) for the different values.

Bob being 143 km separated from Alice, Charlie and Dave. The GHZ-state visibility in the $H/V, P/M$ and R/L-basis was 10.81, 4.39 and 3.35 standard deviations above the limit for local realistic theories, respectively. Consequently, the resulting mean visibility was 8.87 standard deviations above this classical bound. The violation of the Mermin inequality for a 4-photon GHZ-state would have required to perform measurement runs for 8 different settings, which would not have been practical due to our limited observation time at the OGS on Tenerife. Unfortunately, it is not possible to extract data for a long-distance 3-photon GHZ-state experiment out of our measurements in retrospect, due to the special design of our data-collection setup for Alice, Charlie and Dave on La Palma.

7. Conclusion and Outlook

The presented work described the setup and implementation of two long-distance free-space multi-photon experiments as performed at the Canary Islands. Both, the entanglement-swapping experiment as well as the 4-photon GHZ experiment comprised a 143 km long-distance free-space quantum channel from La Palma to Tenerife. We therefore utilized the local infrastructure of the observatories at an altitude of ~ 2400 m on both islands. The Jacobus Kapteyn Telescope building of the Isaac Newton Group of Telescopes on La Palma accommodated the main experimental setup and the transmitter station. The receiver module was implemented in the Optical Ground Station of the European Space Agency on Tenerife, which houses a 1 m diameter reflecting telescope. We successfully confirmed entanglement swapping with an entanglement witness more than 6 standard deviations beyond the classical limit. Therefore we entangled two photons that were generated in two independent down-conversion processes and shared no common past. In our experimental setup the measurement stations were space-like separated, such that no information about the measurement outcome of one photon could possibly influence the outcome of the other. So far the results of the entanglement-swapping experiment have been published on arXiv (see appendix A.2). In our second experiment we successfully entangled two photon pairs to a 4-photon-entanglement GHZ state with one photon being sent to a remote measurement station 143 km separated from the others. We verified the quantum nature of the GHZ-state with a visibility in the H/V, P/M and R/L-basis of 10.81, 4.39 and 3.35 standard deviations beyond the limit for local realistic theories, respectively.

With the successful realization of our multi-photon experiments over a turbulent 143 km horizontal link, we showed the feasibility of space links for future satellite missions. The implemented protocols constitute the fundamental quantum resource for the distribution of entanglement over large distances and between multiple parties. In a device such as the quantum repeater [7; 8] large distances are divided into shorter links by several repeater nodes. Entanglement is distributed between the nodes and ultimately extended over the whole range by the process of entanglement swapping between adja-

cent nodes. In a fully fledged realization one also has to be able to store the quantum states in a memory [4; 96] until all nodes are readily prepared. Furthermore the quality of each entangled pair has to be enhanced by means of entanglement purification [97–99], such that the fidelity of the final state will be well above the required bound. For example applying the purification protocol of Pan et al. [98; 99] on our entanglement-swapping results would increase our measured state fidelity $F = 1/2 - W \approx 0.712$ to a purified state fidelity $F' = \frac{F^2}{F^2+(1-F)^2} \approx 0.859$ even above the threshold of ≈ 0.78 for the violation of a CHSH-type Bell inequality. Nevertheless, a quantum memory and entanglement purification solely serve to increase the efficiency and quality of the protocol, whereas entanglement swapping represents the integral quantum tool for a quantum repeater.

The vision of a world-spanning quantum communication network, with satellites distributing entanglement across the globe, calls for further experiments toward this goal. A possible experiment could consist of two widely separated sources for entangled photon pairs and a Bell-state measurement station located in between. Besides all the practical applications of bringing quantum technology to space, the new operational area would also grant access to a variety of fundamental tests of quantum mechanics, e.g. the question of a limited distance for entanglement. Bearing in mind the above I believe in a bright future of free-space quantum communication in particular and the field of quantum information in general.

A. Appendix

A.1. Specification sheets

Chameleon™ Ultra Family
Widely Tunable, Hands-Free, Modelocked Ti:Sapphire Lasers

	Chameleon Ultra	Chameleon Ultra I	Chameleon Ultra II
Average Power[1] (W)	>2.5	>2.9	>3.5
Tuning Range (nm)	690 to 1020	690 to 1040	680 to 1080
Peak Power[1] (kW)	>200	>250	>300
Power Specifications			>650 mW at 680 nm
	>500 mW at 690 nm	>600 mW at 690 nm	
			>1.6W at 700 nm
	>1.4W at 710 nm	>1.5W at 710 nm	
	>2.5W at 800 nm	>2.9W at 800 nm	>3.5W at 800 nm
	>1.4W at 920 nm	>1.45W at 920 nm	>1.6W at 920 nm
	>450 mW at 1020 nm	>450 mW at 1020 nm	>550 mW at 1020 nm
		>300 mW at 1040 nm	
			>200 mW at 1080 nm
Tuning Speed[2] (nm/s)	>35	>40	>40
Pulse Width[1,3] (fs)		140	
Noise[1,4] (%)		<0.15	
Output Power Stability[5] (%)		<±0.5	
Spatial Mode[1]		TEM$_{00}$ (M^2 <1.1)	
Beam Diameter[1,6] (mm)		1.2 ±0.2	
Beam Ellipticity[1,7]		0.9 to 1.1	
Astigmatism[1]		<10%	
Repetition Rate (MHz)		80	
Polarization		Horizontal >500:1	
Pointing (μrad/nm)		<0.5	
Operating Voltage		90 to 250 VAC (auto ranging)	
Maximum Operating Current		<15A at 90 VAC (power supply)	
		<7A at 90 VAC (chiller)	
		<2A at 90 VAC (MRU X1)	
System Power Consumption		2300W max., 1300W typical	
Line Frequency		47 to 63 Hz	
Operating Temperature Range		15 to 35°C (59 to 95°F)	
Weight of Laser Head		42 kg (93 lbs.)	
Weight of Power Supply		41 kg (90 lbs.)	
Umbilical Length		4 m (13 ft.)	
Chiller:			
Dimensions (L x W x H)		27 x 20 x 38 cm (11 x 8 x 15 in.)	
Weight		11 kg (25 lbs.)	
MRU Air Recirculator:			
Dimensions (L x W x H)		46 x 43 x 8.5 cm (18 x 17 x 3 in.)	
Weight		9 kg (20 lbs.)	

[1] Specified at peak of tuning range.
[2] Average speed measured over entire tuning range.
[3] Based on sech^2 deconvolution of 0.65 times autocorrelation width.
[4] Measured RMS in a 10 Hz to 20 MHz bandwidth.
[5] Power drift in any two-hour period with less than ±1°C temperature change after a one-hour warm-up.
[6] 1/e^2 at exit port.
[7] Ratio of major to minor 1/e^2 beam diameter at exit port.
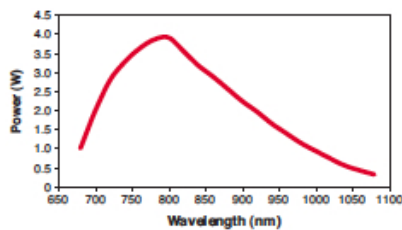
Figure A.1.: Specifications of the *Coherent* pump laser *Chameleon Ultra II* [90].

Table 1. **Specifications SPCM-AQ4C at 22˚C, all models, unless otherwise indicated**

Note: *At power on and 40˚C
**At maximum count rate

Parameter		Minimum	Typical	Maximum	Units
Supply currents:	at +2 V		1.0	4.0*	Amps
				3.0**	Amps
	at +5 V		0.20	1.0**	Amps
	at +30 V		0.01	0.04**	Amps
Maximum power consumption	at +2 V		2	6**	Watts
	at +5 V		1	5**	Watts
	at +30 V		0.3	1.2**	Watts
Supply voltages		1.95	2	2.05	V
		4.75	5	5.25	V
		29	30	31	V
Operating temperature (heatsink)		5		40	˚C
Photon detection efficiency (per channel)	at 400nm	1	2.5		%
	at 650nm	45	60		%
	at 830nm	35	45		%
	at 1060nm	1	2		%
Average Pd variation per channel at constant heat sink temperature (6 hrs at 25°C)			±1	±3	%
Average Pd variation per channel at 5°C to 40°C heat sink temperature			±4	±10	%
Dark count (per channel)				500	Counts/Sec.
Average dark count variation per channel at constant heat sink temperature (6 hours at 25˚C)				±10	%
Average dark count variation per channel at 5˚C to 40˚C heat sink temperature				±20	%
Dead time (Count rates below 5 Mc/s) nanoseconds			50		ns
Output pulse width			25		ns
Maximum count rate (per channel)	Continuous		1.5		Mc/s
	500ms duration, 25% duty cycle		4		Mc/s
Afterpulsing probability			0.3	0.5	%
Gate threshold voltage (at V_{Sup}= 5V)					
	Low level (sink 5mA) = Gate On		0	0.4	V
	High level = Gate Off		3.5	5.25	V
Gate turn-on delay before first edge of true output pulse			60	75	ns
Gate turn-off delay for minimum last output pulse width of 10ns			4	15	ns
Linearity correction factor [7] See fig. 3					
	at 200 kc/s		1.01	1.10	
	at 1 Mc/s		1.08	1.15	
	at 1.5 Mc/s		1.12	1.20	

Absolute maximum ratings

Parameter		Maximum	Units
Supply voltage	+2 V	2.1	V
	+5 V	5.5	V
	+30V	31.5	V
Mean count rate, continuous (per channel)		2	Mc/s
Peak count rate, at 25% duty cycle to 500ms (per channel)		5	Mc/s
Peak light intensity (per channel)	Maximum 10^4 photon/pulse and pulse width less than 1ns		
Temperature: -45˚ to 50˚C storage, 5˚C to 40˚C operating heat sink.			

Figure A.2.: Specifications of the *PerkinElmer* single-photon counting module array *SPCM-AQ4C* [91].

A.2. Preprint

Teleportation of entanglement over 143 km

Thomas Herbst*[1,2], Thomas Scheidl[1], Matthias Fink[1], Johannes Handsteiner[1], Bernhard Wittmann[1,2], Rupert Ursin[1,2] and Anton Zeilinger[1,2]

[1]*Institute for Quantum Optics and Quantum Information (IQOQI), Austrian Academy of Sciences, Boltzmanngasse 3, A-1090 Vienna, Austria*
[2]*Vienna Center for Quantum Science and Technology, Faculty of Physics, University of Vienna, Boltzmanngasse 5, A-1090 Vienna, Austria*

(Dated: March 14, 2014)

As a direct consequence of the no-cloning theorem [1], the deterministic amplification as in classical communication is impossible for quantum states. This calls for more advanced techniques in a future global quantum network [2, 3], e.g. for cloud quantum computing [4, 5, 6]. A unique solution is the teleportation of an entangled state, i.e. entanglement swapping [7], representing the central resource to relay entanglement between distant nodes. Together with entanglement purification [8, 9, 10, 11] and a quantum memory [12, 13] it constitutes a so-called quantum repeater [9, 14]. Since the afore mentioned building blocks have been individually demonstrated in laboratory setups only, the applicability of the required technology in real-world scenarios remained to be proven. Here we present a free-space entanglement-swapping experiment between the Canary Islands of La Palma and Tenerife, verifying the presence of quantum entanglement between two previously independent photons separated by 143 km. We obtained an expectation value for the entanglement-witness operator, more than 6 standard deviations beyond the classical limit. By consecutive generation of the two required photon pairs and space-like separation of the relevant measurement events, we also showed the feasibility of the swapping protocol in a long-distance scenario, where the independence of the nodes is highly demanded. Since our results already allow for efficient implementation of entanglement purification, we anticipate our assay to lay the ground for a fully-fledged quantum repeater over a realistic high-loss and even turbulent quantum channel.

Introduction

The vision of a global quantum internet is to provide unconditionally secure communication [5, 13], blind cloud computing [15] and an exponential speedup in distributed quantum computation [5, 6]. Teleportation of an entangled state, also known as entanglement swapping, plays a vital role in this vision. To date the entanglement-swapping protocol has been implemented in many different systems [16, 17, 18, 19, 20, 21, 22], owing to the fact that it represents a key resource for numerous quantum-information applications. Since an unknown single quantum state cannot be cloned nor amplified without destroying its essential quantum feature, the quantum repeater is the main resource for faithful entanglement distribution over long distances. The idea is to decompose the total distance into shorter elementary links, over which entanglement is shared, purified and eventually stored in quantum memories from which the entangled states can be retrieved on demand, once all the nodes are readily prepared. Finally the entanglement is swapped between adjacent nodes and faithfully extended over the whole distance. Entanglement purification and quantum memories serve solely to enhance the efficiency and the fidelity of the protocol, both of which are limited due to imperfection

---

*Correspondence: thomas.herbst@univie.ac.at

of the sources of entangled particles, of the involved quantum operations and of the interconnecting quantum channels. Entanglement swapping however provides the underlying non-classical correlations and constitutes the fundamental resource required for the implementation of a quantum repeater. Here we show that we were able to provide this resource via a realistic 143 km long-distance free-space (elementary) link under harsh atmospheric conditions, representing the largest geographical separation for this protocol to date. Furthermore, the simultaneous creation of two randomly generated photon pairs drastically reduces the signal-to-noise ratio, leading to technological requirements on the verge of practicability. Nonetheless, we ensured space-like separation of the remote measurement events, which is important for certain protocols e.g. quantum key distribution [23, 24].

The entanglement swapping protocol is realized via the generation of two entangled pairs, photons "0" and "1" and photons "2" and "3", for example the maximally entangled singlet states

$$\left|\Psi^-\right\rangle_{01} = \frac{1}{\sqrt{2}}(\left|H\right\rangle_0\left|V\right\rangle_1 - \left|V\right\rangle_0\left|H\right\rangle_1)$$

$$\left|\Psi^-\right\rangle_{23} = \frac{1}{\sqrt{2}}(\left|H\right\rangle_2\left|V\right\rangle_3 - \left|V\right\rangle_2\left|H\right\rangle_3) \tag{1}$$

where $\left|H\right\rangle$ and $\left|V\right\rangle$ denote the horizontal and vertical polarization states, respectively. The product state $\left|\Psi\right\rangle_{0123} = \left|\Psi^-\right\rangle_{01} \otimes \left|\Psi^-\right\rangle_{23}$ may be written as

$$\left|\Psi\right\rangle_{0123} = \frac{1}{2}[\left|\Psi^+\right\rangle_{03} \otimes \left|\Psi^+\right\rangle_{12} - \left|\Psi^-\right\rangle_{03} \otimes \left|\Psi^-\right\rangle_{12}$$
$$- \left|\Phi^+\right\rangle_{03} \otimes \left|\Phi^+\right\rangle_{12} + \left|\Phi^-\right\rangle_{03} \otimes \left|\Phi^-\right\rangle_{12}]. \tag{2}$$

Therefore a so-called Bell-state measurement (BSM) between photons "1" and "2" results randomly in one of the four maximally entangled Bell states $\left|\Psi^\pm\right\rangle_{12} = \frac{1}{\sqrt{2}}(\left|H\right\rangle_1\left|V\right\rangle_2 \pm \left|V\right\rangle_1\left|H\right\rangle_2)$ and $\left|\Phi^\pm\right\rangle_{12} = \frac{1}{\sqrt{2}}(\left|H\right\rangle_1\left|H\right\rangle_2 \pm \left|V\right\rangle_1\left|V\right\rangle_2)$ with an equal probability of 1/4. By that measurement, photons "0" and "3" are projected into the same entangled state as photons "1" and "2". Thus the entanglement is swapped from photons "0-1" and "2-3" to the photons "1-2" and "0-3" (Figure 1a). This procedure may also be seen as teleportation of the state of photon "1" onto photon "3" or photon "2" onto photon "0". Although the implementation of this protocol, solely based on linear optics, allows distinguishing between two out of four Bell states only [25], it provides a maximal fidelity of 1.

Experiment

Here we report successful entanglement swapping in an experiment performed on the Canary Islands, utilizing a 143 km horizontal free-space link between the Jacobus Kapteyn Telescope (JKT) building of the Isaac Newton Group of Telescopes (ING) on La Palma and the Optical Ground Station (OGS) of the European Space Agency (ESA) on Tenerife (Figure 1a). Both buildings are located at an altitude of 2400 m. The JKT served as the base station for the production of the two entangled photon pairs, for the BSM between photons "1" and "2" and for the polarization detection of photon "0" at Alice. The transmitter telescope, sending photon "3" to the receiving station on Tenerife, was installed on the rooftop of the JKT building. At the receiver the photons were collected by the 1 m diameter OGS reflector telescope and guided through the optical Coudé path to the setup for polarization analysis and the final measurement by Bob.

In our experimental setup (Figure 1b) a mode-locked femtosecond pulsed Ti:Saph laser emitted light with a central wavelength of 808 nm at a repetition rate of 80 MHz. Those near-infrared pulses were then frequency doubled to a central wavelength of 404 nm using second-harmonic generation in a type-I nonlinear β-barium borate (BBO) crystal. The individual polarization-entangled photon pairs employed in the protocol were generated via spontaneous parametric down-conversion (SPDC) in two subsequent type-II phase-matched BBOs [26] and coupled into single-mode (SM) optical fibres for spatial mode selection. The quality of entanglement was optimized by eliminating the spectral distinguishability [27, 28, 29], which is inherent to pulsed SPDC schemes. The first SPDC source provided the entangled state $\left|\Psi^-\right\rangle_{23}$, with photon "2" as one input photon for the BSM and photon "3" being guided through a 50 m long SM fibre to the transmitter telescope. The second SPDC source prepared the state $\left|\Psi^-\right\rangle_{01}$, where photon "1" was the second input photon for the BSM. Photon "0" was locally delayed in a 100 m fibre ($\sim$ 500 ns) and subsequently measured by Alice, thus ensuring space-like separation between Alice's and Bob's measurement events [24].
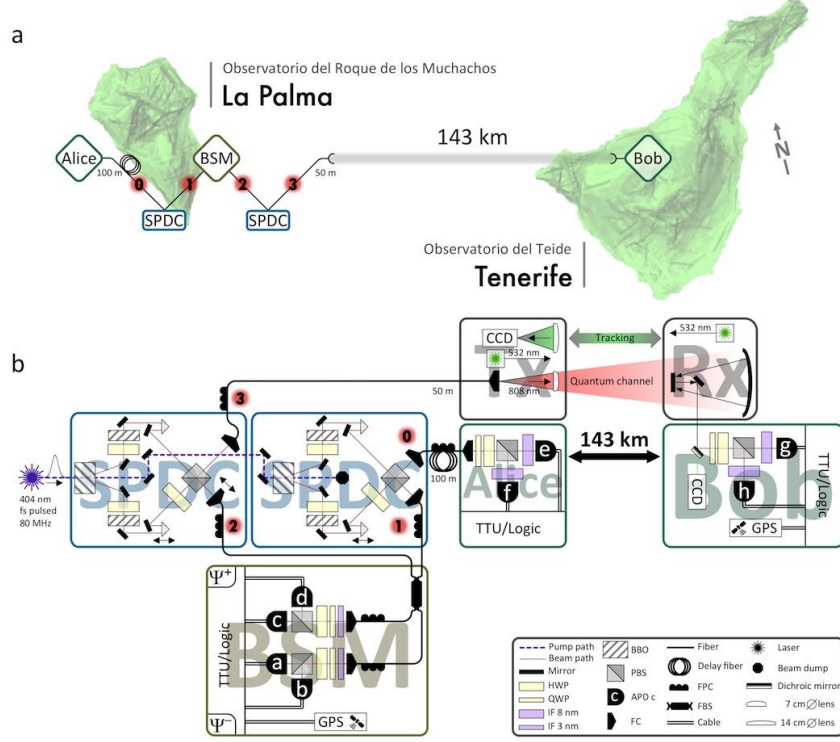
Figure 1: Entanglement swapping over a 143 km free-space channel between the Canary Islands La Palma and Tenerife. a, *Experimental scheme.* Both spontaneous parametric down-conversion (SPDC) sources, the Bell-state measurement (BSM) module and Alice were situated on La Palma and Bob on Tenerife. The two SPDC sources generated the entangled photon pairs "0-1" and "2-3". Photons "1" and "2" (photons are indicated by black numbers on red circles) were subjected to a BSM. A 100 m fibre delayed photon "0" with respect to photon "3", such that Alice's and Bob's measurements were space-like separated. Revealing entanglement of photons "0" and "3" between Alice and Bob verified successful entanglement swapping. **b,** *Experimental setup.* Two polarization-entangled photon pairs $\left|\Psi^-\right\rangle_{01}$ and $\left|\Psi^-\right\rangle_{23}$ were generated in two identical sources via spontaneous parametric down-conversion (SPDC) in a nonlinear β-barium borate (BBO) crystal. The photons were then coupled into single-mode (SM) fibres with fibre couplers (FC). Any polarization rotation in the SM fibres was compensated for by fibre polarization controllers (FPC). Photons "1" and "2" were spectrally filtered with interference filters (IF) with a full width at half maximum (FWHM) of 3 nm and overlapped in a fibre beam splitter (FBS). A subsequent polarization-dependent measurement was performed, utilizing a quarter wave plate (QWP), a half wave plate (HWP), a polarizing beam splitter (PBS) and four avalanche photodiodes (APD) a,b,c and d in the Bell-state measurement (BSM). Photon "3" was guided via a 50 m fibre to the transmitter (Tx) and sent to Bob in Tenerife, while photon "0" was delayed by a 100 m fibre before its polarization detection at Alice. The receiver (Rx) on Tenerife captured photon "3" where Bob performed his polarization-dependent measurement. Both Alice and Bob spectrally filtered their photons with IFs with 8 nm FWHM. All detection events were time stamped by time-tagging units (TTU) with a resolution of 156 ps and stored for subsequent analysis. See main text for detail.

In La Palma, the BSM was implemented using a tuneable fibre beam splitter (FBS) set to a 50:50 splitting ratio. While the spatial overlap of photons "1" and "2" is inherent to the FBS, a perfect temporal overlap is accomplished in the minimum of the Hong-Ou-Mandel [30] (HOM) interference dip. The latter was achieved by adjusting the optical path length for photon "2", by linearly moving the SM fibre coupler in the first SPDC source. Both output arms of the FBS were equipped with a quarter- and a half-wave plate followed by a polarizing beam splitter (PBS) in order to project on any desired polarization measurement basis. Intrinsic polarization rotations in the SM fibres were compensated for with in-fibre polarization controllers. The avalanche photodiodes (APDs) a, b, c and d, placed at the four outputs of the two PBSs, were connected to a home-made coincidence logic, providing the two valid outcomes of our BSM: simultaneous clicks of APDs (a & d) ∨ (b & c) or (a & b) ∨ (c & d) indicated that photons "1" and "2" were projected onto the maximally entangled $\left|\Psi^-\right\rangle_{12}$ singlet or $\left|\Psi^+\right\rangle_{12}$ triplet Bell state, respectively. As can be seen from Eq.(2), conditioned on

these BSM results, photons "0" and "3" were thus simultaneously projected onto the very same states $|\Psi^-\rangle_{03}$ and $|\Psi^+\rangle_{03}$, respectively. The projection onto the other Bell-states $|\Phi^\pm\rangle_{12}$ does not result in a coincidence detection event by the BSM and thus cannot be resolved with a linear-optics scheme. Furthermore, the two valid BSM outcomes together with Alice's detection events of photon "0" (APDs e and f) were fed into a logic AND gate, providing four possible combinations. These local 3-fold coincidence events on La Palma as well as the remote detection events of photon "3" on Tenerife (APDs g and h) were then recorded by two separate time-tagging units (TTUs) with a temporal resolution of 156 ps. In order to retrieve the final 4-folds between Alice's events and those measured on Bob's side we calculated the cross-correlation between the remotely recorded individual measurement data - both synchronized to GPS standard time. To compensate for residual relative clock drifts between the distant TTU-clocks we employed entanglement assisted clock synchronization [31] between consecutive 30 s measurements, allowing for a coincidence-time window of down to 5 ns.

Experimental results

The strong average attenuation of -32 dB over the 143 km free-space quantum channel calls for high production rates of the SPDC sources in order to operate well above the noise level of the single-photon detectors on Tenerife. However, pumping the SPDC sources with high pump intensities reduces the achievable entanglement-swapping visibility due to increased multi-pair emissions. Hence, a reasonable trade-off between count rates and visibility was required. In order to find the optimal operating point, we locally characterized our setup for various 2-fold count rates of the SPDC sources (Figure 2). The entanglement-
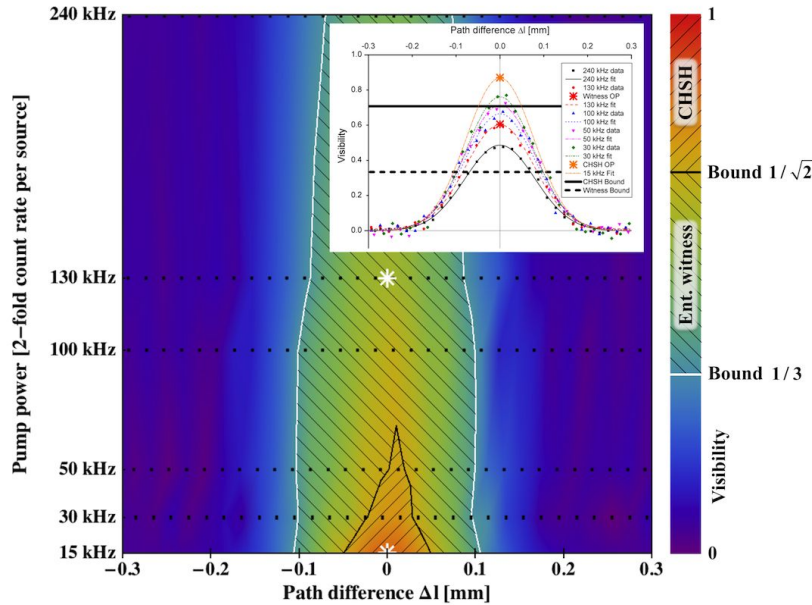
Figure 2: A density plot of the entanglement-swapping visibility versus path-length difference and pump power measured locally on La Palma. The abscissa represents the relative optical path-length difference Δl between photon "1" and "2" in the Bell-state measurement and the ordinate represents the 2-fold count rate of the sources. All measured data points are indicated by black dots in the density plot. The entanglement-swapping visibility is illustrated by rainbow colours where the entanglement-witness bound and the bound for the violation of a Clauser-Horne-Shimony-Holt (CHSH) type Bell inequality are represented by a white and a black isoline at a visibility of $1/3$ and $1/\sqrt{2}$, respectively. The hatched areas between visibilities of $1/3$ and $1/\sqrt{2}$ and above $1/\sqrt{2}$ mark the regions where entanglement can be shown by an entanglement witness and a CHSH type Bell inequality, respectively. A plot of the individual measurement runs including the respective Gaussian fits is illustrated in the inset. The operating point (OP) for the local test of the CHSH inequality (see orange star in inset) was chosen at a 2-fold rate of 15 kHz and zero delay. At this set point a visibility of 0.87 was achieved. For the entanglement-swapping experiment via the 143 km and -32 dB free-space link we tuned the setup to a 2-fold rate of 130 kHz and again perfect overlap at zero delay, resulting in a visibility of 0.6 (see red star in inset). In the density plot white stars indicate both OPs.

swapping visibilities of our setup varied between 0.87 at lowest 2-fold count rate (15 kHz 2-folds, about 1 Hz 4-folds) and 0.49 at full pump power (240 kHz 2-folds, 370 Hz 4-folds).

A traditional measure of entanglement is constituted by violation of a Clauser-Horne-Shimony-Holt [32] (CHSH) type Bell inequality. To accomplish this, a CHSH S-value above the classical bound of $S \leq 2$ needs to be experimentally obtained, being equivalent to an entanglement visibility of $1/\sqrt{2} \approx 0.71$. This was only achievable when operating at low pump powers and, given the resulting low count rates, therefore only feasible in the course of a measurement performed locally on La Palma. We accumulated data over 8000 s and measured the required S-value for both the singlet $|\Psi^-\rangle_{03}$ and triplet $|\Psi^+\rangle_{03}$ state. In total we detected 5647 singlet and 5618 triplet swapping events and violated the inequality with $S_{singlet} = 2.487 \pm 0.287$ and $S_{triplet} = 2.469 \pm 0.287$ at a 15 kHz 2-fold rate, respectively (Figure 3). This result clearly proves that photons "0" and "3" have been projected into an entangled state.

In order to reduce the accumulation time in the remote measurement scenario, we set each SPDC source to a local 2-fold rate of 130 kHz, corresponding to a locally detected 4-fold count rate of 100 Hz and an average entanglement visibility of the swapped state of approximately 0.60. We measured the expectation value of an entanglement-witness operator W, with $W < 0$ representing a sufficient condition for the presence of entanglement [33]. Our entanglement-witness operator is given as

$$W = \frac{1}{2} - \frac{1}{4}(1 + V_{HV} + V_{PM} + V_{RL}), \tag{3}$$

with V_{HV}, V_{PM}, V_{RL} being the correlation visibilities of state $|\Psi\rangle_{03}$ in the three mutually unbiased bases horizontal/vertical (HV), plus/minus (PM) and right/left (RL), respectively. The visibility is given by $V = (CC_{max} - CC_{min})/(CC_{max} + CC_{min})$ with the max (min) coincidence counts CC_{max} (CC_{min}). Inserting

Swapped state	Ψ^-_{03}	Ψ^+_{03}
V_{HV}	0.618 ± 0.067	0.610 ± 0.062
V_{PM}	0.607 ± 0.060	0.556 ± 0.065
V_{RL}	0.624 ± 0.056	0.542 ± 0.065
$\overline{V} = 1/3\,(V_{HV} + V_{PM} + V_{RL})$	0.616 ± 0.035	0.569 ± 0.037
$W = 1/2 - 1/4\,(1 + V_{HV} + V_{PM} + V_{RL})$	-0.212 ± 0.027	-0.177 ± 0.028
Local S-value	2.487 ± 0.287	2.469 ± 0.287
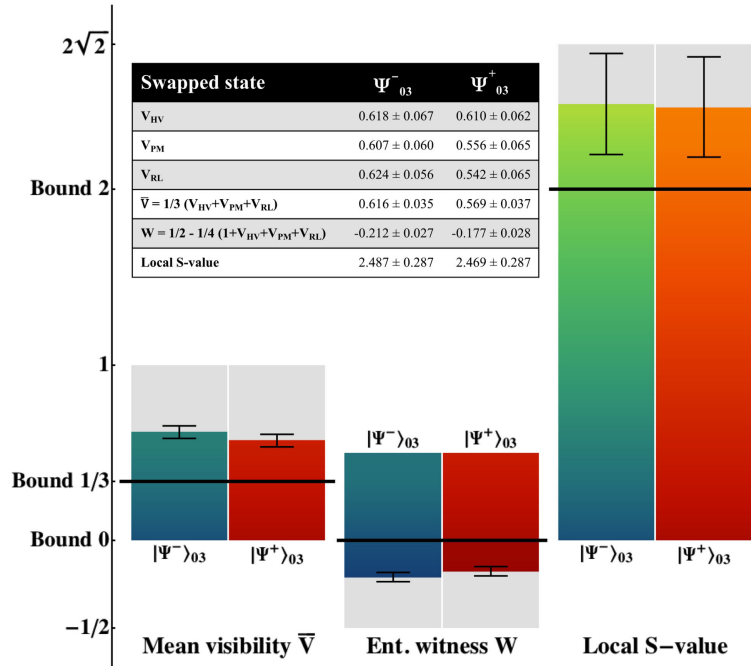
Figure 3: Summary of the measurement results. Over the 143 km free-space link we obtained an expectation value for the entanglement-witness operator W, more than 6σ below the classical bound of 0. This proved the presence of entanglement between the states $|\Psi^-\rangle_{03}$ and $|\Psi^+\rangle_{03}$. The violation of a Clauser-Horne-Shimony-Holt (CHSH) type Bell inequality was shown locally on La Palma underlining the quality of our setup. The bar chart illustrates the mean visibility $\overline{V}$ and the entanglement-witness operator W over the 143 km link as well as the locally measured S-value. All outcomes are given for the swapped states $|\Psi^-\rangle_{03}$ and $|\Psi^+\rangle_{03}$ with error bars derived from Poissonian statistics, $\pm 1\sigma$. The numerical values of the measurement results are given in the inset, including the individual visibilities V_{HV}, V_{PM} and V_{RL} in the three mutually unbiased bases horizontal/vertical (HV), plus/minus (PM) and right/left (RL) as well as the mean visibility $\overline{V}$, the entanglement-witness operator W and the locally measured S-value.

the measured visibilities into Eq.(3) yields a negative expectation value for the entanglement witness operator $W_{singlet} = -0.212 \pm 0.027$ and $W_{triplet} = -0.177 \pm 0.028$ with statistical significances of 7.99 and 6.37 standard deviations σ, respectively (assuming Poissonian photon statistics). Hence, we unambiguously demonstrated that the experimentally obtained states between photon "0" and "3" have become entangled over 143 km (Figure 3). These results were obtained from subsequent 30 s data files, accumulated over a measurement time of 271 min during 4 consecutive nights. In total, 506 and 492 entanglement-swapping events have been recorded for the singlet and triplet state, respectively.

Concluding comments

Our data demonstrate successful entanglement swapping via a long-distance free-space link under the influence of highly demanding environmental conditions, in fact more challenging than expected for a satellite-to-ground link. This proves the feasibility of quantum repeaters in a future space- and ground-based worldwide quantum internet. In particular, in a quantum repeater scheme, a single step of the purification method realized in Ref. [11] would increase our obtained visibilities beyond the bound for the violation of a CHSH type Bell inequality even in the remote scenario. Together with a reliable quantum memory, our results set the benchmark for an efficient quantum repeater at the heart of a global quantum-communication network.

References

[1] Wootters, W. K. & Zurek, W. H. A single quantum cannot be cloned. *Nature* **299**, 802–803 (1982).

[2] Bose, S., Vedral, V. & Knight, P. L. Multiparticle Generalization of Entanglement Swapping. *Physical Review A* **57**, 822–829 (1998).

[3] Kimble, H. J. The quantum internet. *Nature* **453**, 1023–1030 (2008).

[4] Cirac, J. I., Ekert, A. K., Huelga, S. F. & Macchiavello, C. Distributed Quantum Computation over Noisy Channels. *Physical Review A* **59**, 4249–4254 (1999).

[5] Nielsen, M. A. & Chuang, I. L. *Quantum Computation and Quantum Information* (Cambridge University Press, Cambridge, 2000).

[6] Ladd, T. D. *et al.* Quantum computers. *Nature* **464**, 45–53 (2010).

[7] Zukowski, M., Zeilinger, A., Horne, M. A. & Ekert, A. K. "Event-Ready-Detectors" Bell experiment via entanglement swapping. *Physical Review Letters* **71**, 4287–4290 (1993).

[8] Bennett, C. H. *et al.* Purification of noisy entanglement and faithful teleportation via noisy channels. *Physical Review Letters* **76**, 722–725 (1996).

[9] Briegel, H. J., Dür, W., Cirac, J. & Zoller, P. Quantum repeaters: the role of imperfect local operations in quantum communication. *Physical Review Letters* **81**, 5932–5935 (1998).

[10] Pan, J.-W., Simon, C., Brukner, C. & Zeilinger, A. Entanglement purification for quantum communication. *Nature* **410**, 1067–1070 (2001).

[11] Pan, J.-W., Gasparoni, S., Ursin, R., Weihs, G. & Zeilinger, A. Experimental entanglement purification of arbitrary unknown states. *Nature* **423**, 417–422 (2003).

[12] Clausen, C. *et al.* Quantum storage of photonic entanglement in a crystal. *Nature* **469**, 508–511 (2011).

[13] Gisin, N. & Thew, R. Quantum communication. *Nature Photonics* **1**, 165–171 (2007).

[14] Duan, L. M., Lukin, M. D. & Zoller, P. Long-distance quantum communication with atomic ensembles and linear optics. *Nature* **413**, 413–418 (2001).

[15] Barz, S. *et al.* Demonstration of blind quantum computing. *Science* **335**, 303–308 (2012).

[16] Pan, J.-W., Bouwmeester, D., Weinfurter, H. & Zeilinger, A. Experimental Entanglement Swapping: Entangling Photons That Never Interacted. *Physical Review Letters* **80**, 3891–3894 (1998).

[17] Jennewein, T., Weihs, G., Pan, J.-W. & Zeilinger, A. Experimental Nonlocality Proof of Quantum Teleportation and Entanglement Swapping. *Physical Review Letters* **88**, 17903 (2001).

[18] Halder, M. *et al.* Entangling independent photons by time measurement. *Nature Physics* **3**, 692–695 (2007).

[19] Yuan, Z.-S. *et al.* Experimental demonstration of a BDCZ quantum repeater node. *Nature* **454**, 1098–1101 (2008).

[20] Kaltenbaek, R., Prevedel, R., Aspelmeyer, M. & Zeilinger, A. High-fidelity entanglement swapping with fully independent sources. *Physical Review Letters* **79**, 040302 (2009).

[21] Ma, X.-S. *et al.* Experimental delayed-choice entanglement swapping. *Nature Physics* **8**, 479–484 (2012).

[22] Hofmann, J. *et al.* Heralded Entanglement Between Widely Separated Atoms. *Science* **337**, 72–75 (2012).

[23] Ekert, A. K. Quantum cryptography based on Bell's theorem. *Physical Review Letters* **67**, 661–663 (1991).

[24] Scheidl, T. *et al.* Violation of local realism with freedom of choice. *Proceedings of the National Academy of Sciences* **107**, 19708–19713 (2010).

[25] Calsamiglia, J. & Lütkenhaus, N. Maximum Efficiency of a Linear-Optical Bell-State Analyzer. *Applied Physics B* **72**, 67–71 (2001).

[26] Kwiat, P. G. *et al.* New High-Intensity Source of Polarization-Entangled Photon Pairs. *Physical Review Letters* **75**, 4337–4342 (1995).

[27] Kim, Y.-H. & Grice, W. P. Generation of pulsed polarization-entangled two-photon state via temporal and spectral engineering. *Journal of Modern Optics* **49**, 2309–2323 (2002).

[28] Kim, Y.-H., Kulik, S., Chekhova, M., Grice, W. & Shih, Y. Experimental entanglement concentration and universal Bell-state synthesizer. *Physical Review Letters* **67**, 010301 (2003).

[29] Poh, H., Lim, J., Marcikic, I., Lamas-Linares, A. & Kurtsiefer, C. Eliminating spectral distinguishability in ultrafast spontaneous parametric down-conversion. *Physical Review Letters* **80**, 043815 (2009).

[30] Hong, C. K., Ou, Z. Y. & Mandel, L. Measurement of subpicosecond time intervals between two photons by interference. *Physical Review Letters* **59**, 2044–2046 (1987).

[31] Ma, X.-S. *et al.* Quantum teleportation over 143 kilometres using active feed-forward. *Nature* **489**, 269–273 (2012).

[32] Clauser, J. F., Horne, M. A., Shimony, A. & Holt, R. A. Proposed Experiment to Test Local Hidden-Variable Theories. *Physical Review Letters* **23**, 880–884 (1969).

[33] Gühne, O. & Tóth, G. Entanglement detection. *Physics Reports* **474**, 1–75 (2009).

A.3. ESA report

ESA-ESTEC TEC-MMO

ESA Final Report

High-Speed Adaptive-Optics System based on Blind Optimization

by

Thomas Herbst

under the supervision of Josép-Maria Perdigues-Armengol

Contents

92

1. Introduction

This report gives a detailed description of the adaptive-optics system developed at ESA-ESTEC, TEC-MMO during my stay as a Young Graduate Trainee (YGT) under the supervision of Josép-Maria Perdigues-Armengol.

Usually an adaptive-optics system consists of a wavefront sensor and a deformable mirror to compensate for the measured wavefront errors. The drawback of using wavefront sensors is that ordinary models have frame rates in the order of 30 frames per second and need enough signal in order to operate flawlessly. To overcome the speed limit one can instead use a photo diode and measure the intensity reflected by the deformable mirror through a pinhole (or coupled into single-mode fiber as we did). With a so called stochastic parallel gradient descent algorithm (SPGDA) the optimum setting for the deformable mirror can be retrieved by maximization of the detected power. Implementation of the SPGDA in a field programmable gate array (FPGA) allows for high-speed and time-stable operation of the used mirrors, now limited by their mechanical response time.

The report is divided into four main parts: *Quickstart*, *Methods*, *Setup and Results*. *Quickstart* should allow the user to switch on the electronics of an installed system. In chapter *Methods* a short introduction to the mathematics and references for further studies are given.

Chapter *Setup* gives an overview over the setup and a detailed description to its building blocks.

Finally in *Results* the data of our indoor and outdoor measurements is presented and discussed.

2. Quick-Start

1. Connect all instruments (see 4.6 on page 32 for a detailed description)

2. Boot the *National Instruments* (NI) PXI-system (figure 2.1).

Figure 2.1.: The *National Instruments* (NI) PXI-system.

Figure 2.2.: The *Physik Instrumente* (PI) controller of the piezo tip/tilt mirror.

3. Switch on the *Physik Instrumente* (PI) controller of the piezo tip/tilt mirror (figure 2.2).

4. Switch on the *New Focus* ±15V power supply (figure 2.3).

Figure 2.3.: The *New Focus* ±15V power supply.

Figure 2.4.: The *fug* high voltage (HV) supply.

2

3

2.0

7. If required, change the parameters (see 4.7.3 on page 41 for a detailed description) and run the VI (figure 2.6).
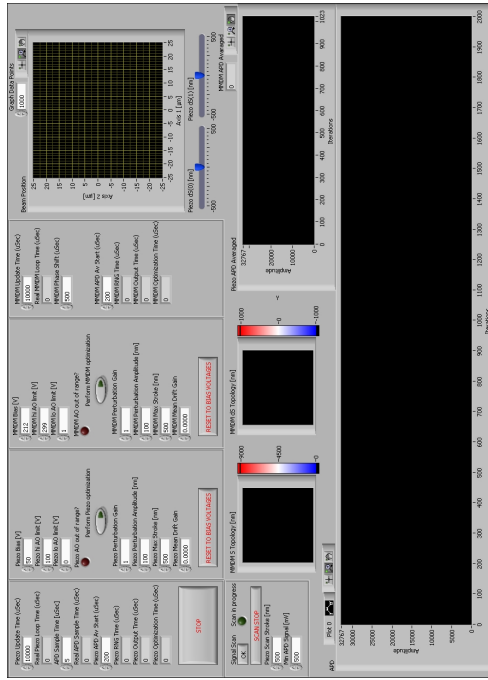
Figure 2.6.: The front panel of "Master SPGDA 2S BN LUTSqrtComp IntAv FAST MeanDriftComp (Host).vi".

8. Check the signal of the detector in the graph labeled "APD" at the bottom of the front panel and if necessary align the setup until you get a small signal or try a spiral search with the tip/tilt mirror by pushing the button "Signal Scan".

9. Once you have a small signal from the detector, activate the piezo tip/tilt mirror and the MMDM deformable mirror with the respective "Perform ... optimization" push button. Play around with different settings and find the optimum for the current situation.

   !Warning: **Do not reduce the update time of the mirrors below 800μs as you might run into the resonance frequency of the mirror and break it!**

5

2.0

5. Make sure the *fug* high voltage (HV) supply (figure 2.4) is set to 0V and power on the instrument. Check the voltage limit and set it to the maximum allowed value, i.e. 299V (new model 268V) for the deformable mirror used in this report. Push the output button and set it to ON. Now increase the voltage until the voltage limit is reached.
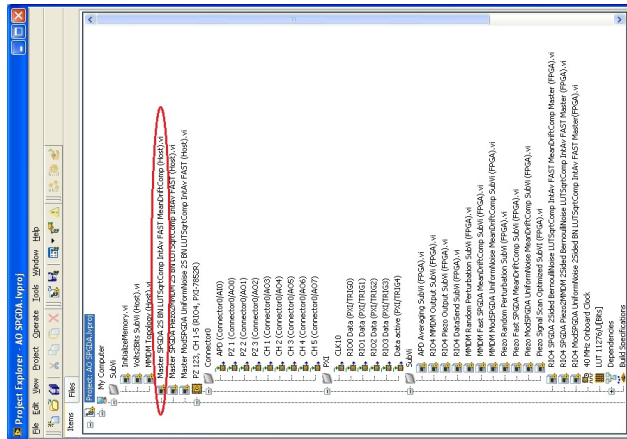

Figure 2.5.: The *LabView* project explorer.

6. Open the *LabView* project (figure 2.5) "..\Final Version\AO SPGDA.lvproj" and open the virtual instrument (VI) "Master SPGDA 2S BN LUTSqrtComp IntAv FAST MeanDriftComp (Host).vi"

4

10. To stop the VI hit the big, red "STOP" button on the front panel and do not use the stop button (shape of a stop sign) of *LabView*, otherwise the mirrors won't be set to zero and stay under high voltage.

11. To switch off the system, invert the start up procedure. Therefore reduce the high voltage to 0V, deactivate the output button and switch off the high voltage supply. Switch off the ±15V power supply and the PI controller. Close all programs and shut down the PXI-system.

2.0

3. Methods

This chapter provides an insight into the maths behind our blind optimization algorithm. In contrast to adaptive-optics systems with a wavefront sensor, our stochastic parallel gradient descent algorithm (SPGDA) is controlled from the feedback of a single-mode fiber. Applying stochastic perturbations Δu to all mirror actuators in parallel, allows the algorithm to find a minimum by looking at the gradient of the feedback metric $\frac{\Delta J}{\Delta u}$ [1-3]. As in the paper of M. Cohen et al. [3] we use a 2-sided approach with Bernoulli-distributed perturbations of fixed amplitude π only random in sign $\sigma = \pm 1$. 2-sided means that $\Delta J = J(u_1 + \Delta u_1, u_2 + \Delta u_2, ..., u_N + \Delta u_N) - J(u_1 - \Delta u_1, u_2 - \Delta u_2, ..., u_N - \Delta u_N)$. With the definitions

$$u_n^- = u_n^{(m)} - \sigma_n^{(m)}\pi, \qquad\qquad \sigma_n^{(m)} = \pm 1 \qquad\qquad (3.1)$$

$$u_n^+ = u_n^{(m)} + \sigma_n^{(m)}\pi \qquad\qquad (3.2)$$

$$\Delta u_n^{(m)} = u_n^+ - u_n^- = 2\sigma_n^{(m)}\pi \qquad\qquad (3.3)$$

$$\Delta J^{(m)} = J^{(m)}(u^+) - J^{(m)}(u^-) = J^+ - J^- \qquad\qquad (3.4)$$

the SPGDA can be simplified to

$$u_n^{(m+1)} = u_n^{(m)} + \gamma \frac{\Delta J^{(m)}}{\Delta u_n^{(m)}}, \qquad |\Delta u_n^{(m)}| = 2\pi = const. \qquad (3.5)$$

$$\Rightarrow \quad u_n^{(m+1)} = u_n^{(m)} + \gamma' \sigma_n^{(m)} \Delta J^{(m)}, \qquad \gamma' = \gamma/2\pi = const. \qquad (3.6)$$

Equation 3.6 was implemented in a high-speed field programmable gate array (FPGA) in order to calculate the actuator settings for our tip/tilt mirror (TTM) and micromachined deformable mirror (MMDM) (see section 4.7.2 on page 38).

To look further into adaptive optics with SPGDAs the following papers provide a good basis [4-9]. Also very interesting are references [8, 9].

7

6

4. Setup

4.1. Overview

This section gives an overview of the setup as it was implemented in the black lab. Figure 4.1 shows the optical setup.

A HeNe laser with a wavelength of 633nm was expanded to a collimated beam of ~4cm diameter and reflected into the telescope via the folding mirror. The telescope with a magnification of 4 consisted of a $\varnothing$=50mm, f=200mm lens and a $\varnothing$=25mm, f=50mm
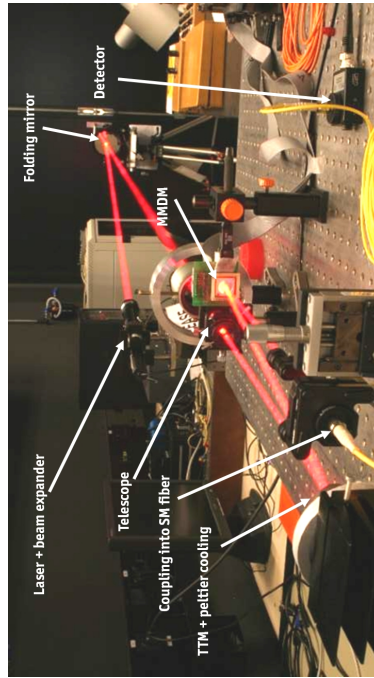
Figure 4.1.: Overview of the optical setup of the adaptive-optics system. The beam of a HeNe laser with a wavelength of 633nm was expanded to a collimated beam of 4cm diameter and reflected into the telescope via the folding mirror. In the telescope the beam was reduced to a $\varnothing$=1cm collimated beam and reflected by the tip/tilt mirror (TTM) and micromachined membrane deformable mirror (MMDM). A f=50mm lens focused the beam into the single mode fiber, guiding the coupled light to the detector.

8

lens and therefore reduced the beam to a ~1cm diameter collimated beam. This beam was reflected by the tip/tilt mirror (TTM) and micromachined membrane deformable mirror (MMDM) and focused into a single mode fiber by a f=50mm lens. Finally the fiber guided the coupled light to the detector, providing the feedback signal for the optimization algorithm.

The signal of the detector is fed into the strong field programable gate array (FPGA) module of the PXI-system (detailed description of the PXI-system in section 4.2) where the optimization algorithm calculates the new settings for the TTM and MMDM. 8 trigger lines in the backplane of the PXI-system distribute the updated output signals to four FPGA modules just used for analog output. All channels of the TTM and MMDM are updated synchronously, whereat the TTM and MMDM can be delayed in respect to each other. See figure 4.2 for a schematic of the feedback loop implemented in the PXI-system.

Figure 4.2.: Schematic of the feedback loop implemented in the PXI-system (details on the PXI-system in section 4.2). The signal of the photo diode is fed into the strong FPGA module where the optimization algorithm calculates the new settings for the TTM and MMDM. 8 trigger lines in the backplane of the PXI-system distribute the updated output signals to four FPGA modules just used for analog output. All channels of the TTM and MMDM are updated synchronously, whereat the TTM and MMDM can be delayed in respect to each other.

A detailed description on the wiring of the electronic setup shown in figure 4.3 can be found in section 4.6 on page 32.

9

4.2. PXI-System

In order to implement the optimization algorithms in a high-speed and time stable field programable gate array (FPGA) without any prior knowledge in hardware programming, we purchased the NI PXI-system. An introductory description of the PXI standard can be found on the NI homepage [10]:

"...PCI eXtensions for Instrumentation (PXI) is a rugged PC-based platform that offers a high-performance, low-cost deployment solution for measurement and automation systems. PXI combines the Peripheral Component Interconnect (PCI) electrical bus with the rugged, modular Eurocard mechanical packaging of CompactPCI and adds specialized synchronization buses and key software features. PXI also adds mechanical, electrical, and software features that define complete systems for test and measurement, data acquisition, and manufacturing applications. These systems serve applications such as manufacturing test, military and aerospace, machine monitoring, automotive, and industrial test.

National Instruments developed and announced the PXI specification in 1997 and launched it in 1998 as an open industry specification to meet the increasing demand of complex instrumentation systems. Currently, PXI is governed by the PXI Systems Alliance (PXISA), a group of more than 50 companies chartered to promote the standard, ensure interoperability, and maintain the PXI specification. Because PXI is an open specification, any vendor is able to build PXI products. CompactPCI, the standard regulated by the PCI Industrial Computer Manufacturers Group (PICMG), and PXI modules can reside in the same PXI system without any conflict because interoperability between CompactPCI and PXI is a key feature of the PXI specification..."

Figure 4.3.: Overview of the electronic setup of the adaptive-optics system. A more detailed description on the wiring can be found in section 4.6 on page 32.

10

11

"...PXI systems are composed of three basic components - chassis, system controller, and peripheral modules..." (see figure 4.4)
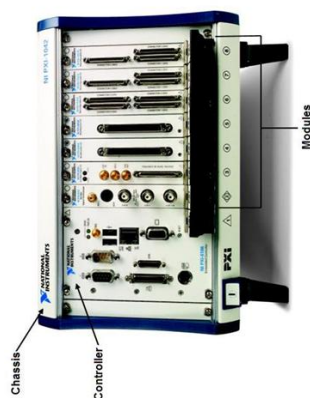
Figure 4.4.: Standard 8-Slot PXI Chassis Containing an Embedded System Controller and Seven Peripheral Modules [10].

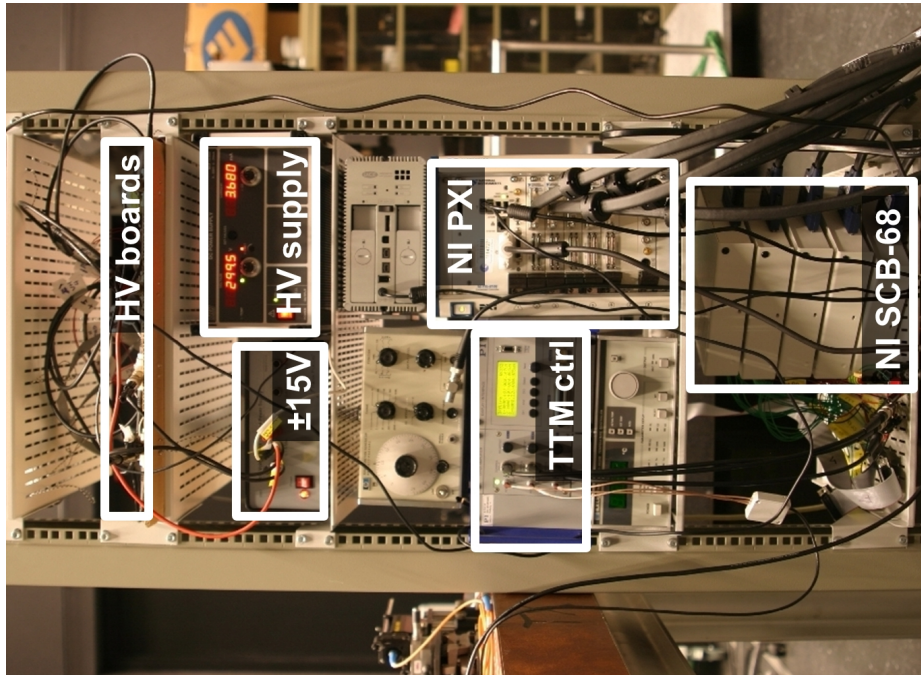"...The chassis contains the high-performance PXI backplane, which includes the PCI bus and timing and triggering buses. PXI modular instrumentation adds a dedicated 10 MHz system reference clock, PXI trigger bus, star trigger bus, and slot-to-slot local bus to address the need for advanced timing, synchronization, and sideband communication while not losing any PCI advantages..." (see figure 4.5)
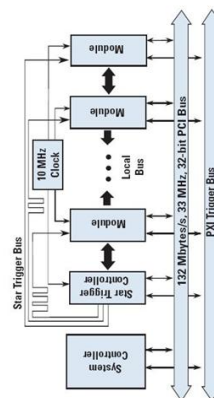
Figure 4.5.: PXI Timing and Triggering Buses - PXI combines industry-standard PC components, such as the PCI bus, with advanced triggering and synchronization extensions on the backplane. [10].

4.2.1. Controller and Modules

In our setup we used the NI PXI-1042Q quiet 8-slot chassis with the NI PXI-8108 Core 2 Duo controller with 2.53 GHz, 2 GB DDR2 RAM and Windows XP operating system. As the main FPGA module for implementation of the optimization algorithms we purchased the NI PXI-7852R Virtex-5 LX50 FPGA module. This module consists of

- 8 analog inputs (AIs), independent sampling rates up to 750 kHz, 16-bit resolution, ±10V
- 8 analog outputs (AOs), independent update rates up to 1 MHz, 16-bit resolution, ±10V
- 96 digital lines configurable as inputs, outputs, counters, or custom logic at rates up to 40 MHz
- 28800 flip-flops, 28800 6-input look-up-tables (LUTs), 1728kbit embedded block RAM
- 3 DMA channels for high-speed data streaming

The remaining 4 NI PXI-7831R Virtex-II 1M Gate FPGA modules are mainly used for output of the control voltages for the deformable mirror. Each board consists of

- 8 analog inputs (AIs), independent sampling rates up to 200 kHz, 16-bit resolution, ±10V
- 8 analog outputs (AOs), independent update rates up to 1 MHz, 16-bit resolution, ±10V
- 96 digital lines configurable as inputs, outputs, counters, or custom logic at rates up to 40 MHz
- 10240 flip-flops, 10240 6-input look-up-tables (LUTs), 720kbit embedded block RAM
- 3 DMA channels for high-speed data streaming

4.3. Tip/Tilt Mirror

The tip/tilt mirror (TTM) in our setup is a silver mirror glued to the *PI S-330.30* tip/tilt platform with two orthogonal pairs of PZT actuators. Each actuator pair tilts one axis and is connected in differential push-pull mode which means that every change in voltage increases one actuator and decreases the other. Thus thermal changes will only effect the Z-axis position and not the angular orientation. Figures 4.7 and 4.8 show the working principle and circuitry of the S-330.30 TTM [11].
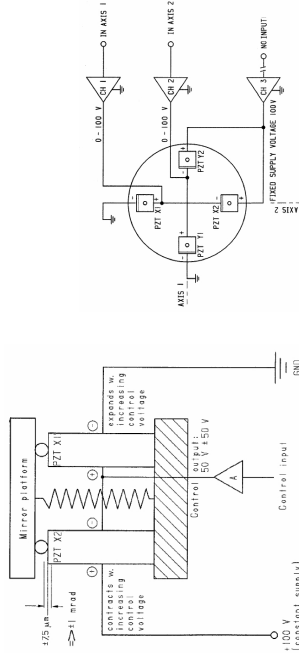
Figure 4.7.: S-330 differential-drive tip/tilt platform, working principle (only Axis-1 tip motion shown) [11].

Figure 4.8.: Circuitry of the S-330 [11].

Each axis can be tilted up to ± 1mrad with a control voltage in the range of 0 to +100V and a constant supply voltage of +100V. For zero tilt angle a voltage of +50V has to be applied. With the *PI E-503* amplifier a resolution of $\leq 0.05\mu$rad can be achieved and with a gain of 10 the TTM can be run with the 0 to +10V AO voltages of the NI FPGA modules.

15

All FPGA modules are connected via shielded cables to a *NI SCB-68* shielded input/output (I/O) connector block (see figure 4.6). These connector blocks are used to connect the wires of the tip/tilt and deformable mirror with the PXI-system.

Figure 4.6.: *NI SCB-68* shielded I/O connector block [10].

14

4.3. TIP/TILT MIRROR

The response of the TTM and the amplifier at 1kHz is shown in figure 4.9 where the yellow square wave is the signal from the AO of the NI FPGA module, the magenta line is after the amplification and the dark blue line is the mechanical response of the mirror. One can see that the rise time of the amplifier is around 100µs and the mechanical response of the TTM about 250µs with some post-pulse oscillations.
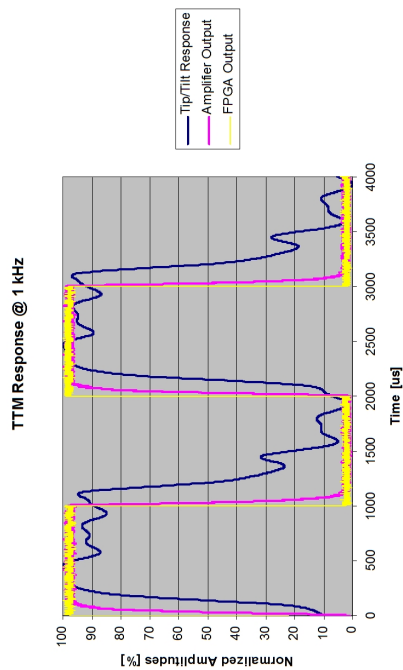
Figure 4.9.: Response of the TTM and the amplifier. The yellow square wave is the signal from the AO of the NI FPGA module, the magenta line is after the amplification and the dark blue line is the mechanical response of the TTM.

4.3. TIP/TILT MIRROR

Figure 4.10 shows the delay between the square wave signal from the FPGA and the mechanical response of the TTM as a function of the applied frequency. Three different strokes with an amplitude of 1V, 3V and 6V from zero position and after amplification were used for both axes of the mirror.
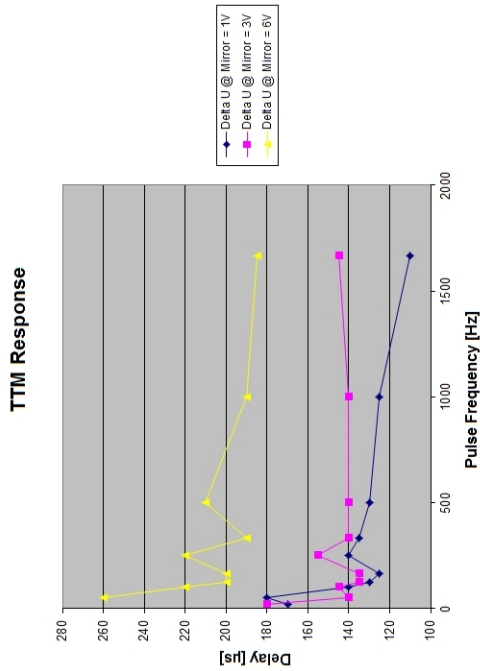
Figure 4.10.: Delay between FPGA square wave and the mechanical response of the TTM as a function of the applied frequency. Three different strokes with an amplitude of 1V, 3V and 6V from zero position, after amplification for both axes of the TTM.

The linearity and hysteresis of the TTM was measured by gradually changing the voltage applied on one axis (50V→100V→0V→50V) while keeping the other axis at zero position, i.e. 50V. For each voltage setting of the TTM, the fiber coupling was optimized by manually changing the fiber coupler xy-position with the micrometer screws and measuring the traverse. The results are illustrated in figure 4.11 and show a quite linear behavior with a difference of around 5μm at 50V depending from where the 50V are approached.
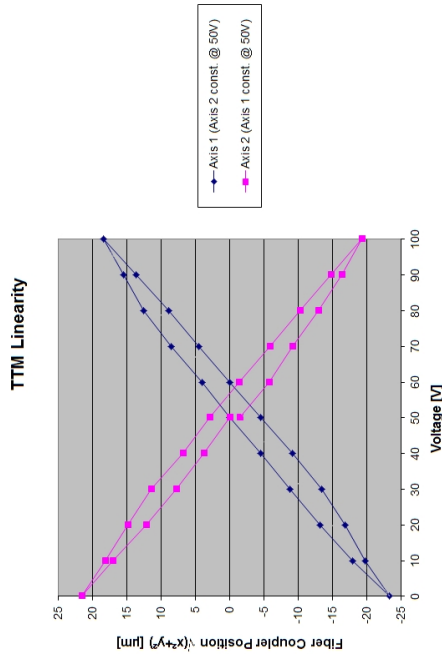
TTM Linearity

Figure 4.11.: Linearity and hysteresis of the TTM. Change of the fiber coupler position in μm for different voltages on one axis while keeping the other axis at zero position (50V).

The following two pages from the manual of the *PI S-330.30* show how to calculate the resonance frequency of the TTM and the specs of the platform. With the silver mirror in our setup the resonance frequency is about 2.7kHz and therefore well above the overall 1.6kHz limit of the deformable mirror.

---

5 Dynamic Behavior

In addition to the amplifier, controller and sensor bandwidths, the maximum operating frequency of a tilt platform depends on its mechanical resonant frequency. To estimate the effective resonant frequency of the tilt mirror system (platform + mirror), the moment of inertia of the mirror substrate must first be calculated.

Moment of inertia of a rotationally symmetric mirror:

$$I_m = m\left[\frac{3R^2 + H^2}{12} + \left(\frac{H}{2}+T\right)^2\right]$$

Moment of inertia of a rectangular mirror:

$$I_m = m\left[\frac{L^2 + H^2}{12} + \left(\frac{H}{2}+T\right)^2\right]$$

where:

m = *Mirror mass [g]*
I_M = *Moment of inertia of the mirror [g·mm²]*
L = *Mirror length perpendicular to the tilt axis [mm]*
H = *Mirror thickness [mm]*
T = *Distance, pivot point to platform surface (see technical data table for individual model) [mm]*
R = *Mirror radius [mm]*

Using the resonant frequency of the unloaded platform (see Technical Data table) and the moment of inertia of the mirror substrate, the system resonant frequency is calculated according to the following equation:

Resonant frequency of a tilt platform / mirror system:

$$f' = \frac{f_0}{\sqrt{1 + I_M/I_0}}$$

where:

f' = *Resonant frequency of platform with mirror [Hz]*
f_0 = *Resonant frequency of unloaded platform [Hz]*
I_0 = *Moment of inertia of the platform (see technical data table) [g·mm²]*
I_M = *Moment of inertia of the mirror [g·mm²]*

For more information on static and dynamic behavior of piezo actuators, see the "Tutorial" section of the PI Catalog, in particular pages 4-27 ff.

4.4. Deformable Mirror

We used a *OKO Technologies* micromachined membrane deformable mirror (MMDM) from *Flexible Optical B.V.* with an $\varnothing$=15mm aperture and 37 electrostatic actuators arranged in a honeycomb structure distributed over an active area of ca. $\varnothing$=12mm (see figures 4.12 and 4.13).

Figure 4.12.: *OKO* 15mm, 37-channel MMDM.

Figure 4.13.: Wiring of the 37 channels [12].

As the working principle of the mirror is based on electrostatic force, the deflection of the membrane is proportional to the square of the applied voltage. Applying the maximum voltage of 299V for our model (new model 268V) to all actuators simultaneously, will maximally deflect the center of the membrane by $\sim 9\mu m$. To reach such high voltages, the mirror is connected to two 20-channel HV boards with a gain of ~ 69. These boards amplify the low voltage signal from the AO of the FPGA module and and have to be operated with a ± 15V supply and a HV supply (more information on how to connect the devices in section 4.6). As the gain of 69 would amplify 10V to 690V, one has to limit the AO voltage of the FPGA to ~ 4.3V (new model ~ 3.9V).

Due to the fact that the electrostatic force can only attract the membrane, the MMDM has to be biased to half of its maximum center deflection (i.e. $4.5\mu m$) by applying 212V (new model 190V) to all actuators. From this position the mirror can be operated bi-directional. A more detailed description of our model can be found in the product guide of *Flexible Optical B.V.* [12] and is included in the following pages.

S-330 XY Tip/Tilt Platform   **User Manual PZ 107E**

6   S-330 Technical Data

Models	S-330.30 (open-loop)	S-330.10 / S-330.P10 (closed-loop)	Units
Active axes (fixed orthogonal tilt axes)	2	2	
Tip/tilt range 0 to 100 V[1]	±1	±1	mrad ±20%
Closed-loop tilt angle ≥	–	±1	mrad
Integrated feedback sensor	–	4 x strain gauge	
Open-loop / closed-loop resolution[2] ≤	0.05	0.1	µrad
Closed-loop linearity (typ.)	–	±0.2	%
Full-range repeatability (typ.)[3]	–	±2	µrad
Electrical capacitance[4]	3.6 per axis	3.6 per axis	µF ±20%
Dynamic operating current coefficient (DOCC)[5]	0.22 per axis	0.22 per axis	µA/(Hz x µrad)
Resonant frequency (f_0) without mirror[6]	3.3	3.3	kHz ±20%
Resonant frequency w/ Ø 25 x 8 mm glass mirror[7]	2.4	2.4	kHz ±20%
Distance, pivot point to platform surface	6	6	mm
Platform moment of inertia	1530	1530	g·mm²
Operating temperature range[8]	-20 to 80	-20 to 80	°C
Voltage connection	3 x Lemo fem. 2m cable	3 x Lemo fem. 2m cable	
Sensor connection	–	1 x Lemo, 2m cable	
Weight (w/o cables)	200	200	g ±5%
Material	Stainless steel case, Invar platform	Stainless steel case, Invar platform	
PICMA ceramic actuator[9]	no	no / yes	

Notes:

[1] Range: Operation over a -20 to +120 V range is possible if excursions to the limits are of short duration. See "Lifetime of PZTs" in the PI Catalog for more information. Special open-loop version with ± 2.5 mrad for 0-100 V is available on request.

[2] Resolution of PZT tip/tilt platforms is not limited by friction or stiction. Value is typical (RMS, 1σ) noise-equivalent motion with E-503 amplifier module.

[3] Full-Range Repeatability: Typical values, closed-loop mode. Since repeatability is a percentage of angle traveled, repeatability is significantly better for small ranges.

[4] Temperature Range: Small-signal value (measured at 1 V, 1000 Hz, 20°C, no load); large-signal values at room temperature are 30 to 50% higher. The capacitance of PZT ceramics changes with amplitude, temperature, and load up to 200% of the unloaded, small-signal capacitance at room temperature. For detailed information on power requirements, refer to the amplifier frequency response curves in the "PZT Control Electronics" section of the PI Catalog.

[5] Dynamic Operating Current Coefficient in µA per hertz and µrad. Example: Sinusoidal scan of 100 µrad at 10 Hz requires approximately 0.22 mA drive current.

[6] Unloaded Resonant Frequency: Lowest tilt resonant frequency around an active axis without mirror (well above the maximum operating frequency). For more resonance considerations, see p. 4-28 in the PI Catalog.

[7] Resonant Frequency with Mirror: Example of how a load (mirror) affects the (calculated) resonant frequency.

[8] Standard range, other temperature ranges on request. Closed-loop systems are calibrated for optimum performance at room temperature. Recalibration is recommended if operation is at a significantly higher or lower temperature.

[9] PICMA™ ceramics offer extended lifetime and compatibility with harsh conditions.

Release 1.1.1   **www.pi.ws**   **Page 10**

3

DEFORMABLE MIRRORS, TECHNICAL DATA

3.1 15mm 37-channel MMDM ("OKO mirror")

15 mm 37-channel MMDM was introduced in 1997 and has been the most popular deformable mirror ever made.

The mirror, shown in Fig. 3.1, consists of a silicon chip mounted over a PCB holder. The chip contains silicon nitride (composite) membrane, which is coated to form a mirror. The PCB contains the control electrode structure, spacer and connector. It also serves as the mirror package. The shape of the reflective membrane is controlled by voltages applied to the control electrodes with the membrane grounded.

The device can be used for fast dynamic correction of low-order optical aberrations such as defocus, astigmatism, coma, etc. in lasers, telescopes, ophthalmic devices, displays and imaging optics.

The scheme of the assembled mirror and the principle of control are illustrated in Fig. 3.2

3.1.1 Technical data

See Table 3.1 for typical technical parameters of the mirror.
Small surface defects are possible. They do not influence the quality of the mirror.

31

3. DEFORMABLE MIRRORS, TECHNICAL DATA

Figure 3.1: *Typical view of a 37-channel micromachined deformable mirror with and without package. Please note that these mirrors can be fabricated with different package designs, so the mirror you have may look differently.*
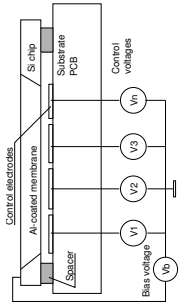
Figure 3.2: *Schematic section of the micromachined adaptive mirror.*

3.1.2 Actuator structure

The membrane is mounted over the printed actuator structure shown in Fig. 3.4. The center-to-center distance between actuators is 1.8mm. The whole actuator structure is located within 12mm circle under the mirror membrane.

The first (close to the mirror) cable connector controls central 19 actuators of the hexagonal structure and provides connection to the ground. The second connector controls 18 peripheral electrodes (two pins are not connected). In principle the mirror can be used with only one control board (19-channel variant) - ground the actuators 20...37 for reliable mirror operation.

19 amplifiers of the driver board connected to the first connector are used to drive the mirror actuators. The membrane is grounded (right jumper on the driver board in the upper position, no left jumper). The membrane can be

32   OKO Technologies • www.okotech.com

23

22

3. DEFORMABLE MIRRORS, TECHNICAL DATA

Figure 3.3: *Technical drawing of the package and mounting holes of the 15mm 37-channel MMDM*

Section A-A

9,0

45,0°

21,0

Membrane

5,0

21,0

Ø30,0

Ø20,0

Ø15,0

23

A

A

50,0

70,0

15,5

10,0

35,0

10

23,5

35,0

25

8 holes M4x6

10

23,0

Bottom

OKO Technologies ● www.okotech.com

25

34

3.1. 15MM 37-CHANNEL MMDM ("OKO MIRROR")

Table 3.1: *Technical parameters of 15mm 37-channel MMD mirror.*

Parameter	Value
Aperture shape	approximately circular
Mirror coating	Metal or Metal + dielectric
Aperture dimensions	15mm diameter
Number of electrodes	37 (19) (see Fig. 3.4)
Control voltages V_c	0 . . . 150 to 300 V, dependent on the mirror
Initial RMS deviation from plane	less than 0.45 μm
Main initial aberration	1.5 fringes at 630nm
Maximum deflection of the mirror center	10 μm
Package dimensions	see Fig. 3.3
Weight	140 g

connected to the amplifier number 20 (bias) by setting both jumpers on the amplifier board to the lower position - **this is not recommended**.

3.1.3 Optical quality

Typical interferograms of the mirror are shown in Fig. 3.5.

3.1.4 Specific remarks

When operated with 19 channels, use shorting link for the second connector to prevent charging of floating electrodes.
See also general remarks on page 69.

24

104

The response of our MMDM and the amplifier boars at 1kHz is shown in figure 4.14 where the yellow square wave is the signal from the AO of the NI FPGA module, the magenta line is after the amplification and the dark blue line is the mechanical response of the mirror. One can see that the rise time of the amplifier boards is quite long, but due to the quadratic behavior of the mirror, the deflection of the membrane reacts faster. A drawback of the membrane mirror is that there are strong post-pulse oscillations.

MMDM Response @ 1 kHz

Legend: MMDM Response, Amplifier Output, FPGA Output

y-axis: Normalized Amplitudes [%]
x-axis: Time [us]

Figure 4.14.: Response of the MMDM and the amplifier boards. The yellow square wave is the signal from the AO of the NI FPGA module, the magenta line is after the amplification and the dark blue line is the mechanical response of the MMDM.

3.1. 15MM 37-CHANNEL MMDM ("OKO MIRROR")

MIRROR SOCKET
VIEW FROM THE MIRROR SIDE

Figure 3.4: *The PCB actuator structure and the pinout (actuator numbers) of PGA connector, shown from the top (mirror surface) view. The cables should be connected from the back side with red-colored wire oriented to the "Ground" pin. See "Red wire" mark in the figure.*
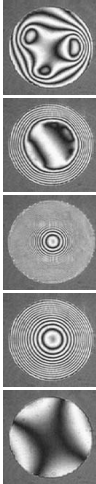
Figure 3.5: *Test of the mirror: zero voltage applied, control byte 180 applied to all actuators, control byte 255 applied to all actuators, control byte 255 applied to actuators 20 to 37, non-zero bytes applied to some actuators (left to right)*

26

27

4.5. Detector

In our setup a *DET36A/M* Si detector from *Thorlabs* [13] was used with an active area of 3.6 x 3.6mm, a wavelength range from 350nm to 1100nm and a rise time of 14ns (see figure 4.16).

Figure 4.16.: *DET36A/M* Si detector from Thorlabs with 3.6 x 3.6mm active area, 350nm - 1100nm wavelength range and 14ns rise time [13].

The detailed specs, response and bandwidth of the detector can be read on the following two pages of the manual [13]. One can see that the output voltage V_{OUT} is proportional to the load resistor R_{LOAD}. Thus higher R_{LOAD} increases the gain of the detector. On the other hand it decreases the bandwidth f_{BW} of the detector. Therefore one has to find the right R_{LOAD} for each experimental setup, which can be realized using a trim-pot. Via a BNC connector V_{OUT} (0-10V) can be read out and measured with the AI of our NI FPGA module.

Figure 4.15 shows the delay between the square wave signal from the FPGA and the mechanical response of the MMDM as a function of the applied frequency. Three different strokes with an amplitude of 15V, 30V and 45V from the bias position and after amplification were applied to all actuators of the mirror. At a frequency of approximately 1.4kHz the mechanical-response time increases drastically.
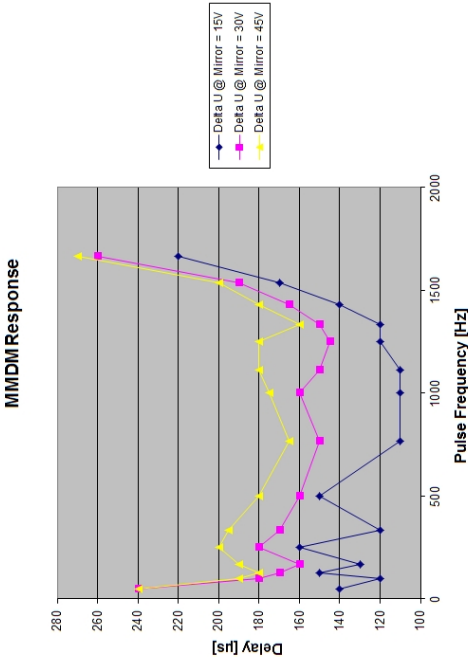
Figure 4.15.: Delay between FPGA square wave and the mechanical response of the MMDM as a function of the applied frequency. Three different strokes with an amplitude of 15V, 30V and 45V from bias position, after amplification for all actuators of the MMDM.

THORLABS

DET36A Operating Manual – High Speed Silicon Detector

Description:

The Thorlabs DET36A is a ready-to-use high-speed photo detector. The unit comes complete with a photodiode and internal 12V bias battery enclosed in a rugged aluminum housing. The DET36A includes a removable 1" optical coupler (SM1T1), providing easy mounting of ND filters, spectral filters, fiber adapters (SMA, FC and ST style), and other Thorlabs 1" stackable lens mount accessories.

The DET36A includes two #8-32 tapped mounting holes with a 0.25" mounting depth, while the DET36A/M has two M4 tapped mounting holes. A 12V A23 battery is included.

Specifications:

Electrical

Detector:		Silicon PIN
Active Area:		13mm² (3.6 x 3.6mm)
Wavelength Range:	λ	350 to 1100 nm
Peak Wavelength:	λ_{P}	970 nm (typ)
Peak Response (typ):	$\Re(\lambda_{P})$	0.65 A/W (typ)
Shunt Resistance:	R_{sh}	>10MΩ
Diode Capacitance:	C_{j}	40pF
Rise/Fall Time:	t_{r}	14ns (max.)
Linearity Limit (Current):		1mA
(Power):		1.5mW (min @λ_{P})
NEP (750nm):		1.6x10⁻¹⁴ W/√Hz (max.)
Bias Voltage:	V_{B}	10 V (8V min)
Dark Current²:	I_{D}	0.35nA (06nA max.)
Output Voltage:	V_{OUT}	0 to 10V
Damage Threshold:		100mW/cm²

General

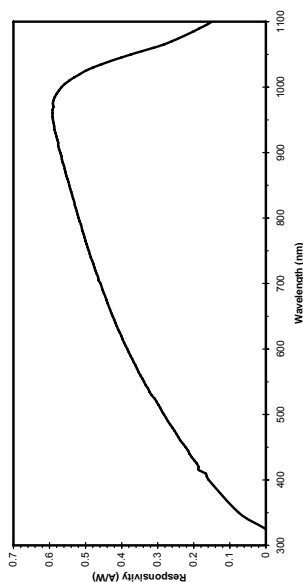| On / Off Switch:	Slide
Battery Check Switch:	Momentary Pushbutton
Output:	BNC (DC Coupled)
Package Size:	2.8"x1.9" x 0.83" 70mm x 48mm x 21mm
PD Surface Depth:	0.16" (4.1mm)
Weight:	0.2 lbs
Accessories:	SM1T1 Coupler SM1RR Retainer Ring
Storage Temp:	-25 to 70°C
Operating Temp:	10 to 50°C
Battery¹:	A23, 12V_{DC}, 40mAh
Low Battery Voltage³	(See 'Battery Check')
V_{OUT} (Hi-Z):	~8V
V_{OUT} (50Ω):	~400mV

1. All measurements performed with a 50Ω load unless stated otherwise.
2. Measured with specified Bias Voltage.
3. Assumes the battery voltage drops below 9.6V. The reverse protection diode generates a 0.6V drop.

Figure 1 - Typical DET36A Spectral Responsivity Curve

Operation

Thorlabs DET series are ideal for measuring both pulsed and CW light sources. The DET36A includes a reversed-biased PIN photo diode, bias battery, and ON/OFF switch packaged in a rugged housing. The BNC output signal is the direct photocurrent out of the photo diode anode and is a function of the incident light power (P) and wavelength (λ). The Spectral Responsivity, $\Re(\lambda)$, can be obtained from Figure 1 to estimate the amount of photocurrent to expect. Most users will wish to convert this photocurrent to a voltage (V_{OUT}) for viewing on an oscilloscope or DVM. This is accomplished by adding an external load resistance, R_{LOAD}. The output voltage is derived as:

$$V_{OUT} = P * \Re(\lambda) * R_{LOAD}$$

It should be noted that the load resistor will react with the photodetector junction capacitance (C_{J}) to limit the bandwidth. For best frequency response, a 50Ω terminator should be used. The bandwidth (f_{BW}) and the rise-time response (t_{R}) can be approximated using the diode capacitance (C_{J}) and the load resistance (R_{LOAD}) as shown below:

$$f_{BW} = 1 / (2 * \pi * R_{LOAD} * C_{J})$$
$$t_{R} = 0.35 / f_{BW}$$

For maximum bandwidth, we recommend using a 50Ω coax cable with a 50Ω terminating resistor at the opposite end of the coax. This will also minimize ringing by matching the coax with its characteristic impedance. If bandwidth is not important, you may increase the amount of voltage for a given input light by increasing the R_{LOAD}.
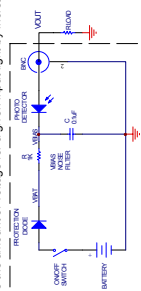
Figure 2 – Circuit Schematic

Setup

- Unpack the optical head, install a Thorlabs TR-series ½" diameter post into one of the #8-32 (M4 on /M version) tapped holes, located on the bottom and side of the sensor, and mount into a PH-series post holder.
- Attach a 50Ω coax cable (i.e. RG-58U) to the output of the DET. Select and install a terminating resistor to the remaining end of the cable and connect to a voltage measurement device. See the 'Operation' Section to determine resistor values. Thorlabs sells a 50Ω terminator (T4119) for best frequency performance and a variable terminator (VT1) for output voltage flexibility. Note the input impedance of your measurement device since this will act as a terminating resistor. A load resistor is not necessary when using current measurement devices.
- Power the DET on using the power switch. To check battery voltage, see 'Battery Check' below.
- Install any desired filters, optics, adapters, or fiber adapters to the input aperture. **Caution:** The DET36A was designed to allow maximum accessibility to the photodetector by having the front surface of the diode flush with the outside of the DET housing. When using fiber adapters, make sure that the fiber ferrule does not crash into the detector. Failure to do so may cause damage to the diode and / or the fiber. An easy way to accomplish this is to install a SM1RR retaining ring (included with the DET36A) inside the 1" threaded coupler before installing the fiber adapter
- Apply a light source to the detector.

Battery Check and Replacement

Battery Check
Thorlabs new DET series includes a battery check feature that will allow the user to monitor the bias voltage on the output BNC. Simply hold down the "VBIAS OUT" bottom located on the bottom edge of the unit. The bias voltage will be output to the BNC. If a high impedance load is used (>10kΩ), the output will be equal to the bias voltage. This feature includes a 1.05kΩ current limiting resistor (R_{CL}) to prevent excessive loading of the battery if using small terminating resistors. For example, a 50Ω load resistor with a 10V bias will produce a 200mA current without this resistor. This will significantly decrease lifetime of the battery. The output bias voltage will be dependent on the load

4.6. Wiring

This section gives a detailed description on how to set up and connect all devices correctly with each other.

The chassis of the PXI-system houses the controller in slot 1, four *NI PXI-7831R* FPGA modules in slots 2-5 and module *NI PXI-7852R* in slot 6. Each module has three 68-pin reconfigurable I/O (RIO) connectors. Connector0 provides the analog I/O lines and is called RMIO where M stands for multifunction. Whereas Connector1 and 2 are for digital lines only, therefore called RDIO with D for digital.

Connector0 of each module is connected to a *NI SCB-68* connector block via a *NI SHC68-68-RMIO* shielded cable. The screw terminals of the connector blocks are used to screw the wires for connecting the detector, the TTM- and the MMDM-channels. Table 4.1 on the next page shows which screw terminals on which connector block correspond to which device and their channels. The BNC connector to the detector DET is screwed to AI0 and its ground AIGND0 of the *SCB-68* block which is connected to the *NI PXI-7852R* FPGA module in slot 6 of the PXI-System. Also the BNC connectors for the TTM channels PZ1-3 are screwed in the same connector block into terminals AO0-2 and AOGND0-2 respectively. The remaining five AO terminals and two AOGNDs on this block are used to connect channels CH1-5, ground GND and the membrane of the MMDM. All the other channels of the MMDM are distributed according to table 4.1 over the remaining *SCB-68* connector blocks.

The wires for channels CH1-19, ground GND and membrane are soldered to a single 25-pin D-Sub connector. The same for CH20-37, GND and membrane. Two 26-pin flat ribbon cables are connected to the 25-pin D-Sub connectors on one end and to the 26-pin connectors of the HV boards on the other end. It has to be mentioned that the pin numbers of the flat ribbon cables do no directly correlate with the channel numbers of the MMDM as can be seen in the pinout schemes of the MMDM and the HV boards in the bottom of page 35. From each HV board a 20-pin flat ribbon cable is used to finally connect the MMDM. Channels 1-19 have to be plugged to the connector closer to the mirror. The HV boards themselves are powered by a *New Focus* ±15V supply and a *fug* limited HV supply with the negative HV connected to ground. The HV limit has to be set to the maximum allowed voltage for the MMDM and can be found in the technical passport of the mirror. In our case it is 299V (new model 268V). When powering up the MMDM system, first switch on the ±15V supply and then the HV supply with the voltage set to 0V and output set to OFF. Now check the voltage limit and set it to the

Module	PXI-Slot#	RIO#	SCB-68 Screw Terminal	26 D-Sub Pin#	Label	Device
					DET	Detector
PXI-7852R	6	4	AI0/AIGND0			
			AO0/AOGND0		P21	TTM
			AO1/AOGND1		P22	
			AO2/AOGND2		P23	
			AOGND3	26	GND	
			AOGND4	1	Membrane	
			AO3	12	CH1	
			AO4	20	CH2	
			AO5	13	CH3	
			AO6	9	CH4	
			AO7	5	CH5	
PXI-7831R	5	3	AO0	8	CH6	
			AO1	16	CH7	
			AO2	19	CH8	
			AO3	17	CH9	MMDM CH1-19
			AO4	14	CH10	
			AO5	11	CH11	
			AO6	2	CH12	
			AO7	3	CH13	
PXI-7831R	4	2	AO0	4	CH14	
			AO1	6	CH15	
			AO2	7	CH16	
			AO3	10	CH17	
			AO4	15	CH18	
			AO5	18	CH19	
PXI-7831R	3	1	AOGND0	26	GND	
			AOGND1	1	Membrane	
			AO6	16	CH20	
			AO7	18	CH21	
			AO0	17	CH22	
			AO1	20	CH23	MMDM CH20-37
			AO2	15	CH24	
			AO3	3	CH25	
			AO4	5	CH26	
			AO5	2	CH27	
			AO6	4	CH28	
			AO7	6	CH29	
PXI-7831R	2	0	AO0	8	CH30	
			AO1	7	CH31	
			AO2	10	CH32	
			AO3	9	CH33	
			AO4	12	CH34	
			AO5	11	CH35	
			AO6	14	CH36	
			AO7	13	CH37	
				19	NC	

Table 4.1.: Wiring scheme for *NI SCB-68* connector blocks.

desired value, i.e. 299V (new model 268V). Afterwards activate the output and increase the voltage until the maximum allowed voltage for the MMDM.

Detector *DET36A/M* is connected to the BNC cable DET with a trim-pot as shunt resistor between signal and ground. The tunable resistor allows for adjusting the gain of the detector as described in section 4.5.

Channels CH1-3 of the TTM are connected to the respective LEMO jacks of the PI controller rack. The control-input connectors of the rack are connected with the respective cables labeled PZ1-3 from the *SCB-68* block.

The wiring of the whole system is depicted on the next page.
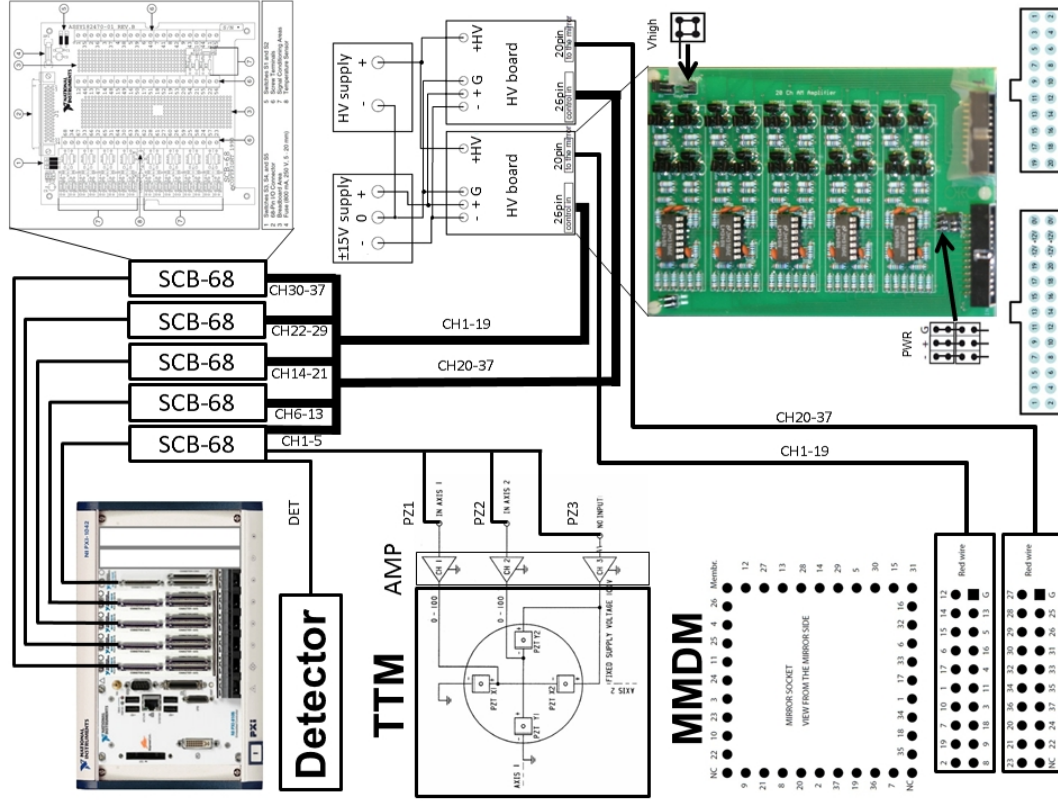
4.7. Software

In the Software section of this report a close look will be taken on the *NI LabVIEW FPGA Module* software add-on, on how the optimization algorithm was implemented in *LabVIEW* source code and the different *LabVIEW* projects that have been programmed.

4.7.1. LabVIEW FPGA Module

As written on the NI homepage [14]:

"...The NI LabVIEW FPGA Module can help you program a field programmable gate array (FPGA) with a LabVIEW block diagram. Under the hood, the module uses code generation techniques to synthesize the graphical development environment to FPGA hardware. This block diagram approach to FPGA is well-suited for an intuitive depiction of the inherent parallelism that FPGAs provide..."

For programming with the *NI LabVIEW FPGA Module* one has to create a *LabVIEW* project first. The project explorer (see page 37) contains all hardware modules that are available in the PXI-system. For instance the PXI controller called "My Computer" and the five NI FPGA boards "PZ 123, CH 1-5 (RIO4, PXI-7852R)", "CH 6-13 (RIO3, PXI-7831R)", "CH 14-21 (RIO2, PXI-7831R)", "CH 22-29 (RIO1, PXI-7831R)" and "CH 30-37 (RIO0, PXI-7831R)". The caption in parentheses describes in which slot of the PXI-system the hardware is located and its product code, e.g. "RIO0, PXI-7831R" corresponds to the NI FPGA board *PXI-7831R* in slot 2, "RIO1, PXI-7831R"→board *PXI-7831R* in slot3 and so on. The caption before the parentheses can be changed by the user.

VIs located directly in "My computer" are so called "Host VIs". These VIs run on the CPU of the controller and are used to call the VIs running on the FPGA. Therefore VIs located in one of the FPGA-board folders are called "FPGA VIs". Each folder of an FPGA board also contains the used AI, AO, DIO and trigger lines, e.g. "APD (Connector0/AI0)". Again the caption in parentheses describes the hardware address and the text before can be set by the user. FPGAs also allow for implementation of user defined clocks, memory, first-in first-out (FIFO) resources and lookup tables (LUTs), e.g. "LUT 11276/U[Bits]" which is a LUT in order to avoid resource-intensive division in the FPGA. FIFOs are mainly used to either exchange data between loops and other part of an FPGA VI, or between the FPGA VI and the Host VI. These FIFOs are called "Target-scoped FIFOs" and "Direct Memory Access (DMA) FIFOs" respectively.

Graphical programming on an FPGA is almost the same as programming a standard *LabVIEW* VI, with the difference that there are not all functions available in the tools palette and the VI has to be compiled before execution. Compiling automatically starts when pressing the run button or with a right click on the FPGA VI and selecting "Compile".

To get into *LabVIEW FPGA Module* software a helpful on-line tutorial can be found on the NI homepage [15].

4.7.2. Implementation of the Algorithm

The analog I/Os of the FPGA modules have a 16-bit resolution, which means that the analog range from -10V to 10V can be divided in 2^{16} bits and the desired voltage is addressed by an I16 number ranging from -2^{15} to $+2^{15} - 1$, i.e. -32768 to +32767. Therefore the conversion formula to AO voltage is $U_{AO} = k_{bit} \cdot U_{bit} = \frac{10}{32767} \cdot U_{bit}$. With a gain of 69 of the HV boards the conversion from AO voltage to high voltage is $U_{HV} = k_{AO} \cdot U_{AO} = 69 \cdot U_{AO}$. As the stroke of the MMDM is proportional to the applied voltage squared, the formula for the stroke is $S = k_{HV}^2 \cdot U_{HV}^2$. The technical passport of the mirror states a maximum deflection of $\sim 9\mu m$ at $\sim 300V$ thus $9000nm = k_{HV}^2 \cdot 300^2 V^2 \Rightarrow k_{HV}^2 = \frac{1mm}{10V^2}$ and

$$S_{[nm]} = k_{HV}^2 \cdot U_{HV}^2 = k_{HV}^2 \cdot k_{AO}^2 \cdot U_{AO}^2 = k_{HV}^2 \cdot k_{AO}^2 \cdot k_{bit}^2 \cdot U_{bit}^2 = \frac{1}{10} \cdot 69^2 \cdot \frac{10^2}{32767^2} \cdot U_{bit}^2 = k_{tot}^2 \cdot U_{bit}^2. \tag{4.1}$$

Due to the quadratic behavior of the total stroke, the amount of a small stroke for a given voltage change depends on the starting voltage to which the voltage change is added. The change in stroke depending on a change in voltage can be derived by differentiation of S

$$\frac{dS}{dU_{bit}} = 2 \cdot k_{tot}^2 \cdot U_{bit} \Rightarrow \Delta U_{bit} = \frac{\Delta S_{[nm]}}{2 \cdot k_{tot}^2 \cdot U_{bit}} \approx 11276 \frac{\Delta S_{[nm]}}{U_{bit}}. \tag{4.2}$$

In order to avoid a resource-intensive division in the FPGA, a LUT was implemented mapping each possible input value $U_{bit} \rightarrow \frac{11276}{U_{bit}}$.

Having a look at the optimization algorithm, one gets

$$U_{bit}^{N+1} = U_{bit}^N + \gamma \cdot \frac{\Delta J^N}{\Delta U_{bit}^N} = U_{bit}^N + \frac{\gamma}{11276} \cdot U_{bit}^N \cdot \frac{\Delta J^N}{\Delta S_{[nm]}^N}. \tag{4.3}$$

with the gain of the algorithm γ and the intensity change between two different mirror settings $\Delta J = J(u_1 + \Delta u_1, u_2 + \Delta u_2, ..., u_N + \Delta u_N) - J(u_1 - \Delta u_1, u_2 - \Delta u_2, ..., u_N - \Delta u_N)$. As the stroke of the stochastic perturbations ΔS will only vary in sign but not in absolute

value, the division by $|\Delta S|$ can be transferred to the host VI leaving a multiplication with $Sign(\Delta S)$. This gives us

$$U_{bit}^{N+1} = U_{bit}^N + \underbrace{\frac{\gamma}{|\Delta S_{[nm]}^N|} \cdot 11276}_{\text{from host VI}} \cdot U_{bit}^N \cdot Sign(\Delta S_{[nm]}^N) \cdot \Delta J^N. \tag{4.4}$$

Now we can have a look at the sub VI which generates the random perturbations for the MMDM (see figure 4.17).

Figure 4.17.: Sub VI to generate random perturbations for the MMDM.

If "Perform MMDM optimization" is true, a while loop is carried out and will repeat 37 times (0-36). The input variable "MMDM In" is an array of 37 elements containing the settings of all MMDM channels. Each element is fed into the LUT separately with each loop repetition. The output is multiplied with "MMDM Perturbation Amplitude (nm)" which corresponds to $|\Delta U_{bit}| = \frac{|\Delta S_{[nm]}|}{U_{bit}}$. Now this value is multiplied with a random sign, implemented with a random the number generator (RNG) of the functions palette. The RNG is set to randomly output -1 or 0. This is multiplied by 2 and summed up with 1 leading to -1 or +1. The final set of random perturbations ΔU_{bit} is written into an initialized array and ready for output as "MMDM dU" array. Input variable "MMDM Max Stroke (nm)" is just to make sure that the stroke cannot exceed a defined limit. The random perturbations are then added to the actual settings of the MMDM channels and the intensity of the light coupled into fiber is measured. Afterwards the perturbations are subtracted from the original settings of the MMDM and the intensity is measured again. This gives us ΔJ and the algorithm is able to calculate a new set point for the MMDM. The sub VI carrying out the algorithm of equation 4.4 is shown in figure 4.18.

The input variables "Delta APD (Bits)", "MMDM Perturbation Gain/dS/11276" and "MMDM In" correspond to ΔJ, $\underbrace{\frac{\gamma}{|\Delta S^N_{[nm]}| \cdot 11276}}_{\text{from host VI}}$ and U_{bit} respectively. Therefore they are multiplied for each element of "MMDM In" and also multiplied with the sign of each random perturbation of "MMDM Perturbation In". These values are added to the actual settings "MMDM In". Again we have implemented some limits in order not to exceed the maximum allowed stroke. Outside of the loop the mean value over all 37 actuators is calculated and the bias position "MMDM Bias (Bits)" is subtracted. This can be used to force the MMDM in its bias position. The strength of this effect can be controlled with "MMDM Mean Drift Gain". Finally the new MMDM actuator settings "MMDM Out" are ready to be applied to the mirror and the overall loop is repeated.

4.7.3. Files

In this section the the path and name of the individual projects are given. Also the parameters and functions of the most complex program are explained.
The folder "...\Final Version" contains three subfolders:

- AO
- AO Measurement
- Mirror Tests

with the projects "AO SPGDA.lvproj", "AO SPGDA MEASUREMENT.lvproj" and "Mirror Tests.lvproj" respectively. *LabVIEW* project "AO SPGDA.lvproj" contains host VIs for the adaptive-optics optimization. "AO SPGDA MEASUREMENT.lvproj" contains the same VIs as "AO SPGDA.lvproj" with the additional feature of being able to write measurement data to files. "Mirror Tests.lvproj" contains host VIs for testing the latency of the system and mirror strokes.
The project "...\Final Version\AO Measurement\AO SPGDA MEASUREMENT.lvproj" contains the host VI "Master SPGDA 2S BN LUTSqrtComp IntAv FAST MeanDriftComp MEASUREMENT (Host).vi" which is shown in figure 4.19. Its front-panel objects are alphabetically listed and explained in the tables on pages 43-45.
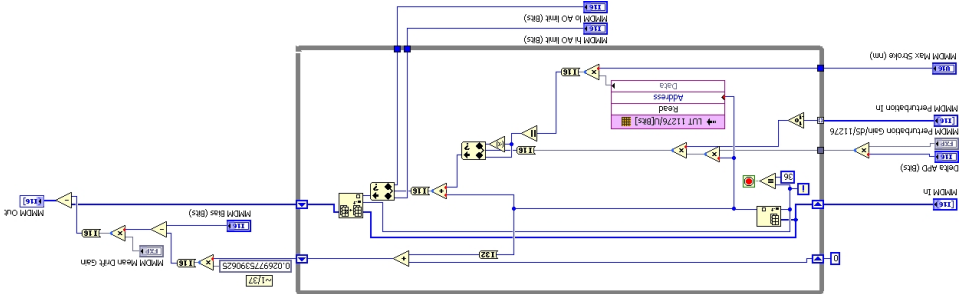

Figure 4.18.: Sub-VI to implement the optimization algorithm.

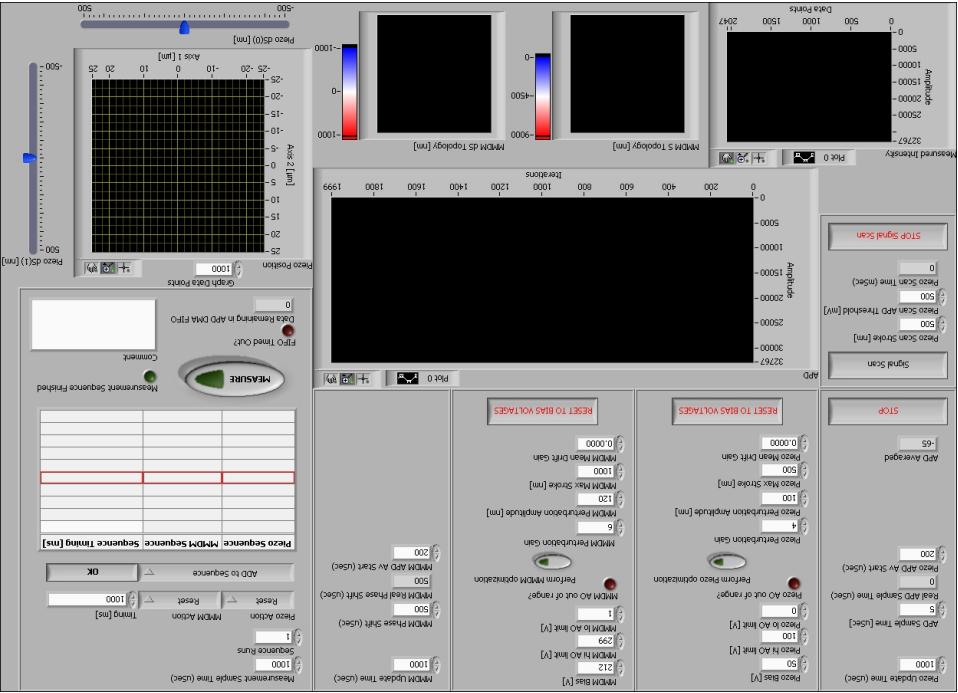| Caption	I/O	Description
ADD to Sequence	I	Drop-down menu to insert a line, delete a line or reset the measurement sequence. select if "Timing [ms]" and the selected action of "Piezo Action" and "MMDM Action" should be a.
APD	O	Graph indicating the current detector signal.
APD Averaged	O	The average value of the detected signal in bits.
APD Sample Time [uSec]	I	The time between two consecutive detector readouts.
Comment	I	Interface to enter user comments in the info file of the measurement.
Data Remaining in APD DMA FIFO	O	Indicates how many items are stored in the FIFO.
FIFO Timed Out?	O	Indicates whether there was an error in data exchange with the FIFO.
Graph Data Points	I	Defines how many of the latest data points should be displayed in "Piezo Position" in order to trace the movement.
Measure	I	Push button to start the measurement.
Measured Intensity	O	Graph indicating the detector signal written to the measurement file.
Measurement Sample Time (uSec)	I	The time constant in μs for recording the detector signal to be written into the measurement file.
Measurement Sequence Finished	O	Indicates if the measurement has finished.
MMDM Action	I	Drop-down menu for the desired action of the MMDM in the measurement sequence.
MMDM AO out of range?	O	This LED indicates if the software limit kept the calculated voltage in range.
MMDM APD Av start (uSec)	I	Offset between MMDM voltage update and starting to average over the detector signal. This takes account to the mechanical response of the mirror.
MMDM Bias [V]	I	The voltage for the MMDM mean position.
MMDM dS Topolody [nm]	O	Shows the changes of the actuator strokes of the MMDM.
MMDM hi AO limit [V]	I	The software limit for the maximum allowed voltage of the MMDM.

Figure 4.19.: Front panel of the host VI "Master SPGDA 2S BN LUTSgrtComp IntAv FAST MeanDriftComp MEASUREMENT (Host).vi".

Caption	I/O	Description
Piezo hi AO limit [V]	I	The software limit for the maximum allowed voltage of the TTM.
Piezo lo AO limit [V]	I	The software limit for the minimum allowed voltage of the TTM.
Piezo Maximum Stroke [nm]	I	Limits the actuator stroke in nm between two consecutive TTM settings.
Piezo Mean Drift Gain	I	Controls the strength of forcing the TTM in its bias position.
Piezo Perturbation Amplitude [nm]	I	Corresponds to $|\Delta S_{[nm]}|$ in equation 4.4 for the TTM.
Piezo Perturbation Gain	I	Corresponds to γ in equation 4.4 for the TTM.
Piezo Position	O	Shows how many μm the beam is deflected in the fiber-coupler plane by the TTM.
Piezo Scan APD Threshold [mV]	I	The voltage level in mV at which the spiral search stops.
Piezo Scan Stroke [nm]	I	The stroke in nm from one TTM step to the next.
Piezo Scan Time (mSec)	O	The overall time in ms the spiral search was active.
Piezo Update Time (uSec)	I	The time in μs between two consecutive voltage outputs to the TTM.
Real APD Sample Time (uSec)	O	Measured time between two consecutive detector read-outs.
RESET TO BIAS VOLTAGES	I	Stops the MMDM optimization algorithm and resets the voltage settings to the bias voltage.
RESET TO BIAS VOLTAGES	I	Stops the TTM optimization algorithm and resets the voltage settings to the bias voltage.
Sequence Runs	I	Indicates how often the measurement sequence should be carried out.
Signal Scan	I	Initiates a spiral search of the TTM starting at the last settings of the TTM.
STOP	I	Stops the program. Always use this button and NOT the LabVIEW stop button in the menu.
STOP Signal Scan	I	Aborts the spiral search of the TTM.
Table for measurement sequence	I	All lines entered in this table will be carried out in the measurement.
Timing [ms]	I	Duration in ms for the desired action of the TTM and MMDM in the measurement sequence.

45

Caption	I/O	Description
MMDM lo AO limit [V]	I	The software limit for the minimum allowed voltage of the MMDM.
MMDM Maximum Stroke [nm]	I	Limits the actuator stroke in nm between two consecutive MMDM settings.
MMDM Mean Drift Gain	I	Controls the strength of forcing the MMDM in its bias position.
MMDM Perturbation Amplitude [nm]	I	Corresponds to $|\Delta S_{[nm]}|$ in equation 4.4 for the MMDM.
MMDM Perturbation Gain	I	Corresponds to γ in equation 4.4 for the MMDM.
MMDM Phase shift (uSec)	I	The time between the output of the TTM and the MMDM.
MMDM Real Phase shift (uSec)	I	Measured time between the output of the TTM and the MMDM.
MMDM S Topolody [nm]	O	Shows the absolute actuator strokes of the MMDM.
MMDM Update Time (uSec)	I	The time in μs between two consecutive voltage outputs to the MMDM.
OK	I	Carries out the action selected in the "ADD to Sequence" drop-down menu.
Perform MMDM optimization	I	Push button to activate the optimization algorithm for the MMDM.
Perform Piezo optimization	I	Push button to activate the optimization algorithm for the TTM.
Piezo Action	I	Drop-down menu for the desired action of the TTM in the measurement sequence.
Piezo AO out of range?	O	This LED indicates if the software limit kept the calculated voltage in range.
Piezo APD Av start (uSec)	I	Offset between TTM voltage update and starting to average over the detector signal. This takes account to the mechanical response of the mirror.
Piezo Bias [V]	I	The voltage for the TTM zero position.
Piezo dS(0) [nm]	O	Indicates the change of the actuator stroke for Axis1 of the TTM.
Piezo dS(1) [nm]	O	Indicates the change of the actuator stroke for Axis2 of the TTM.

44

5. Results

The adaptive-optics setup was first tested in the black lab under ideal conditions in order to debug the system and to get an estimation on the performance of the algorithm. After the successful evaluation in the lab we set up a ~30m outdoor link and tested it on a day with quite strong wind.

5.1. Lab

Figure 4.1 on page 8 shows the setup that was used to do the measurements. The adaptive-optics system was aligned such, that with both mirrors in bias position around 10% of the maximum signal was coupled into single-mode fiber. The update time for both mirrors was set to 800µs which corresponds to 1.25kHz and the "Measurement Sample Time" was 1ms, therefore every millisecond a data point was recorded and stored in the measurement file. Figure 5.1 shows the data of a typical indoor measurement taken in the black lab.

First both mirrors were in bias position and only the TTM was switched on for optimization. It can be seen that the TTM alone already improved the signal within several ms by a factor of ~10. Later the MMDM was switched on as well and the signal was improved even further. After resetting both mirrors to the bias positions, only the MMDM was switched on. This improved the coupling into fiber not as fast as the TTM before, but the signal reached a higher value. Switching on the TTM as well slowly increased the coupling even more. Another reset was carried out before switching on both mirrors at the same time, resulting in a fast improvement up to the maximum level for the TTM alone followed by a slower improvement until an overall maximum.

As expected, due to only two optimization parameters for the TTM, it compensates faster but not as accurate as the MMDM. In contrast the optimization algorithm of the MMDM has to deal with 37 parameters and therefore needs longer to converge to a maximum. However with its 37 actuators the MMDM can compensate for more aberrations and therefore more accurate.
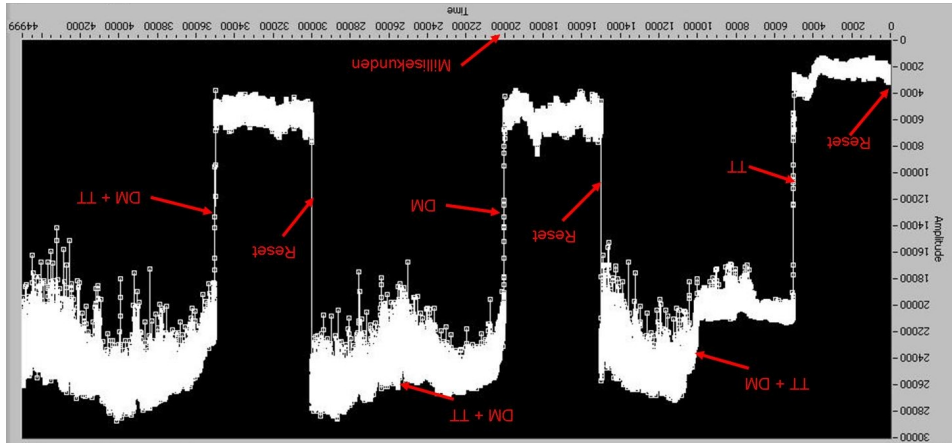
Figure 5.1.: Data of an indoor measurement with the mirrors running at 1.25kHz and the data recorded at 1kHz. First both mirrors were in bias position, then only the TTM was switched on for optimization and later the MMDM as well. After a reset to the bias positions of the mirrors, only the MMDM was switched on at first and then the TTM. Another reset was carried out before switching on both mirrors at the same time.
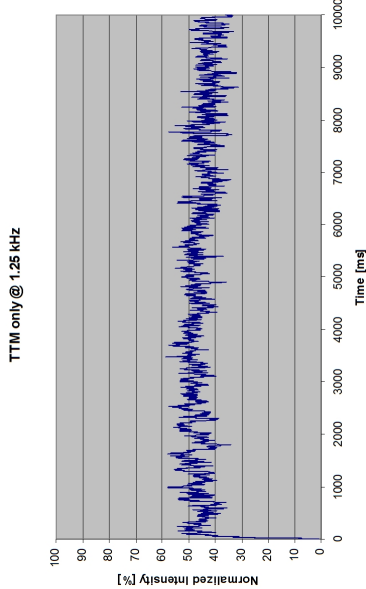
Figure 5.2.: Data of the 30m outdoor measurement with only the TTM running at 1.25kHz and the data recorded at 1kHz.

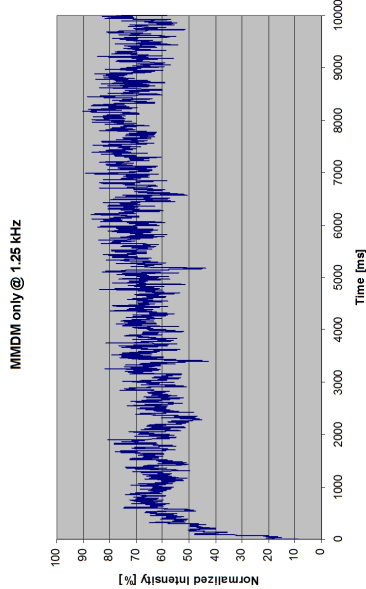Figure 5.3.: Data of the 30m outdoor measurement with only the MMDM running at 1.25kHz and the data recorded at 1kHz.

5.2. Outdoor

The 30m outdoor link was realized by opening the door behind the folding mirror in figure 4.1 on page 8 and placing the mirror ∼10m line-of-sight outside the lab. The laser with the beam expander was placed ∼20m further away, perpendicular to the line-of-sight. Outside the lab the wind was quite strong and reasonably shaking the folding mirror and laser.

As for the indoor test the mirrors were running at 1.25kHz and the measurement data was recorded at a rate of 1kHz. All graphs show an average over 9 measurement runs and are normalized to the overall maximum intensity. Figure 5.2 shows the averaged data for a 10s measurement run with only the TTM optimizing. Again there is a fast increase to 50% intensity and the algorithm keeps it there. In figure 5.3 only the MMDM was switched on. Similar to the result in the lab the MMDM needs more time to find the optimum but finally reaches 70-80% of the maximum intensity. With both mirrors used for optimization (see figure 5.4), the intensity of the coupled light quickly reaches the 60-70% level and steadily increases up to 80-90% with a short spike of maximum intensity. The last graph (figure 5.5) is consecutive to the data in figure 5.4 and shows how quickly the signal is lost if the current optimum setting is kept and no further optimization is carried out.

48

49

116

A. Acknowledgement

I would like to thank my supervisor Josép for his support during my stay as a YGT in the optics section TEC-MMO at ESA-ESTEC. Also I would like to thank my section head Bernhard Furch who gave me the opportunity of a three-months extension in order to finish the project.

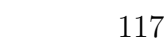Finally I want to thank my office mates Maria and Geert for the great time we had (Blllb ;).

Figure 5.4.: Data of the 30m outdoor measurement with both the TTM and MMDM running at 1.25kHz and the data recorded at 1kHz.

Figure 5.5.: Data of the 30m outdoor measurement recorded at 1kHz and starting from optimized mirror settings with no further optimization carried out.

[9] M. Vorontsov. Decoupled stochastic parallel gradient descent optimization for adaptive optics: integrated approach for wave-front sensor information fusion. *JOSA A*, 19(2):356–368, 2002. ISSN 1520-8532.

[10] National Instruments. What Is PXI? URL http://zone.ni.com/devzone/cda/tut/p/id/4811/.

[11] Physik Instrumente. S-330.30 Manual. URL http://www.pi-portal.ws/index.php?option=com_docman&task=doc_download&gid=200&Itemid=6.

[12] Flexible Optical B.V. OKO Technology 15mm 37-channel MMDM. URL http://www.okotech.com/mmdm.

[13] Thorlabs. DET36A/M. URL http://www.thorlabs.com/thorProduct.cfm?partNumber=DET36A/M.

[14] National Instruments. What Is LabVIEW FPGA? URL http://www.ni.com/fpga/what_is.htm.

[15] National Instruments. LabVIEW FPGA Module On-Line Tutorial. URL http://zone.ni.com/wv/app/doc/p/id/wv-230.

Bibliography

[1] J. SPALL. A stochastic approximation technique for generating maximum likelihood parameter estimates. In *1987 American Control Conference, 6 th, Minneapolis, MN*, pages 1161–1167. 1987.

[2] G. Cauwenberghs. Analog VLSI stochastic perturbative learning architectures. *Neuromorphic systems engineering*, pages 409–435, 1998.

[3] M. Cohen, R. Edwards, G. Cauwenberghs, M. Vorontsov, and G. Carhart. AdOpt: Analog VLSI stochastic optimization for adaptive optics. In *International Joint Conference on Neural Networks(IJCNN'99)*, pages 2343–2346. 1999.

[4] M. Vorontsov, G. Carhart, and J. Ricklin. Adaptive phase-distortion correction based on parallel gradient-descent optimization. *Optics letters*, 22(12):907–909, 1997. ISSN 0146-9592.

[5] V. Polejaev, P. Barbier, G. Carhart, M. Plett, D. Rush, and M. Vorontsov. Adaptive compensation of dynamic wavefront aberrations based on blind optimization technique. In *Proceedings of SPIE*, volume 3760, page 88. 1999.

[6] M. Vorontsov, G. Carhart, M. Cohen, and G. Cauwenberghs. Adaptive optics based on analog parallel stochastic optimization: analysis and experimental demonstration. *JOSA A*, 17(8):1440–1453, 2000. ISSN 1520-8532.

[7] M. Plett, P. Barbier, and D. Rush. Compact adaptive optical system based on blind optimization and a micromachined membrane deformable mirror. *Applied Optics*, 40(3):327–330, 2001. ISSN 0003-6935.

[8] F. Gonte, A. Courteville, and R. D "andliker. Optimization of single-mode fiber coupling efficiency with an adaptive membrane mirror. *Optical Engineering*, 41:1073, 2002.

Bibliography

[1] C. Bennett, et al. Quantum cryptography: Public key distribution and coin tossing. *Proceedings of IEEE International Conference on Computers, Systems and Signal Processing*, 175, 1984.

[2] C. H. Bennett, et al. Teleporting an unknown quantum state via dual classical and Einstein-Podolsky-Rosen channels. *Physical Review Letters*, 70(13):1895–1895, 1993.

[3] M. A. Nielsen, et al. Quantum Computation and Quantum Information. Cambridge University Press, Cambridge, 2000.

[4] N. Gisin, et al. Quantum communication. *Nature Photonics*, 1(3):165–171, 2007.

[5] T. D. Ladd, et al. Quantum computers. *Nature*, 464(7285):45–53, 2010.

[6] M. Zukowski, et al. "Event-Ready-Detectors" Bell experiment via entanglement swapping. *Physical Review Letters*, 71(26):4287–4290, 1993.

[7] H. J. Briegel, et al. Quantum repeaters: the role of imperfect local operations in quantum communication. *Physical Review Letters*, 81(26):5932–5935, 1998.

[8] L. M. Duan, et al. Long-distance quantum communication with atomic ensembles and linear optics. *Nature*, 413:413–418, 2001.

[9] D. M. Greenberger, et al. Going beyond Bell's theorem. *Springer*, 69–72, 1989.

[10] D. M. Greenberger, et al. Bell's theorem without inequalities. *American Journal of Physics*, 58(12):1131–1143, 1990.

[11] H. J. Kimble. The quantum internet. *Nature*, 453(7198):1023–1030, 2008.

[12] T. Herbst. Entanglement-Based Quantum Communication over Long-Distance Free-Space Links. Master's thesis, Vienna University of Technology, 2008.

[13] A. Fedrizzi, et al. High-fidelity transmission of entanglement over a high-loss free-space channel. *Nature Physics*, 5:389–392, 2009.

[14] T. Scheidl, et al. Feasibility of 300 km quantum key distribution with entangled states. *New Journal of Physics*, 11(8):085002, 2009.

[15] T. Scheidl, et al. Violation of local realism with freedom of choice. *Proceedings of the National Academy of Sciences*, 107(46):19708–19713, 2010.

[16] J. Yin, et al. Quantum teleportation and entanglement distribution over 100-kilometre free-space channels. *Nature*, 488(7410):185–188, 2012.

[17] X.-S. Ma, et al. Quantum teleportation over 143 kilometres using active feed-forward. *Nature*, 489(7415):269–273, 2012.

[18] X.-S. Ma, et al. Quantum erasure with causally disconnected choice. *Proceedings of the National Academy of Sciences*, 110(4):1221–1226, 2013.

[19] N. Herbert. FLASH—A superluminal communicator based upon a new kind of quantum measurement. *Foundations of Physics*, 12(12):1171–1179, 1982.

[20] W. K. Wootters, et al. A single quantum cannot be cloned. *Nature*, 299:802–803, 1982.

[21] V. Buzek, et al. Quantum Copying: Beyond the No-Cloning Theorem. *Physical Review A*, 54(3):1844–1852, 1996.

[22] C. Simon, et al. Optimal Quantum Cloning Via Stimulated Emission. *Physical Review Letters*, 84:2993–2996, 2000.

[23] V. Scarani, et al. Quantum cloning. *Reviews of Modern Physics*, 77(4):1225, 2005.

[24] E. Schrödinger. Die gegenwärtige Situation in der Quantenmechanik. *Naturwissenschaften*, 1935.

[25] A. Einstein, et al. Can quantum-mechanical description of physical reality be considered complete? *Phys. Rev.*, 47:777–780, 1935.

[26] G. Ghirardi, et al. A general argument against superluminal transmission through the quantum mechanical measurement process. *Lettere Al Nuovo Cimento (1971–1985)*, 27(10):293–298, 1980.

[27] J. S. Bell. On the Einstein Podolsky Rosen Paradox. *Physics*, 1:195, 1964.

[28] J. F. Clauser, et al. Proposed Experiment to Test Local Hidden-Variable Theories. *Physical Review Letters*, 23(15):880–884, 1969.

[29] J. S. Bell. Introduction to the hidden-variable question. *Foundations of quantum mechanics*, 171–181, 1971.

[30] A. Peres. Separability Criterion for Density Matrices. *Physical Review Letters*, 77(8):1413–1415, 1996.

[31] M. Horodecki, et al. Separability of mixed states: necessary and sufficient conditions. *Physics Letters A*, 223(1):1–8, 1996.

[32] B. M. Terhal. Bell inequalities and the separability criterion. *Physics Letters A*, 271(5-6):319–326, 2000.

[33] M. Lewenstein, et al. Optimization of entanglement witnesses. *Physical Review Letters*, 62(5):052310, 2000.

[34] P. Hyllus, et al. Relations between entanglement witnesses and Bell inequalities. *Physical Review Letters*, 72(1):012321, 2005.

[35] O. Gühne, et al. Entanglement detection. *Physics Reports*, 474(1-6):1–75, 2009.

[36] H. S. Eisenberg, et al. Quantum entanglement of a large number of photons. *Physical Review Letters*, 93(19):193901, 2004.

[37] H. Fearn, et al. Theory of two-photon interference. *J. Opt. Soc. Am. B*, 6(5):917–917, 1989.

[38] H. Weinfurter. Experimental Bell-state analysis. *Europhysics Letters (EPL)*, 25(8):559–564, 1994.

[39] A. Zeilinger, et al. Information transfer with two-state two-particle quantum systems. *Journal of Modern Optics*, 41(12):2375–2384, 1994.

[40] G. Alber, et al. Quantum Information, volume 173 of *An Introduction to Basic Theoretical Concepts and Experiments*. Springer Verlag, Berlin, 2001.

[41] C. K. Hong, et al. Measurement of subpicosecond time intervals between two photons by interference. *Physical Review Letters*, 59(18):2044–2046, 1987.

[42] L. Vaidman, et al. Methods for reliable teleportation. *Physical Review A*, 59(1):116–125, 1999.

[43] N. Lütkenhaus, et al. Bell measurements for teleportation. *Physical Review A*, 59:3295–3300, 1999.

[44] J. Calsamiglia, et al. Maximum Efficiency of a Linear-Optical Bell-State Analyzer. *Applied Physics B*, 72(1):67–71, 2001.

[45] D. Bouwmeester, et al. Observation of Three-Photon Greenberger-Horne-Zeilinger Entanglement. *Physical Review Letters*, 82(7):1345–1349, 1999.

[46] J.-W. Pan, et al. Experimental test of quantum nonlocality in three-photon Greenberger–Horne–Zeilinger entanglement. *Nature*, 403(6769):515–519, 2000.

[47] N. D. Mermin. Extreme quantum entanglement in a superposition of macroscopically different states. *Physical Review Letters*, 65(15):1838–1840, 1990.

[48] S. Roy, et al. Tests of signal locality and Einstein-Bell locality for multiparticle systems. *Physical Review Letters*, 67(20):2761–2764, 1991.

[49] M. Ardehali. Bell inequalities with a magnitude of violation that grows exponentially with the number of particles. *Physical Review Letters*, 46(9):5375–5378, 1992.

[50] M. Zukowski, et al. Critical visibility for N-particle Greenberger-Horne-Zeilinger correlations to violate local realism. *Physical Review Letters*, 56(3):R1682–R1685, 1997.

[51] D. Bouwmeester, et al. Experimental quantum teleportation. *Nature*, 390(6660):575–579, 1997.

[52] D. Bouwmeester, et al. High-Fidelity Teleportation of Independent Qubits. *J. Mod. Opt.*, 47:279–289, 2000.

[53] A. Zeilinger, et al. Three-Particle Entanglements from Two Entangled Pairs. *Physical Review Letters*, 78:3031–3034, 1997.

[54] C. Erven, et al. Experimental three-photon quantum nonlocality under strict locality conditions. *Nature Photonics*, 2014.

[55] J. A. Wheeler. Polyelectrons. *Annals of the New York Academy of Sciences*, 48(3):219–238, 1946.

[56] C. S. Wu, et al. The Angular Correlation of Scattered Annihilation Radiation. *Phys. Rev.*, 77(1):136–136, 1950.

[57] C. A. Kocher, et al. Polarization Correlation of Photons Emitted in an Atomic Cascade. *Physical Review Letters*, 18(15):575–577, 1967.

[58] S. J. Freedman, et al. Experimental test of local hidden-variable theories. *Physical Review Letters*, 28(14):938–941, 1972.

[59] A. Aspect, et al. Experimental test of Bell's inequalities using time-varying analyzers. *Physical Review Letters*, 49(25):1804, 1982.

[60] P. G. Kwiat, et al. New High-Intensity Source of Polarization-Entangled Photon Pairs. *Physical Review Letters*, 75(24):4337–4342, 1995.

[61] C. Kurtsiefer, et al. Generation of correlated photon pairs in type-II parametric down conversion. *Journal of Modern Optics*, 48(13):1997–2007, 2001.

[62] R. W. Boyd. Nonlinear Optics. Academic Press, San Diego, 3 edition, 2008.

[63] M. D. Reid, et al. Violations of classical inequalities in quantum optics. *Physical Review A*, 34(2):1260–1276, 1986.

[64] M. Michler, et al. Interferometric Bell-state analysis. *Physical Review A*, 53(3):R1209–R1209, 1996.

[65] J. D. Franson. Bell inequality for position and time. *Physical Review Letters*, 62(19):2205–2208, 1989.

[66] P. G. Kwiat, et al. Correlated two-photon interference in a dual-beam Michelson interferometer. *Physical Review A*, 41(5):2910–2913, 1990.

[67] W. Grice, et al. Spectral information and distinguishability in type-II down-conversion with a broadband pump. *Physical Review Letters*, 56(2):1627–1634, 1997.

[68] Y.-H. Kim, et al. Generation of pulsed polarization-entangled two-photon state via temporal and spectral engineering. *Journal of Modern Optics*, 49(14-15):2309–2323, 2002.

[69] Y.-H. Kim, et al. Experimental entanglement concentration and universal Bell-state synthesizer. *Physical Review A*, 67(1):010301, 2003.

[70] H. Poh, et al. Eliminating spectral distinguishability in ultrafast spontaneous parametric down-conversion. *Physical Review Letters*, 80(4):043815, 2009.

[71] R. L. Millis, et al. Identification, optimization and protection of optical telescope sites. In International Conference held Lowell Observatory, Flagstaff, Arizona, USA. 1987.

[72] K. Cowles. Site selection criteria for the optical atmospheric visibility monitoring telescopes. *TDA Progress Report 42*, 97:235–239, 1989.

[73] A. E. Siegman. Lasers. University Science Books, 1986.

[74] C. Huygens. The Celestial Worlds Discover'd, Or, Conjectures Concerning the Inhabitants, Plants and Productions of the Worlds in the Planets. 1722.

[75] J. Miller, et al. Photonics Rules of Thumb. Optics, Electro-Optics, Fiber Optics and Lasers. McGraw Hill Professional, 2003.

[76] L. C. Andrews. Field guide to atmospheric optics. 2, 2004.

[77] T. Schmitt-Manderbach. Long distance free-space quantum key distribution. Ph.D. thesis, Ludwig-Maximilians-Universität München, 2007.

[78] S. Dunagan, et al. Spectrometer for Sky-Scanning Sun-Tracking Atmospheric Research (4STAR): Instrument Technology. *Remote Sensing*, 5(8):3872–3895, 2013.

[79] A. N. Kolmogorov. The local structure of turbulence in incompressible viscous fluid for very large Reynolds numbers. 30(4):299–303, 1941.

[80] A. N. Kolmogorov. Dissipation of energy in locally isotropic turbulence. 32(1):16–18, 1941.

[81] L. C. Andrews, et al. Laser Beam Propagation Through Random Media. SPIE - The International Society for Optical Engineering, 1998.

[82] H. Trinquet. Using meteorological forecasts to predict astronomical 'seeing'. *SPIE Newsroom*, 2009.

[83] R. L. Fante. Electromagnetic beam propagation in turbulent media: An update. In Proceedings of the IEEE, 1424–1443. 1980.

[84] R. L. Fante. Electromagnetic beam propagation in turbulent media. In Proceedings of the IEEE, 1669–1692. 1975.

[85] V. I. Klyatskin, et al. On the displacement of spatially-bounded light beams in a turbulent medium in the Markovian-random-process approximation. *Radiophysics and Quantum Electronics*, 15(9):1056–1061, 1972.

[86] D. L. Fried. Anisoplanatism in adaptive optics. *Journal of the Optical Society of America*, 72(1):52, 1982.

[87] ING. Jacobus Kapteyn Telescope. www.ing.iac.es/PR/jkt_info.

[88] ESA. Optical Ground Station. sci.esa.int/sre-fi/36520-optical-ground-station.

[89] IAC. Optical Ground Station. www.iac.es/eno.php?op1=3&op2=6&lang=en&id=7.

[90] Coherent. Chameleon Ultra Family Data Sheet. www.coherent.com/download/6416/Chameleon-Ultra-Family-Data-Sheet.pdf.

[91] PerkinElmer. SPCM-AQ4C. www.perkinelmer.co.uk/PDFS/downloads/dts_spcm-aq4c.pdf.

[92] Y.-S. Kim, et al. Ultra-low noise single-photon detector based on Si avalanche photodiode. *Review of Scientific Instruments*, 82(9):093110, 2011.

[93] National Instruments. PCI-DIO-32HS. www.ni.com/pdf/manuals/371464d.pdf.

[94] T. Scheidl. A fundamental test and an application of quantum entanglement. Ph.D. thesis, University Vienna, Vienna, 2009.

[95] N. Goldovsky, et al. Ionospheric delay contribution to the uncertainty of time and frequency measurements by one-way satellite time transfer method. *Science Direct*, 35:353–362, 2004.

[96] C. Clausen, et al. Quantum storage of photonic entanglement in a crystal. *Nature*, 469(7331):508–511, 2011.

[97] C. H. Bennett, et al. Purification of noisy entanglement and faithful teleportation via noisy channels. *Physical Review Letters*, 76(5):722–725, 1996.

[98] J.-W. Pan, et al. Entanglement purification for quantum communication. *Nature*, 410(6832):1067–1070, 2001.

[99] J.-W. Pan, et al. Experimental entanglement purification of arbitrary unknown states. *Nature*, 423(6938):417–422, 2003.

[100] L. Sabine. Sir Rudolph Peierls: Selected Private and Scientific Correspondence, volume 2. World Scientific, 2009.

Acknowledgements

Special thanks to all my friends for being just the way they are. I can always count on their understanding in bad times and on their dedication to celebrate the good times.

Finally I want to thank my family for their unconditional support during all these years. It is a great relief to know that somebody will stand by you no matter what.

I would like to conclude my thesis with a concise quote of John Bell in his correspondence with Sir Rudolf Peierls, Geneva, 20.08.1980 [100]:

> ”...our students learn quantum mechanics
> the way they learn to ride bicycles
> (both very valuable accomplishments)
> without really knowing what they are doing...”

Curriculum vitae

Personal Facts

Title / Name	MSc Thomas Herbst
Citizenship	Austrian

Work Experience

Sept 08 – Nov 09	Optical Engineer at the European Space Agency (ESA), Noordwijk, The Netherlands.
Oct 06 – July 08	Research fellow at the Institute for Quantum Optics and Quantum Information, Vienna, Austria.
Aug 05 – Sept 05	Internship at ARC Seibersdorf research dept. Quantum Technology, Vienna, Austria.
July 04 – Sept 04	Internship at Infineon Technologies dept. CPR – Nano Processes / Nano Interconnects, Munich, Germany.

Education

Since Feb 10	Doctoral student of Prof. Anton Zeilinger at the Vienna Center for Quantum Science and Technology, Vienna, Austria.
May 08	2nd diploma examination passed with distinction.
June 06	Practical course on manufacturing and characterization of Photovoltaic cells.
June 04	Project work on heteroepitaxial layers of GaN/AlN on Sapphire analyzed with transmission electron microscopy.
Sept 02 – Jan 03	Exchange student at Université Paul Sabatier, Toulouse, France.
Feb 03	1st diploma examination passed with distinction.
2000	Start of the diploma studies (equivalent to MSc) on Technical Physics at Vienna University of Technology, Vienna, Austria.
1990 – 1999	Bundesgymnasium Amstetten, Lower Austria, Austria. Major subjects: Physics and Computer Sciences.

Publications

[1] T. Herbst, T. Scheidl, M. Fink, J. Handsteiner, B. Wittmann, R. Ursin, and A. Zeilinger, "Teleportation of entanglement over 143 km," *arXiv:14030009*, Feb. 2014.

[2] X.-S. Ma, J. Kofler, A. Qarry, N. Tetik, T. Scheidl, R. Ursin, S. Ramelow, T. Herbst, L. Ratschbacher, and A. Fedrizzi, "Quantum erasure with causally disconnected choice," *Proceedings of the National Academy of Sciences*, vol. 110, no. 4, pp. 1221–1226, 2013.

[3]   X.-S. Ma, T. Herbst, T. Scheidl, D. Wang, S. Kropatschek, W. Naylor, B. Wittmann, A. Mech, J. Kofler, E. Anisimova, V. Makarov, T. Jennewein, R. Ursin, and A. Zeilinger, "Quantum teleportation over 143 kilometres using active feed-forward," *Nature*, vol. 489, no. 7415, pp. 269–273, Sep. 2012.

[4]   X.-S. Ma, S. Kropatschek, W. Naylor, T. Scheidl, J. Kofler, T. Herbst, A. Zeilinger, and R. Ursin, "Experimental quantum teleportation over a high-loss free-space channel," *Opt. Express*, vol. 20, no. 21, pp. 23126–23137, Jan. 2012.

[5]   T. Scheidl, R. Ursin, J. Kofler, S. Ramelow, X. S. Ma, T. Herbst, L. Ratschbacher, A. Fedrizzi, N. K. Langford, T. Jennewein, and A. Zeilinger, "Violation of local realism with freedom of choice," *Proceedings of the National Academy of Sciences*, vol. 107, no. 46, pp. 19708–19713, Nov. 2010.

[6]   A. Fedrizzi, T. Herbst, M. Aspelmeyer, M. Barbieri, T. Jennewein, and A. Zeilinger, "Anti-symmetrization reveals hidden entanglement," *New Journal of Physics*, vol. 11, no. 10, p. 103052, Oct. 2009.

[7]   T. Scheidl, R. Ursin, A. Fedrizzi, S. Ramelow, X.-S. Ma, T. Herbst, R. Prevedel, L. Ratschbacher, J. Kofler, T. Jennewein, and A. Zeilinger, "Feasibility of 300 km quantum key distribution with entangled states," *New Journal of Physics*, vol. 11, no. 8, p. 085002, Aug. 2009.

[8]   A. Fedrizzi, R. Ursin, T. Herbst, M. Nespoli, R. Prevedel, T. Scheidl, F. Tiefenbacher, T. Jennewein, and A. Zeilinger, "High-fidelity transmission of entanglement over a high-loss free-space channel," *Nature Physics*, vol. 5, pp. 389–392, May 2009.

[9]   A. Fedrizzi, T. Herbst, A. Poppe, T. Jennewein, and A. Zeilinger, "A wavelength-tunable, fiber-coupled source of narrowband entangled photons," *Opt. Express*, vol. 15, pp. 15377–15386, 2007.

[10]   M. Suda, T. Herbst, and A. Poppe, "Simulating phase coding in quantum cryptography: influence of chromatic dispersion," *Eur. Phys. J. D*, vol. 42, no. 1, pp. 139–145, Dec. 2006.

Recent Conferences

17 – 21 Aug 14   Oral presentation at the SPIE international Symposium on Optical Engineering + Applications, San Diego, USA.

19 – 22 June 14   Poster presentation at "Quantum [Un]Speakables II: 50 Years of Bell's Theorem", Vienna, Austria.

07 – 09 May 14   Oral presentation at the International Conference on Space Optical Systems and Applications, Kobe, Japan.

24 – 28 Feb 14   Poster presentation at the International Conference on Quantum Optics 2014, Obergurgl, Austria.

03 – 07 Feb 14   Poster presentation at the Conference on Quantum Information Processing, Barcelona, Spain.

03 Sept 13   Oral presentation at the annual meeting of the Austrian Physical Society, Linz, Austria.